Isochoric generation and spectroscopic diagnosis of high energy density systems

A thesis submitted for the degree of

Doctor of Philosophy

Author: Oliver Humphries
College: Trinity College
Supervisor: Dr. Sam Vinko

Atomic and Laser Physics
Department of Physics
Mathematical, Physical and Life Sciences Division
University of Oxford

Hilary Term 2020

Abstract

Advances in both optical laser and X-ray Free Electron Laser (XFEL) facilities have extended the regimes accessible in laser targets. Petawatt lasers such as Orion at AWE can be routinely used to drive targets to extreme conditions of multi-keV temperatures. Isochoric heating with an XFEL to temperatures of 100's of eV has been demonstrated and well described on prototypical metals and low-Z mixtures, and the bright, tunable x-ray source is often used as a probe in Warm Dense Matter (WDM) and High Energy-Density (HED) studies. X-ray diagnostics are often used to characterise the conditions present in such a laser target, with stringent demands on collection efficiency to yield significance in signal/noise in order to characterise systems with potentially large spatio-temporal gradients.

This thesis describes a set of experiments to isochorically generate and characterise WDM and HED systems relevant to astrophysical plasmas and Inertial Confinement Fusion. The focus of this work is on using measured X-ray Emission Spectroscopy or Resonant Inelastic X-ray Scattering (RIXS) spectra to bound the conditions present in the laser target, and using Single Photon Counting informed techniques to maximise the signal/noise in recovered spectra. Accurate accounting of the single photon response of x-ray detectors is used to detail the absolute value and error on recovered spectral intensity, and from that to inferred plasma parameters. The particular systems considered in this work are nanowire targets irradiated at relativistic intensities, RIXS measurements of warm-dense nickel, and nano-focused XFEL heating of solid density iron.

The recovered plasma conditions mapped from experimental data are shown to correspond well to Particle-In-Cell and Density Functional Theory, benchmarking simulation capacity and offering insights into factors affecting the target's response to laser drive. The results and methods presented here could inform and complement future efforts to investigate warm- and hot-dense systems, as a diagnostic capability or elucidating a navigable route toward ultra-HED systems.

Acknowledgements

First, I would like to thank my supervisor, Sam Vinko, for giving me every opportunity during this project to pursue problems in my way, and supporting me throughout. Similarly, to Justin Wark and Matt Hill, for their advice and assistance over the years. I also want to thank everyone I dragged along to coffee at some point – you may not always have wanted to hear me talk through what I was working on, but you put up with it valiantly. Particular thanks go to Gabriel Perez-Callejo, Alex Savin, Patrick Hollebon, Ryan Royle and David McGonegle, who suffered through more coffee trips than most, along with Tom Preston, Orlando Ciricosta, and Charlotte Palmer.

To my family – you have all kept me going, my parents and siblings have been a constant source of support (despite me having to re-explain what I do every time). In particular my brother James, for being more helpful than I think he knows.

Finally, to my friends, without whom this would not have been possible, and anyone else that has in some way helped. I don't dare make a list as I would inevitably miss a number of people, so: if you think your name should be here, *you're probably right.*

Contents

List of Figures

Acronyms

ADU Analogue-to-Digital Unit 37, 40

AWE Atomic Weapons Establishment 1, 21, 23, 76, 82

CCD Charge Coupled Device III, 37–40

CSPAD Cornell-SLAC Pixel-Array Detector 36

CXI Coherent X-ray Imaging 98

DFT Density Functional Theory 22, 63, 70, 73, 114, 117

DOS Density Of States 18, 22, 58, 59, 66, 68–72, 116

EMP Electromagnetic Pulse 36

EOS Equation of State 97, 115

EuXFEL European XFEL 1, 20, 21, 32, 74

FWHM Full Width Half Max 16, 33, 37, 40, 60, 61, 80, 83, 91, 99, 101, 108

HAPG Highly-Annealed Pyrolitic Graphite 60, 61

HED High Energy-Density IV, 1–4, 9, 10, 12, 16, 17, 20, 54, 55, 60, 73, 75, 79, 96, 97, 111, 113, 114

IAEA International Atomic Energy Agency 104, 105

ICF Inertial Confinement Fusion 1, 3, 14, 15, 73, 75, 96, 113, 117

IPD Ionization Potential Depression III, 20, 54, 55, 64, 66, 69–71, 73, 74, 97, 98, 111, 113, 116

KB Kirkpatrick-Baez 99

LCLS Linac Coherent Light Source 16, 17, 21, 22, 32, 37, 55, 60, 61, 74, 98

LULI Laboratoire pour l'Utilisation des Lasers Intenses 1, 39, 80

MEC Matter in Extreme Conditions 18, 60, 97

NIF National Ignition Facility 14

OxCHEDS Oxford Centre for High Energy-Density Science 22

PIC Particle-In-Cell IV, 21, 90, 91, 114, 117

RHS Right-Hand Side 6

RIXS Resonant Inelastic X-ray Scattering III, 22, 24, 26, 54, 55, 59, 60, 62, 65–73, 113, 115

SASE Self-Amplified Spontaneous Emission 16, 63, 72

SEM Scanning Electron Microscope III, 76, 83

SLAC Stanford Linac Accelerator Centre national accelerator laboratory 1, 22, 55

SPC Single Photon Counting 21, 39–41, 44, 46, 81, 116

TOF Time Of Flight 47, 84

WDM Warm Dense Matter 1, 4, 9, 10, 12, 16, 17, 19, 24, 70, 71, 73, 97, 113

XES X-ray Emission Spectroscopy 19, 24, 37

XFEL X-ray Free Electron Laser III–V, 3, 16–18, 20, 22, 55, 60–69, 72, 73, 96–100, 102, 103, 105–109, 111–117

XRSC X-ray Streak Camera 46, 47

XRSS X-ray Streaked Spectrometer 46, 47, 76, 83, 84, 87, 88, 90–92

XRTS X-ray Thomson Scattering 25, 70, 115

Symbols

a_0 Normalized vector potential 15, 83

ω Angular frequency 12–14, 25, 56–59, 63, 80

$\mathbf{B}$ Magnetic flux density 12, 13

c Speed of light 13, 14, 25, 28, 29, 48, 56–59

σ Electrical conductivity 12, 13

$\mathbf{J}$ Current density 13

$\mathbf{D}$ Electric displacement field 12

λ_D Debye length 4–6

$\mathbf{E}$ Electric field strength 12, 13, 30, 48

e electron charge 4–6, 13, 14, 25, 28, 29, 37, 40, 48, 56–59

ε_0 Vacuum permittivity 4–6, 12–14

E Energy 4, 6, 25, 28, 29, 35, 56, 57, 64

$\mathbf{H}$ Magnetic field strength 12

J Angular momentum 6

k Wavevector 12, 14

k_B Boltzmann constant 4, 5, 70

$\mathcal{L}$ Lagrangian 6

λ Wavelength 15, 28, 78–80

m Particle mass 6, 13, 14, 25, 56–59

n_c Plasma critical density 14, 80

n_e Electron density 4, 5, 11, 13

n_i Ion density 4, 5

$\mathbf{P}$ Electric polarization 12

ϕ Electric potential energy 5

T Temperature 4, 5, 11, 57–59, 64, 70, 86–89, 92

ω_p Plasma frequency 13, 14

Ω Incident photon energy 24, 25, 56–59, 63

Z Atomic number 4–6, 20, 72, 98, 115

1 Introduction

This thesis details some of the work performed by the author on x-ray spectroscopic measurements to diagnose key parameters of isochorically heated plasma systems in the WDM and HED regime. Work contributing to this thesis was performed at a variety of facilities including the European XFEL (EuXFEL), Stanford Linac Accelerator Centre national accelerator laboratory (SLAC), Atomic Weapons Establishment (AWE), and Laboratoire pour l'Utilisation des Lasers Intenses (LULI), with correspondingly diverse international experimental teams. This chapter serves the purpose of introducing the desirable and oft difficult to achieve nature of isochorically heated plasma systems, as well as the key mechanisms and routes used to generate such systems. The structure of the remainder of the thesis, as well as contributions of the author and others to the work are set out within.

1.1 Isochorically heated systems

Isochorically heated systems are raised in energy while maintaining the same volume, and therefore density. In the field of HED physics, isochoric systems are of particular interest as a way of understanding astrophysical bodies [1, 2], where high densities are maintained by gravitational pressure, and navigating toward the Lawson criterion for energy gain in Inertial Confinement Fusion (ICF) [3, 4] by understanding the properties of hot, dense plasma systems. Key conditions in HED are shown in Fig. 1.1, along with representative plasma conditions from astrophysics and ICF in comparison to experimentally obtained systems.

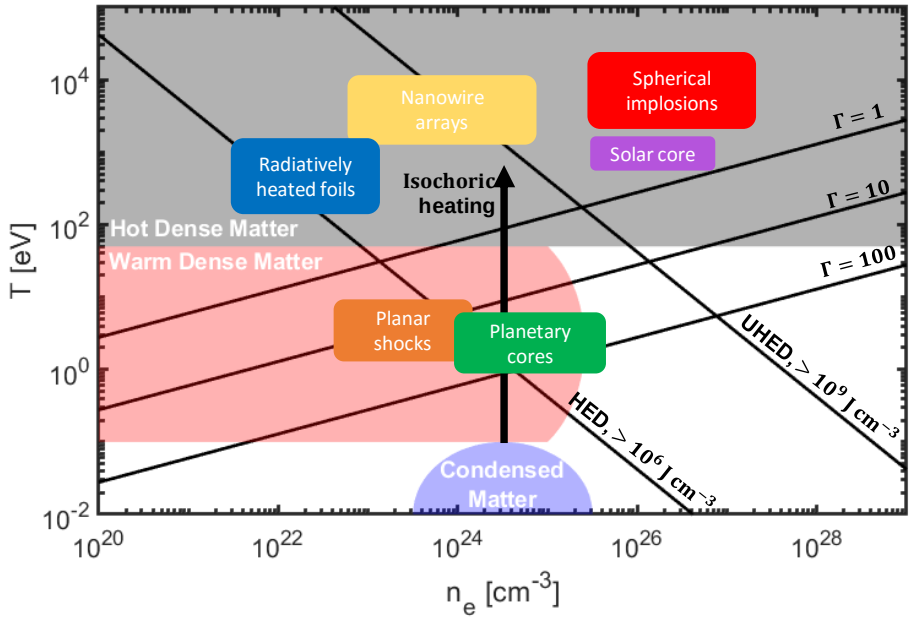

Figure 1.1: Overview of the range of plasma conditions and phases present in the study of HED systems, illustrating the regimes of interest for this work, as well as the nomenclature. Temperature-density curves for strongly coupled plasmas are shown, calculated from equation (3) assuming complete ionization, along with common reference conditions to astrophysical plasmas.

In order to study these exotic states of matter, new strategies to heat systems rapidly – before they have time to expand – and volumetrically – throughout the whole system simultaneously – have been sought. Without the large gravitational pressures in planetary and stellar physics, matter heated to in excess of 10^7 K has an unfortunate tendency to blow up before you can do anything useful with it. One method to achieve these extreme conditions is to use high power laser systems, with contemporary lasers achieving up to petawatt intensities [5] that can be focused into a small spot on a target, rapidly heating a small volume to multi-keV temperatures.

Lasers can also be used to generate highly energetic particles [6, 7, 8] that have

the advantage of propagating further into the target medium than the optical skin depth. Heating the system volumetrically has the significant advantage of lowering the plasma parameter gradients, to make a more uniform plasma, with well controlled conditions, less likely to disassemble due to instabilities – of great interest in fast ignition ICF efforts [9, 10] where a focused heavy-ion beam offers excellent energy coupling to a well defined volume. Less variation in key plasma parameters also makes the system easier to diagnose and model.

A third method to achieve HED states of matter is utilising the recent advances in 4^{th} generation x-ray light sources, XFELs [11, 12, 13]. These systems use the coherent x-rays emitted by relativistic electrons when passed through alternating magnetic fields in an undulator [14]. The x-ray pulse typically delivers $\sim$2 mJ in $\mathcal{O}(10\,\text{fs})$ to a micron-sized focal spot. While the intensities on target are comparable to optical systems, $10^{18}\,\text{W}\,\text{cm}^2$ [15], they can be absorbed over the extinction depth of the target, typically a few microns for x-ray wavelengths, and generate high energy photo-electrons which rapidly thermalize the bulk to extreme temperatures [12, 16]. The direct coupling of individual x-ray photons to absorption or scattering events also permits a variety of additional methods to diagnose the conditions inside the target.

1.2 Key mechanisms and plasma diagnostics

Fundamentally, a plasma consists of a quasi-neutral ionized system, with free electrons and ions, which supports a wide variety of oscillations, excitations and interactions. Plasma is the most abundant form of normal matter in the universe: it forms in the extreme temperatures and pressures of stellar conditions where elec-

tron pressure can dominate, as well as the cold, diffuse interstellar medium where particles are so far apart that electron capture is unlikely.

In the work discussed here, there is a focus on dense, strongly coupled plasma, where the Coulomb interaction energy between particles is comparable to thermal energy. Introducing the ion density, n_i, the electron density, n_e - which for a neutral system has the relation $n_{e0} = Zn_i$ for ion charge Z – the energy of an electron within a Coulomb potential is given by the charge interaction

$$E_{Coulomb} = \frac{Ze^2}{4\pi\varepsilon_0 r_0}, \tag{1}$$

where r_0 here is taken as the radius of a sphere containing on average one electron within the plasma,

$$r_0 = \left(\frac{4\pi n_{e0}}{3}\right)^{-\frac{1}{3}}. \tag{2}$$

The ratio of the Coulomb and thermal energies, $k_B T$, within the system is fundamental to plasma interactions

$$\Gamma = \frac{E_{Coulomb}}{k_B T} = \frac{Ze^2}{4\pi\varepsilon_0 k_B T}\left(\frac{4\pi n_e}{3}\right)^{\frac{1}{3}}, \tag{3}$$

as when $\Gamma \gtrapprox 1$ – written here for the electron-ion coupling – the Coulomb interactions of a system can no longer be treated peturbatively, and the plasma is said to be strongly coupled. A schematic diagram of WDM and HED states of matter is shown in figure 1.1, along with corresponding values of Γ.

A similar ratio also appears contained within the Debye length, λ_D, which is the measure of the scale length over which static fields persist within a plasma. For a classical plasma, the Debye length is found from Poisson's equation, assuming a

thermal ensemble with radial symmetry and small charge separation:

$$\nabla^2\phi = (Zn_i - n_e)\frac{e}{4\pi\varepsilon_0} \tag{4}$$

$$n_e = n_{e0}\exp\left(-\frac{e\phi}{k_BT}\right) \tag{5}$$

$$\frac{1}{r}\frac{\partial^2}{\partial r^2}(r\phi) = \frac{n_{e0}e}{\varepsilon_0}\left(1 - \exp\left(\frac{-e\phi}{k_BT}\right)\right) \tag{6}$$

$$\approx \frac{n_{e0}e^2\phi}{\varepsilon_0 k_BT} \tag{7}$$

$$\phi = \frac{\phi_0}{r}\exp\left(-\frac{r}{\lambda_D}\right) \tag{8}$$

where here the quantity $n_{e0}e^2/(\varepsilon_0 k_BT) = {\lambda_D}^{-2}$, can be identified as the Debye length, which is the characteristic charge screening length. The number of particles contained within the Debye sphere

$$\frac{4\pi}{3}{\lambda_D}^3 n_{e0} = \frac{4\pi\left(\varepsilon_0 k_BT\right)^{\frac{3}{2}}}{3n_{e0}^{\frac{1}{2}}e^3} \tag{9}$$

is found to be inversely proportional to the root of the electron density, n_{e0}. This is the case as the assumptions in linearising the exponential of large thermal energy break down in the case where the inter-particle distances become small in such a dense plasma, and the idealised radially symmetric charge distribution now only averaging over a small number of electrons.

1.2.1 Yukawa scattering

Key transport coefficients in a plasma are found by considering scattering and collisions of charged particles within the screened potential shown in equation (8) [17, 18]. Often in classical plasmas a scattering coefficient is found using a

Coulomb potential, cut off at an impact parameter corresponding to λ_D, however if the identified form of the potential is maintained, a simple set of equations of motion in an attractive Yukawa potential with screening length λ are found as

$$\frac{1}{2}m\dot{\mathbf{r}}^2 - \frac{k}{r}\exp\left(-\frac{r}{\lambda}\right) = E, \tag{10}$$

where $k = Ze^2/4\pi\varepsilon_0$. Identifying constants of motion from the Lagrangian,

$$\frac{d}{dt}\left(\frac{\partial\mathcal{L}}{\partial\dot{\theta}}\right) = \frac{\partial\mathcal{L}}{\partial\theta} = 0 \tag{11}$$

$$\rightarrow mr^2\dot{\theta} = J. \tag{12}$$

Therefore re-writing the equation of motion, and using a substitution $r(t) \rightarrow \lambda/z(\theta(t))$:

$$\frac{1}{2}m\left(\dot{r}^2 + \frac{J^2}{mr^2}\right) - \frac{k}{r}\exp\left(-\frac{r}{\lambda}\right) = E \tag{13}$$

$$\dot{r} = -\frac{\lambda\dot{\theta}}{z^2}\frac{dz}{d\theta} = -\frac{r^2\dot{\theta}z'}{\lambda} = -\frac{Jz'}{m\lambda} \tag{14}$$

$$\frac{J^2}{2m\lambda^2}\left(z'^2 + z^2\right) - \frac{kz}{\lambda}\exp\left(-z^{-1}\right) = E \tag{15}$$

$$z'^2 + z^2 - \frac{2m\lambda k}{J^2}z\exp\left(-z^{-1}\right) = \frac{2m\lambda^2 E}{J^2}. \tag{16}$$

It can be seen there are only two key parameters characterising the scattering from such a potential. Substituting the form of $E = mv^2/2$, $J = mvb$ for the velocity, v, and impact parameter, b, at $r = \infty$, the Right-Hand Side (RHS) of the equation becomes a simple ratio $(\lambda/b)^2 = \alpha^2$, and the prefactor to the potential energy contains a ratio of the Coulomb and kinetic (thermal) energy, $2k/mv^2 = \beta \approx \Gamma$. Identifying the distance of closest approach at $z' = 0$, a deflection angle can be

found by integrating in z

$$\Delta\theta = 2\int_0^{\frac{\lambda}{r_0}} \frac{dz}{\sqrt{\alpha^2 + \alpha\beta z e^{-z^{-1}} - z^2}} - \pi. \tag{17}$$

It can easily be seen that the result of

$$\alpha^2 + \alpha\beta z e^{-z^{-1}} = z^2 \tag{18}$$

results in a singularity, which is the same condition used to find the upper limit of the integral. Although the integrand becomes infinite, in most cases the integral is still finite. Expanding the term in the square root around the singularity at $z = \lambda/r_0 - \epsilon = z_0 - \epsilon$

$$\alpha^2 + \alpha\beta(z_0 - \epsilon)\exp\left(-\frac{1}{z_0 - \epsilon}\right) - (z_0 - \epsilon)^2. \tag{19}$$

Considering first the exponential:

$$\exp\left(-\frac{1}{z_0 - \epsilon}\right) = \exp\left(-\frac{1}{z_0}\frac{1}{1 - \frac{\epsilon}{z_0}}\right) \tag{20}$$

$$\approx \exp\left(-\frac{1}{z_0}\right)\exp\left(-\frac{\epsilon}{z_0^2} - \frac{\epsilon^2}{z_0^3}\right) \tag{21}$$

$$\approx \exp\left(-\frac{1}{z_0}\right)\left(1 - \frac{\epsilon}{z_0^2} - \frac{\epsilon^2}{z_0^3} + \frac{\epsilon^2}{2z_0^4} + \mathcal{O}(\epsilon^3)\right), \tag{22}$$

when retaining only terms $\mathcal{O}(\epsilon^2)$ and below. Inserting this form of the exponential back into equation (19), and identifying the constant terms equating to zero and again dropping terms cubic and above

$$\alpha^2 + \alpha\beta(z_0 - \epsilon)\exp\left(-\frac{1}{z_0}\right)\left(1 - \frac{\epsilon}{z_0^2} - \frac{\epsilon^2}{z_0^3} + \frac{\epsilon^2}{2z_0^4}\right) - z_0^2 + 2z_0\epsilon - \epsilon^2 \tag{23}$$

$$\left[\alpha^2 + \alpha\beta z_0 \exp\left(-\frac{1}{z_0}\right) - z_0^2\right] + \epsilon\left[2z_0 - \alpha\beta e^{-1/z_0}\left(1 + \frac{1}{z_0}\right)\right] + \epsilon^2\left[\alpha\beta e^{-1/z_0}\left(\frac{1}{2z_0^3}\right) - 1\right]. \quad (24)$$

Taking leading order in ϵ, the integral of $\int d\epsilon\ \epsilon^{-\frac{1}{2}} = 2\sqrt{\epsilon}$ can be performed to give a finite result, however if the leading order in ϵ disappears then the integral contains a simple pole, which yields an infinite integral. The condition of a diverging integral can be seen to be

$$\alpha\beta \exp\left(-\frac{1}{z_0}\right)\left(1 + \frac{1}{z_0}\right) = 2z_0, \quad (25)$$

into which the transcendental dependence is removed by using the condition in equation (18), $\alpha\beta e^{-1/z_0} = (z_0^2 - \alpha^2)/z_0$, rearranging to become

$$z_0^3 - z_0^2 + \alpha^2(z_0 + 1) = 0. \quad (26)$$

Finally, classifying the roots of this cubic equation, with the requirement that $z \in \mathbb{R}^{0+}$, the condition for a singularity to exist in scattering angle translates into a requirement on α^2 from the cubic discriminant. For a cubic equation $ax^3 + bx^2 + cx + d = 0$, the discriminant $b^2c^2 - 4ac^3 - 4b^3d - 27a^2d^2 + 18abcd$ is zero if two roots are equal – i.e. the condition at which the cubic equation crosses first crosses the positive z-axis, resulting in

$$\alpha^6 + 11\alpha^4 - \alpha^2 = 0 \quad (27)$$

$$\alpha \leq \sqrt{\frac{\sqrt{125}-11}{2}} \approx 0.3003. \tag{28}$$

For systems of interest in this thesis - solid density with thermal energies of 1 eV to 1000 eV, the relevant ranges of these parameters, α and β, is large. The upper limit of the range of impact parameters is effectively given by r_0, as beyond this the potential from other particles dominates. As the potential also becomes exponentially small for $b \gg \lambda$, and for $b \ll \lambda$ a Coulombic dependence is recovered, the range $\alpha \in [0.2, 3]$ is used. The ratio in β, containing the Coulomb potential energy over the kinetic, would include the full range of velocities present in a plasma distribution, so a range from $\beta \approx 0$ to 50 is taken as illustrative. A plot of example scattering solutions for this parameter range is shown in Figure 1.2. In a traditional plasma – large α – the approximation of small scattering events can largely hold, allowing simple semi-analytic form for the rate of collisions – however the non-linearity introduced by the screening means that in strongly coupled WDM and HED systems, the plasma parameters depending on the Coulomb logarithm must be heavily modified as new effects take hold – making them an rich experimental platform.

While obviously the example of a purely Yukawa potential does not capture all of the physical interactions, as quantum effects dominate close to the nucleus or electronic capture removing some scatterers, it is illustrative of the changes in the dominant mechanisms of transport in strongly coupled systems, as well as demonstrating the inefficient momentum transfer from high-energy (low-β) scattering events. If laser-plasma interaction generates such high-energy particles in size-

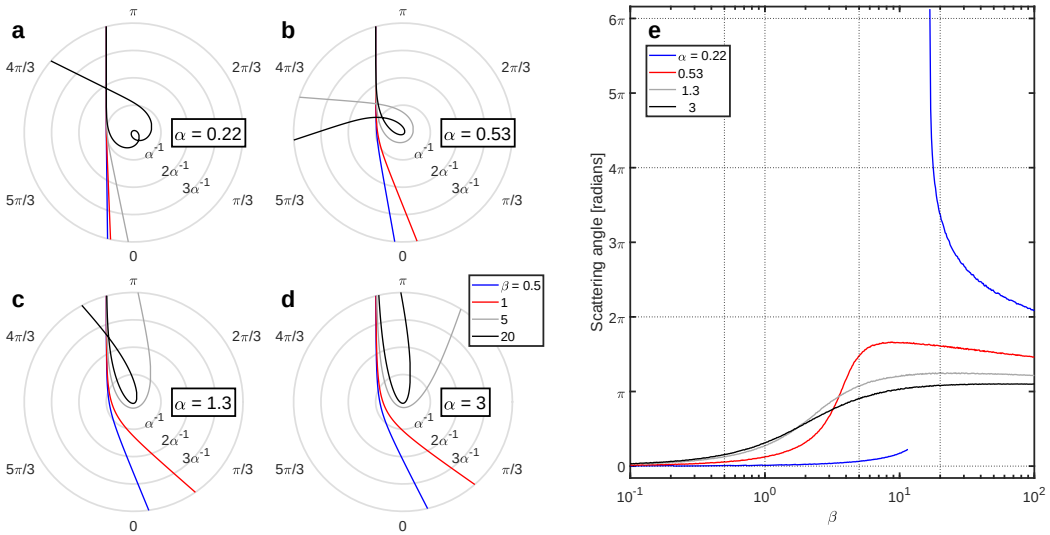

Figure 1.2: Scattering diagrams from a set of Yukawa potentials with non-dimensionalised parameters α and β as in equation (17), in the ranges applicable to WDM and HED plasmas, showing (a)-(d) example scattering trajectories and (e) scattering angle, where intersections of vertical lines correspond to the trajectories shown in (a)-(d). Larger α closely approximates Coulomb scattering, modified more strongly at increased $\beta \propto \Gamma$, requiring corresponding modifications to transport coefficients. High energy particles (low β) retain a small scattering angle from the potential, however they also are less efficient at transferring energy via collision.

able quantities, this can lead to a largely decoupled population of particles above and below the singularity in scattering cross section. Small scattering angles, and therefore low momentum transfer cross section occurring in low-α systems – those where the screening length becomes comparable to the inter-particle distance – allow fast, 'hot', electrons to permeate the system and deposit energy deeper into a laser target. The spontaneous emergence of this divergence in scattering angle is just one example of the significant differences present in strongly coupled systems, where the energy scale of electron binding, kinetic energy, coulomb interactions and temperature all become comparable.

1.3 Laser systems and absorption on target

For experimentally generated plasmas, the key parameters, n_e and T, are strongly dependent on how it has been produced. In tokamaks, for example, the temperature can be in excess of 10 keV however the density is low [19]. In laser produced plasmas, light must be absorbed in the target which requires a certain optical depth in order to couple the energy into the target. For solid density targets, optical light is absorbed within nm of the surface. This energy heats the system, ionizing atoms within the target, increasing the electron density. The timescale of the absorption and equilibration across the target governs how much it can expand in that time, giving a n_e-T track to laser plasma absorption depending on laser intensity.

The mechanism of absorption of laser light also depends on both the incident light and the plasma conditions. At very low intensity ($< 10^8\,\mathrm{W\,cm^{-2}}$) the laser energy is insufficient to cause significant ionization in the target, and therefore most

of the energy interacts with bound electrons. Recasting Maxwell's equations for a wave propagating through a material as a Displacement vector $\mathbf{D} = \epsilon\mathbf{E} = \varepsilon_0\mathbf{E} + \mathbf{P}$ for polarization $\mathbf{P}$, and $\mathbf{H} = \mathbf{B}/\mu$:

$$\nabla \cdot \epsilon\mathbf{E} = 0 \tag{29}$$

$$\nabla \cdot \mu\mathbf{H} = 0 \tag{30}$$

$$\nabla \times \mathbf{E} = -\mu\frac{\partial \mathbf{H}}{\partial t} \tag{31}$$

$$\nabla \times \mathbf{H} = \epsilon\frac{\partial \mathbf{E}}{\partial t} + \sigma\mathbf{E}, \tag{32}$$

for conductivity σ. Forming a wave equation via a fourier transform yields a dispersion relation in the wavevector k and angular frequency ω:

$$k^2 = \mu\epsilon\omega^2 - i\mu\sigma\omega. \tag{33}$$

For a good conductor (i.e. $\sigma \gg \epsilon\omega$), a skin depth to which the wave evanescently propagates is found from the imaginary component of k

$$\delta = [\mathcal{I}(k)]^{-1} = \sqrt{\frac{2}{\mu\sigma\omega}}. \tag{34}$$

Above these intensities, $> 10^8\,\mathrm{W\,cm^{-2}}$, many electrons can be considered "free", and interact directly with the laser light.

1.3.1 Long-pulse lasers

Long pulse lasers typically with pulse durations $\mathcal{O}(\mathrm{ns})$ and energies that can be in excess of 1 kJ are extremely versatile tools in the production of WDM and HED states. Initially the long pulse rapidly heats the surface layer of a target, creating

an ablating hot, low density plasma. The ionized electrons in the plasma oscillate and re-radiate the light, modifying the propagation of the oscillating field

$$\mathbf{E} = \mathbf{E}(x)e^{-i\omega t}, \tag{35}$$

accelerating the electrons

$$\frac{\partial \mathbf{u}_e}{\partial t} = -\frac{e}{m}\mathbf{E}, \tag{36}$$

yielding a current density

$$\frac{\partial \mathbf{J}}{\partial t} = -n_e e\frac{\partial \mathbf{u}_e}{\partial t} = \varepsilon_0 {\omega_p}^2 \mathbf{E} \tag{37}$$

$$\mathbf{J} = \frac{i\varepsilon_0 {\omega_p}^2}{\omega}\mathbf{E} \tag{38}$$

where the high frequency conductivity can be identified as $\sigma = i\varepsilon_0 {\omega_p}^2/\omega$ with a plasma frequency ${\omega_p}^2 = n_e e^2/m\varepsilon_0$.

Using Faraday's and Ampere's laws with the above form of the oscillating electric field

$$\nabla \times \mathbf{E} = \frac{i\omega}{c}\mathbf{B} \tag{39}$$

$$\nabla \times \mathbf{B} = \mu_0 \sigma \mathbf{E} - \mu_0 \varepsilon_0 \frac{i\omega}{c}\mathbf{E} \tag{40}$$

and inserting σ from (38), taking the curl of equation (39) and identifying $\mu_0\varepsilon_0 = c^{-2}$ to arrive at a wave equation

$$\nabla^2 \mathbf{E} - \nabla\left(\nabla \cdot \mathbf{E}\right) + \frac{\omega^2}{c^2}\left(1 - \frac{{\omega_p}^2}{\omega^2}\right)\mathbf{E} = 0. \tag{41}$$

Finally, assuming the spatial dependence of the wave takes the form $\mathbf{E}(x) =$

$e^{i\mathbf{k}\cdot\mathbf{x}}$, the dispersion relation

$$\omega^2 = {\omega_p}^2 + k^2c^2 \tag{42}$$

is found, and therefore $\omega \geq \omega_p$ for a non-decaying waveform, and the critical density of the plasma at $\omega = \omega_p$, beyond which light cannot penetrate, is

$$n_c = \frac{\omega^2 m\varepsilon_0}{e^2}. \tag{43}$$

The critical surface for the laser's wavelength expands away from the dense region of the target with the ablating plasma, limiting the direct coupling of the laser energy into the system, where now heating is due to conduction from the critical surface, or compression of the target from the ablation pressure. In indirect drive systems, the laser's energy is used to heat a surface which then re-emits a thermal radiation bath at high energies, which can penetrate further into the target and heat it more uniformly.

The primary mechanisms for coupling laser energy into the target here are inverse bremsstrahlung [20, 21] whereby electrons accelerated in the laser field then collide with the neutralising ionic background, and resonance absorption [22], where a laser pulse reaching the critical surface drives a plasma wave.

Long pulse lasers are sufficiently lengthy that (magneto-)hydrodynamic processes can occur within the timescale of the laser interaction, making them suitable for shock compression and ICF experiments. At the National Ignition Facility (NIF) the indirect drive scheme is used to generate blackbody radiation with a characteristic temperature of 100's of eV to attempt to provide a more homoge-

neous drive to the ICF pellet to limit instabilities under compression.

1.3.2 Short-pulse lasers

The need to access a wider range of states with laser heating has driven much research into shorter pulse, higher energy laser systems with huge demands on the performance and contrast. Upon heating a system, the ablating plasma can rapidly form a supercritical plasma mirror away from the denser parts of the target, lowering the absorption and therefore final temperature achieved. Since the development of chirped-pulse amplification in the 1980's [23], work that was recently recognised with the Nobel prize, short pulse systems have become accessible for university-lab scale facilities, as well as the largest systems having pulse powers measured in PW [5]. Shorter pulses allow more energy to be coupled into the target before it expands, but there are a new set of problems in the dominant mechanisms for absorption at extreme intensities, $> 10^{17}\,\mathrm{W\,cm^{-2}}$ as relativistic interactions play a role.

For very short pulse laser systems, typically with pulse lengths 1 fs to 1000 fs, the timescale of liberating bound electrons into the (quasi-)free valence band can be comparable with the thermalization time. The outputs from short pulse lasers are often expressed in terms of the normalized vector potential,

$$a_0 = \sqrt{0.731 \times I[10^{18}\,\mathrm{W\,cm^2}]\lambda^2[\mu\mathrm{m}^2]} \tag{44}$$

where $a_0 = 1$ is normalized as the electron kinetic energy from laser oscillations being equal to it's rest mass, and signifies the onset of relativistic interactions. These extreme intensities drive heating by MeV-scale 'hot' electrons generated by

the laser [8] which – as shown by figure 1.2 – can have stopping distances which are long compared to the target thickness, and reflux through the target once it acquires a net positive charge [24]. Due to the limited timescale of interaction, short pulse lasers are also often used as part of a diagnostic capability to produce x-rays or high energy particles in order to radiographically or tomographically image a system in a time-resolved way [25, 26, 27, 28].

Other mechanisms to improve energy coupling to the target have also been developed and refined, including foam targets or gas jets used to tailor the density, altering the geometry to attempt to focus refluxing electrons, or nanostructured targets to modify the dielectric permittivity tensor on the scale of the laser's wavelength as will be discussed in more detail in chapter 4.

1.3.3 X-ray free electron lasers

The advent of XFELs represented a major advancement in capability for WDM and HED research. The first XFEL to turn on in 2009, LCLS, is capable of providing $\sim 10^{12}$ photons of tunable x-rays with a 0.3% bandwidth in a pulse duration of $\mathcal{O}(10\,\text{fs})$ [14] in a Self-Amplified Spontaneous Emission (SASE) spectrum. The beam divergence of LCLS is measured at 2 µrad which compares very favourably with synchrotron sources ($\sim$ mrad divergence), producing peak spectral brightness $\sim 10^{34}$ photons/sr/mm^2/0 1% bandwidth shown in Fig. 1.3. The size of the focal spot can be tailored in experiments to probe the nanoscale of interactions, or act as a spatially localised pump, with achievable focal spot sizes of 90 nm × 110 nm Full Width Half Max (FWHM) [29]. While pulse energies of $\sim$2 mJ are smaller than optical lasers, the pulse can be absorbed over the µm attenuation length of a

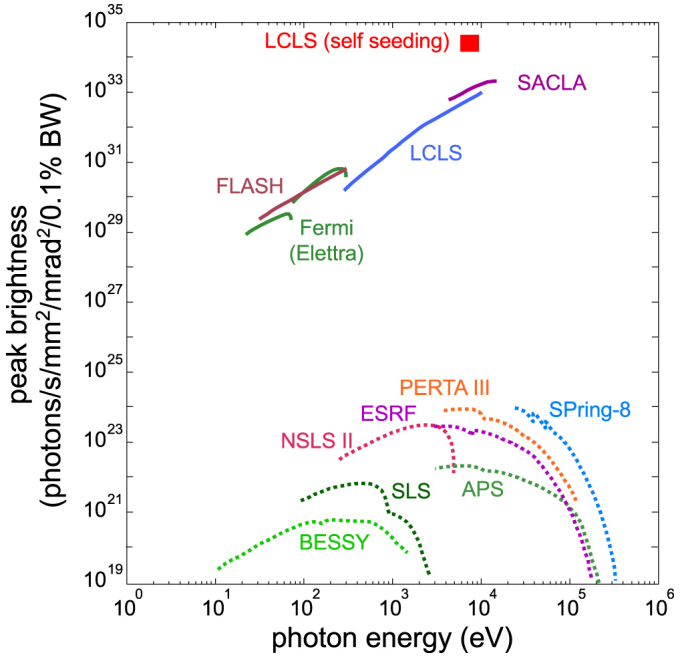

Figure 1.3: A comparison of peak x-ray brightness of various x-ray light sources against photon energy, reproduced from Glenzer *et al.* [15]. While 3rd generation x-ray light sources can currently achieve higher photon energies, the switch-on of the first XFEL, Linac Coherent Light Source (LCLS), represented a billion-times increase in peak brightness for hard x-rays.

solid density target with an enhanced absorption cross-section by coupling directly to atomic core electrons which is sufficient to generate states in excess of 100 eV bulk temperature while remaining at solid density [11].

The ability to heat targets volumetrically with XFELs, removing large plasma parameter gradients, allows experiments to occur on a much more rapid timescale as they are not reliant on the indirect heating such as hot electrons from short pulse lasers over durations of 1 ps. The timescale required for heating in optical laser studies limits the cases that can be investigated, as it often exceeds the lifetime of short-lived WDM states. The ability to generate (and probe) HED on such short timescales that the interatomic distances can be considered static has

been exploited in the multitude of branches of study enhanced by brighter x-ray light sources, in diffract before destroy schemes [30], single particle imaging [31], ultrafast chemistry [32] and Matter in Extreme Conditions (MEC) [33, 13].

1.4 Non-thermal plasmas

The short timescale of target heating in short-pulse laser-plasma interaction couples to a largely non-thermal distribution of electron energies, with significant MeV-level electron population from relativistic intensities. XFELs generate both directly photoionized electrons as well as subsequent auger decay electrons emitted with multi-keV energies. While hot electron equilibration time is still extremely fast due to their high speeds and therefore collisional rates, a non-thermal population can have significant effects on the plasma as it equilibrates [34].

When an XFEL irradiates a target, due to the narrow bandwidth photoelectrons rapidly populate the continuum Density Of States (DOS) at one energy, and through subsequent collisions can further ionize the plasma. At extreme intensities which can surpass 10^5 photons/atom [35], atoms can be multiply photoionized before they have time to recombine, generating exotic states with no core K-shell electrons but fully populated outer shells [11, 13, 36]. If in a truly radiation-dominated regime where ionic populations become decoupled, then as auger decays remove two electrons there could be an oscillating population with only even or odd ion charges significantly populated. The exotic distributions it is possible to produce using extreme brightness x-ray light sources have correspondingly have complicated emission profiles. Despite the possibly significant non-thermal electron distribution, the bulk plasma can thermalize with charge state distributions

corresponding to extreme temperatures, and collisional radiative models can be used to interpret emission spectra.

One of the key advantages of using x-rays is that they are a powerful diagnostic tool, as x-ray emission can be directly linked to ionic populations for optically thin systems, and emission lines can be observed well above a Bremstrahlung background. Even small scattering cross sections can become visible as it is possible to resolve single photons incident on area detectors. X-ray Emission Spectroscopy (XES) in WDM suffers the substantial difficulty that opacities in the soft x-ray regime are large, affecting observations of the interior of any system [37]. The capabilities of detectors as well as key x-ray diagnostic techniques relevant to this work will be discussed in more detail in Chapter 2.

1.5 Structure of thesis

Chapter 1 lays the foundation of this work, introducing how isochoric systems have previously, and are currently being studied, as well as how laser systems infrastructure has developed to expand the range of possibilities. The constantly upgrading state of the art diagnostic capabilities and analysis techniques required to deal with the quantities of data they produce are detailed in chapter 2.

The key original work presented in this thesis, using some of the techniques from chapter 2, is presented in chapters 3 through 5, where a variety of experimental efforts are detailed in either novel methods of creating well characterised extreme state of matter are detailed, or corresponding efforts to fully diagnose and understand their evolution in time.

Chapters 3 focuses on an experiment to heat and diagnose WDM systems using

XFEL-only pump and probe measurements to extract well bounded temperature and Ionization Potential Depression (IPD) measurements of transient states.

Chapter 4 presents efforts to scale highly optically-absorbent nanostructured laser targets to relativistic intensities, along with understanding their dynamical evolution as nanoscale target modulations homogenise to a uniform bulk. Achieving a complete picture of time-resolved laser-target interaction then aids the discussion of how to improve target fabrication for applications as high-fluence x-ray, charged particle and neutron sources.

Chapter 5 describes the efforts to extend isochoric studies at XFELs to higher Z elements with higher photon energies. X-ray emission spectra of isochorically heated Iron are described, and the information it provides on atomic structure and collisional rates for HED systems.

Finally, chapter 6 concludes this thesis with a summary of the work presented, and a discussion of future efforts relevant to this project.

Work described throughout this thesis has formed or contributed toward a number of manuscripts submitted to journals for publication, as part of large collaborative efforts to investigate plasma and material properties in extreme conditions. Much of the experimental work detailed here is based on data from beam time allocations via competitive proposal review process – many of which by necessity of the limited timeline of the project were submitted before this work began – only possible due to the the efforts of a large number of people beforehand. Relevant contributions and useful discussions are in particular due to a small group of people: Dr. Orlando Ciricosta and Dr. Ryan Royle, former postdoc's in the group in Oxford, for doing a lot of the experimental planning, Dr. Thomas Preston (EuXFEL)

and Dr. David McGonegle, for many useful discussions on spectral analysis techniques, and Professor Robin Marjoribanks (University of Toronto), for his work on manufacturing and characterisation of nanowire targets. Dr. Matthew Hill (AWE), for experimental data and assistance throughout in analysing data from Orion. In addition the support of Dr. Sam Vinko and Professor Justin Wark has been invaluable in approaches to experimental work and data analysis techniques.

1.6 Author Contributions

Due to the large, collaborative nature of experiments at international user facilities such as LCLS, EuXFEL and Orion, a large team was involved in much of the work presented in this thesis. The distinct contributions of the author and specific contributions from collaborators are outlined here.

Spectral analysis and single photon counting techniques described within were developed by the author for use on experimental data, based on discussions primarily with A. J. F. Miscampbell, D. A. McGonegle and S. M. Vinko. A code for droplet-based Single Photon Counting (SPC) was based on the previous work of O. Ciricosta.

Experimental work at Orion was performed by the Materials Modelling Group at AWE, and the experiment was led by M. P. Hill. Targets for the experiment were provided by the group of J. J. Rocca (University of Colorado). The author developed the spectral fitting procedure as described in Chapter 4. Additional Particle-In-Cell (PIC) simulations were performed by R. Royle. Details of the experiment have been submitted for publication by Hill *et. al* [38], which was contributed to by the author, and a follow-up publication has been submitted

detailing the methods used to model the spectra. The ELFIE experiment was attended by the author, led by R. S. Marjoribanks who provided the nanowire targets. Scanning electron microscope images of nanowire targets are thanks to A. J. F. Miscampbell. The low- and mid-intensity dielectric description of nanowire absorption was developed by R. S. Marjoribanks and G. Kulcsàr, as described in Marjoribanks *et. al* [39].

Data on RIXS from LCLS was gathered on beam time granted to R. S. Marjoribanks, which the author attended. All spectral analysis and modelling during and subsequently was performed by the author, with the assistance of S. M. Vinko. Density Functional Theory (DFT) simulations to calculate the DOS of Ni were performed by S. M. Vinko. Details of the experiment and measurements have been submitted as a manuscript for publication [40].

Data presented on the isochoric heating of Fe foils using the LCLS XFEL is thanks to H.J. Lee (SLAC), with all spectral processing and line position analysis presented here as a result of work performed by the author.

The interpretation of results from experiments, spectral analysis and modelling methods described within are the result of detailed discussions between the author and primarily S. M. Vinko and J. S. Wark, and their contributions in the development of this work was crucial.

The author is supported by EPSRC (project #1964304) and Oxford Centre for High Energy-Density Science (OxCHEDS). Use of the LCLS, SLAC is supported by the U.S. Department of Energy, Office of Science, Office of Basic Energy Sciences under Contract No. DE-AC02-76SF00515. The MEC instrument was supported by the U.S. Department of Energy, Office of Science, Office of Fusion Energy

Sciences under contract no. SF00515.

2 X-ray emission and scattering diagnostics and analysis

X-ray diagnostics of WDM serve the purpose of probing the bulk thermodynamic state of the system, attempting to bypass the large opacity at soft x-ray energies in order to probe the core of a heated system with penetrating radiation.

X-ray Emission Spectroscopy is used to observe the characteristic emission lines of an atom when a bound electron is excited, which can occur by incident x-rays, hot electrons, or as part of a thermal system. Using an incident x-ray probe and measuring shifts in the photon energy can access a wide variety of excitations in a system, as a higher energy analogue of Raman spectroscopy. Analysis of the x-ray emission spectrum can provide details on the ionic composition of the sample, relative populations of electron configurations, and spacing between atomic energy levels [11, 41, 42, 43, 44]. This can also be extended to resonant Raman x-ray spectroscopy, also known as RIXS, whereby the photon-in/photon-out process is resonant with an x-ray absorption edge, significantly enhancing the cross-section sometimes by an order of magnitude. RIXS also allows probing of elementary excitations which the energy and momentum of the photon can couple to, including phonons, orbital excitations and magnetic excitations.

X-ray scattering diagnostics are among the most frequently probed signals which can be used to infer structure, temperature, and ionization. The differential scattering cross section, i.e. the probability of a photon to scatter the outgoing photon into solid angle $d\Omega_{\mathbf{k}_2}$ with energy loss $\omega - \Omega$ is found from the starting

point of the interaction Hamiltonian

$$H_{int} = \sum_j \frac{e^2}{2mc^2}|\mathbf{A}_j|^2 + \sum_j \frac{e}{mc}\mathbf{p}_j \cdot \mathbf{A}_j \tag{45}$$

where $\mathbf{A}$ is the vector potential of the electromagnetic field and $\mathbf{p}$ is the electron momentum. Here the electron-photon interaction has the lowest order ($\mathbf{A}^2$) and second order perturbations ($\mathbf{p} \cdot \mathbf{A}$), smaller by a factor of $\hbar\omega/mc^2 \ll 1$ where $\hbar\omega \sim 10\,\text{keV}$ is used for x-ray sources.

The scattering cross section from this potential is given by the Kramers-Heisenberg formula [45]:

$$\begin{aligned}\frac{d^2\sigma}{d\Omega_{\mathbf{k}_2} d\omega} = \frac{\omega}{\Omega}\left(\frac{e^2}{mc^2}\right)^2 \delta(E_f - E_i + \omega - \Omega)\times \\ \Bigg|\langle f|\rho_{\mathbf{k}_1-\mathbf{k}_2}|i\rangle\,(\boldsymbol{\eta}_1\cdot\boldsymbol{\eta}_2) + \\ \frac{1}{m}\sum_n\left(\frac{\langle f|\mathbf{p}(\mathbf{k}_2)\cdot\boldsymbol{\eta}_2|n\rangle\langle n|\mathbf{p}(-\mathbf{k}_1)\cdot\boldsymbol{\eta}_1|i\rangle}{E_n - E_i - \Omega} + \right. \\ \left.\frac{\langle f|\mathbf{p}(\mathbf{k}_1)\cdot\boldsymbol{\eta}_1|n\rangle\langle n|\mathbf{p}(-\mathbf{k}_2)\cdot\boldsymbol{\eta}_2|i\rangle}{E_n - E_i + \omega}\right)\Bigg|^2,\end{aligned} \tag{46}$$

where $|i\rangle$, $|n\rangle$ and $|f\rangle$ are initial, intermediate, and final states of the system, with respective energies E_i, E_n and E_f. $\boldsymbol{\eta}_1$ and $\boldsymbol{\eta}_2$ are unit polarization vectors of incident and outgoing photons, with energies Ω and ω respectively. Here the plane wave dependence has been omitted for convenience, with $\rho_{\mathbf{k}} = \sum_j \exp(-i\mathbf{k}\cdot\mathbf{r}_j)$ and $\mathbf{p}(\mathbf{k}) = \sum_j \mathbf{p}_j \exp(-i\mathbf{k}\cdot\mathbf{r}_j)$.

The first matrix term in equation (46) arises from the $\mathbf{A}^2$ interaction, and when taken independently results in the X-ray Thomson Scattering (XRTS) cross section, involving the dynamic structure factor as the transform of the time-dependent

density-density correlation function as a function of scattering vector and photon energy loss:

$$S(\mathbf{q},\omega) = \frac{1}{2\pi}\int_{-\infty}^{\infty} dt\ \exp(i\omega t)\langle i|\rho_{\mathbf{q}}(t)\rho_{-\mathbf{q}}|i\rangle, \tag{47}$$

encapsulating all system-specific properties and providing information on elementary excitations caused by charge fluctuations in a material.

The typical treatment of dense plasma separates the structure factor into several components by splitting the electron density into core- and free-electrons:

$$S(\mathbf{q},\omega) = |f_i(q) + f_e(q)|^2\, S_{ii}(q,\omega) + S_{ff}(q,\omega) + S_{bf}(q,\omega), \tag{48}$$

where S_{ii} is the ionic structure factor, f_i and f_e are the form factors of the ion and surrounding electron charge distribution. S_{ff} contains information on the scattering from free charges, while S_{bf} results from bound-free transitions, Raman transitions. These interactions take place over different photon energy regimes, so can often be probed in isolation and information on each can be extracted.

The second order terms in equation (46) contains the RIXS cross-section, which is enhanced when tuned to an absorption edge. Here the process can be seen as a second order coherent absorption from initial state, $|i\rangle$, to a short-lived intermediate state, $|n\rangle$, before re-emission to the final state, $|f\rangle$. Although the description initially appears to represent simple x-ray absorption and then emission, the lifetime of the intermediate state is given by a non-energy conserving absorption event, however the two electron process as a whole is energy conserving. RIXS has the potential to provide much more information than Thomson scattering, as it is a function of both incident and outgoing photon energies, Ω and ω rather than only

through the energy loss, $\Omega - \omega$, and can therefore provide more detail about the elementary excitations. Details of how this can be pursued will be explored more fully in chapter 3.

2.1 Bragg spectroscopy

In order to resolve the x-ray emission or scattering from a system, the primary diagnostic is an energy resolving spectrometer [46]. At x-ray energies, some crystal lattice spacing's are ideal for serving as a Bragg spectrometer as the plane spacing is comparable with x-ray emission wavelengths. A simple setup uses a small emitting volume from a laser focal spot reflecting from a flat crystal onto a detector as shown in Fig. 2.1.

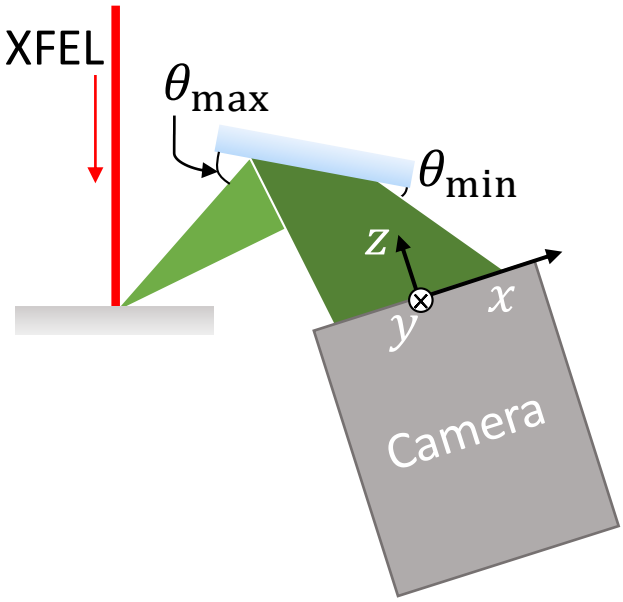

Figure 2.1: A simple flat crystal Bragg spectrometer. Emission from the target is dispersed in energy according to the angle of reflection from the crystal.

A simple application of first order Bragg's law yields

$$\lambda = \frac{hc}{eE\,[\mathrm{eV}]} = 2d\sin(\theta) \tag{49}$$

however the projection of this angle onto the two dimensional camera plane leads to a generalised conic section problem. Each photon energy will illuminate the intersection of a cone and the camera face. In addition, those sections of the camera that are further away from the target subtend a smaller solid angle of the emission, which must be normalized to give true line ratio observations. For the first issue, Bragg's law can be modified to give:

$$E(x,y,\bar{\theta}) = \frac{hc}{2de}\frac{\left\| D\begin{pmatrix}\cos\bar{\theta}\\0\\\sin\bar{\theta}\end{pmatrix} + \mathbf{R}\begin{pmatrix}x\\y\\0\end{pmatrix}\right\|}{D\sin\bar{\theta} + \begin{pmatrix}0&0&1\end{pmatrix}\mathbf{R}\begin{pmatrix}x\\y\\0\end{pmatrix}}. \tag{50}$$

Additional parameters introduced here are

D The distance to the camera origin

R General 3D rotation matrix, $\mathbf{R} = \mathbf{R}_y(\alpha_y)\mathbf{R}_x(\alpha_x)\mathbf{R}_z(\alpha_z)$, where coordinate axes are labelled in figure 2.1

$\bar{\boldsymbol{\theta}}$ The x-ray crystal diffraction angle at the camera origin, $(0,0)$.

Evaluating the terms in equation (50), where c_i and s_i represent $\cos(\alpha_i)$ and

$\sin(\alpha_i)$ respectively:

$$\begin{aligned}\left(D\sin\bar{\theta} + x(c_y s_x s_z - c_z s_y) + y(c_y c_z s_x + s_y s_z)\right)^2 = \\ \left(\frac{hc}{2deE}\right)^2 \left(D^2 + x^2 + y^2 + 2D\left(\cos\bar{\theta}\left(x(c_y c_z + s_x s_y s_z) + y(c_z s_x s_y - c_y s_z)\right)\right.\right. \\ \left.\left. + \sin\bar{\theta}\left(x(c_y s_x s_z - c_z s_y) + y(c_y c_z s_x + s_y s_z)\right)\right)\right). \quad (51)\end{aligned}$$

Finally collecting terms into the form of a generalized conic section matrix

$$\begin{pmatrix} x \\ y \\ D \end{pmatrix}^T \left(\begin{pmatrix} 1 & 0 & (c_{\bar{\theta}+y} c_z + s_{\bar{\theta}+y} s_x s_z) \\ 0 & 1 & (s_{\bar{\theta}+y} c_z s_x - c_{\bar{\theta}+y} s_z) \\ (c_{\bar{\theta}+y} c_z + s_{\bar{\theta}+y} s_x s_z) & (s_{\bar{\theta}+y} c_z s_x - c_{\bar{\theta}+y} s_z) & 1 \end{pmatrix} \right.$$
$$\left. + \left(\frac{2deE}{hc}\right)^2 \begin{pmatrix} c_y s_x s_z - c_z s_y \\ c_y c_z s_x + s_y s_z \\ s_{\bar{\theta}} \end{pmatrix} \begin{pmatrix} c_y s_x s_z - c_z s_y \\ c_y c_z s_x + s_y s_z \\ s_{\bar{\theta}} \end{pmatrix}^T \right) \begin{pmatrix} x \\ y \\ D \end{pmatrix} = 0. \quad (52)$$

This, although it may seem a complicated form, is easily computed and is more useful for optimization as the 5 input parameters of $(\bar{\theta}, D, \boldsymbol{\alpha})$ are the normal set of experimentally measurable parameters, in addition to the crystal $2d$ spacing.

From this energy dispersion relation across the face of the camera, a spectrum can be formed by integrating along lines of constant energy. If complete knowledge of the emission function $S(E)$, i.e. the photons/sr/eV, is assumed, then the photon probability density function on the recovered image would take the form

$$I(x, y|\boldsymbol{\theta}) = S\left(E(x, y, \boldsymbol{\theta})\right) \frac{d^2\Omega(x, y, \boldsymbol{\theta})}{dxdy} |\nabla_{x,y} E(x, y, \boldsymbol{\theta})|, \quad (53)$$

where here the differential solid angle and energy dispersion are included. The energy dependence of any filtering used is assumed to be incorporated in the

dependence of $S(\mathbf{E})$. The differential solid angle can be found from the general result for a distant plane by including an offset for the point of closest approach of the camera plane to the crystal reflection of the target. A simple projection of the camera origin onto the rotated plane normal provides the equation of the plane, recalling that the target-camera vector must be reflected in the plane of the crystal.

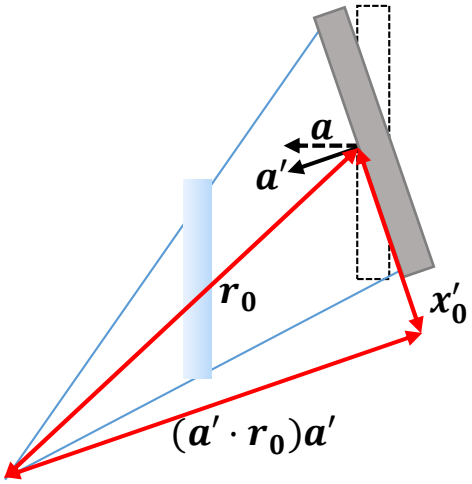

Figure 2.2: Vector relations for calculating the solid angle projection required to normalize spectral emission

$$\mathbf{a}' = \mathbf{R}\hat{\mathbf{z}} \tag{54}$$

$$\mathbf{r}_0 = D \begin{pmatrix} \cos(\bar{\theta}) \\ 0 \\ \sin(\bar{\theta}) \end{pmatrix} \tag{55}$$

$$D' = (\mathbf{a}' \cdot \mathbf{r}_0) \tag{56}$$

$$\mathbf{x}_0 = D'\mathbf{a}' \tag{57}$$

$$\mathbf{x}_0' = \mathbf{r}_0 - \mathbf{x}_0 \tag{58}$$

$$\mathbf{x}' = (\mathbf{x} + \mathbf{R}^{-1}\mathbf{x}_0') \tag{59}$$

$$\frac{d^2\Omega}{dxdy} = \frac{D'}{(x'^2 + y'^2 + D'^2)^{\frac{3}{2}}}. \tag{60}$$

The corresponding vectors and their projections are shown in Fig. 2.2. The optimal spectral reconstruction is now found by integrating the collected spectral emission along lines of constant energy.

$$\tilde{S}(E|\boldsymbol{\theta}) = \frac{\int_{E'(x,y,\boldsymbol{\theta})=E} d\ell \; I(x,y)}{\int_{E'(x,y,\boldsymbol{\theta})=E} d\ell \; \frac{d^2\Omega(x,y,\boldsymbol{\theta})}{dxdy} |\nabla_{x,y} E(x,y,\boldsymbol{\theta})|} \tag{61}$$

Up until now a perfect image of the photon probability density function has been dealt with, however any experimental detector data is digitized - either within a camera architecture, or when scanning film or image plate afterwards. This digitization necessarily has finite resolution, so an image would no longer have a continuous intensity, $I(x, y)$, rather a discretized one. The intensity at a pixel (i, j) will now depend on the total emission across that entire pixel. Another factor is the quantization of light, whereby while the average probability of detection on a pixel is continuous, this sample is drawn from a Poisson distribution. Finally, in

the process of detecting x-ray quanta, there is further noise in the amplification. Including these effects, a description of the image becomes:

$$I_{ij}(\boldsymbol{\theta}) = Poiss\left(\int_{x_i}^{x_i+\Delta x} dx \int_{y_i}^{y_i+\Delta y} dy\ I(x,y|\boldsymbol{\theta})\right) \times (1+\Gamma\eta_1) + \zeta\eta_2 \tag{62}$$

for a pixel size $(\Delta x, \Delta y)$, with random noise terms η with zero mean and $\langle \eta_i \eta_j \rangle = \delta_{ij}$. The magnitude of absolute and relative noise, ζ and Γ respectively, is determined by the particular detector. The inversion of this problem to find the corresponding input $\boldsymbol{\theta}$ and the spectral emission $S(E)$ is an extremely difficult one, however using the continuous approximation given above, adjusted to ensure that it is photon number conserving, a good estimate for the spectral emission function can be arrived at, depending on the number and size of the detector pixels. Beyond this it would be possible to perform a maximum likelihood estimator by simulating the entire image, however this would become computationally expensive as facilities such as LCLS output 0.5 Mpixel images at 120 Hz, and newer facilities such as EuXFEL capable of running at 4.5 MHz.

Figure 2.3 shows an example spectrum and its inversion, including a variety of spectral features of a continuum (bremsstrahlung), a broad (30 eV) emission line, and a delta function to show the limiting case in spectral reconstruction.

Parameters used here were representative values used in a hard x-ray spectrometer:

$$2d = 2.848\,\text{Å (For LiF 220)} \tag{63}$$

$$\bar{\theta} = 40^\circ \tag{64}$$

$$D = 160\,\text{mm} \tag{65}$$

$$(\alpha_x, \alpha_y, \alpha_z) = (5^\circ, \bar{\theta}, 12^\circ) \tag{66}$$

$$\Gamma,\ \zeta = .04 \tag{67}$$

$$\Delta x,\ \Delta y = 200\,\mu\text{m}. \tag{68}$$

α_y is taken as $\bar{\theta}$ in order to maximise the energy range across the image by making the camera perpendicular to the incoming diffracted x-rays at the centre of the image. In order to conserve photon numbers on the image, the image was integrated in narrow energy bands, while still subdividing pixels into multiple energy bins.

While the instrument function FWHM of a spectrum reconstructed in this way can be comparable to a naive pixel-shifting approach (whereby each pixel value in its entirety is attributed to the energy bin of the pixel centre) as shown in Fig. 2.3, the retrieved spectrum is much less susceptible to the influence of noise as pixel-shifting results in a small number of pixels per energy bin. The form of the retrieved spectrum extends well to the limit of a continuous energy scale, in order to accurately diagnose whether the instrument is the limiting factor in measured spectral resolution. The instrument function width is easily found by line integrating the discretized energy dispersion gradient over each pixel resulting in an almost linear dependence between 5.9 eV to 6.7 eV FWHM for the above

[1]Note that the number of points in the energy scale had to be reduced for the pixel shifting algorithm to ensure that energy bins always contained ~ 10 pixels

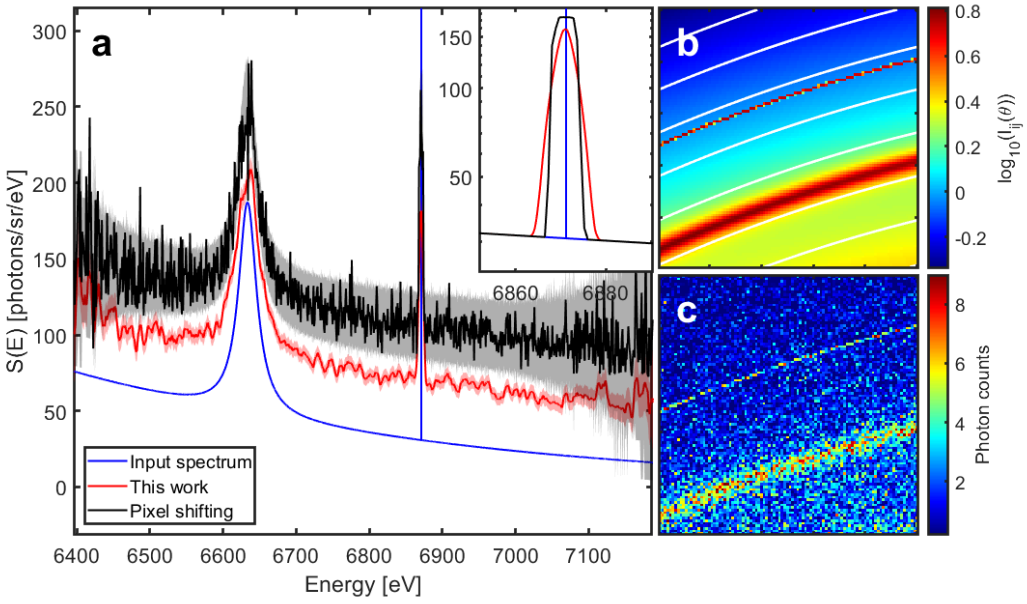

Figure 2.3: An example inversion problem for an x-ray spectrometer, showing (a) the input and reconstructed spectra, offset for visibility, where the coloured band shows the expected Poisson error[1]. (a, inset) Reconstruction of delta function spectral emission without added noise, demonstrating the instrument function. (b) The discretized photon probability density function from Eqs. (53, 62) on a (100×100) pixel image with white iso-energetic contour lines at each multiple 100 eV, and (c) the Poisson sampled image from Eq. (62), with noise and charge spreading, which was used to reconstruct the emission spectrum in (a)

case, however this is a geometry and detector specific calculation. The variation in range of azimuthal angle covered and the distance to the detector compared with pixel size gives a range of $E/\Delta E$ from 1050 to 1100, with discontinuities when the energy contour intersects a corner of the image shown in figure 2.4. Note also the size of the Poisson error increasing towards the limits of the energy scale, as the length of energy contours across the image is shorter, resulting in a smaller solid angle collection area.

In addition to the pixel broadening discussed, the effect of crystal rocking curve

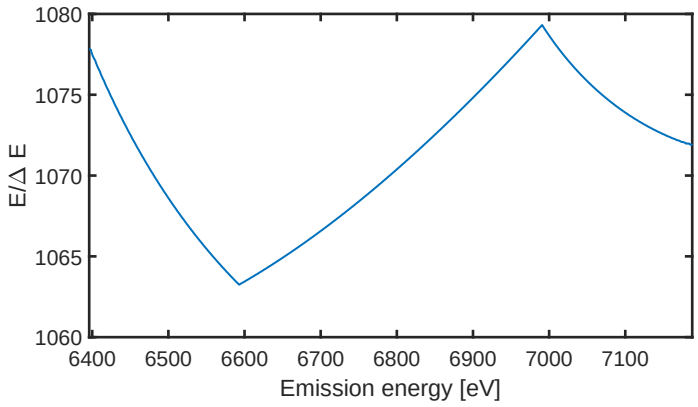

Figure 2.4: Plot of the energy resolution function of the example Bragg spectrum shown in figure 2.3 as a result of pixel size, showing the changes in resolution at the corners of the image to demonstrate the requirement for an instrument and geometry specific calculation.

width and source broadening are assumed to be included in the measured spectrum $S(E)$. Charge spreading also affects the resolution of the recovered spectrum, and efforts to minimize the impact will be detailed in section 2.3. In addition it is clear from the form of the noise discussed in equation (62) that if pixels without a photon present are included, extra noise terms are present in the final spectrum, which should be minimised. As the limitations of the analysis are inherently detector specific, the detectors fielded on experiments relevant to this work will be discussed before advancing the analytical aspects.

2.2 X-ray detectors

X-ray detectors come in many shapes and sizes, depending on their application and experimental considerations. By and large they can be separated into two categories - analogue and digital.

Beginning with analogue detectors, comprising of film, and image plates [47].

These are useful in scenarios where a digital device would not fit, or would be affected by Electromagnetic Pulse (EMP). In addition, the low cost of x-ray film makes it much preferable to use in the case where emission intensity is largely unknown to avoid damaging an expensive detector. The major difficulty in using analogue detectors is characterising the response sufficiently to perform further meaningful measures on a collected emission spectrum / x-ray radiography image. As the gain is often non-linear, approaching some saturation value of photons/unit area, absolutely calibrated devices are rare. In addition, for image plates, the image of collected x-rays has an associated decay time that is again highly non-linear. When combined with the fact that in order to perform quantitative analysis of collected emission, the data will necessarily be digitized on a scanner (which is assumed to have a linear gain), the difficulties of calibrating such a device become evident. Further adjustments to the collected data can come from inhomogeneities in the film, strain, creasing or friction. there is also a certain lack of reproducability intrinsic in using replaceable parts, whereby slight differences in the geometry of image plate placement affect the radiation distribution. Analogue x-ray detectors are often not suitable for time resolved measurements, the dynamic range is often insufficient, and suffer from "intrinsic chemical fog" [48], reducing the detector quantum efficiency.

Digital detectors also come in assorted forms and form factors depending on their intended usage. For example Cornell-SLAC Pixel-Array Detectors (CSPADs) [49] and their successor the ePix10k [50] are optimised for collecting diffraction data over a large q-range by being both physically large and having substantial dynamic range capabilities via gain switching. This specialisation comes at the cost of large

pixel sizes of 100 µm × 100 µm as it requires large charge reservoirs.

In order to satisfy the requirements of XES, requiring a high spatial resolution and very low noise, one solution is the ePix100 camera [51] with high quantum efficiency across the tender and hard x-rays produced at LCLS with a maximum signal of 100 8 keV photons per 50 µm × 50 µm pixel. These detectors rely on the photoexcitation of a Si sensor, generating a number of photoelectrons corresponding to the x-ray energy. For Si-based detectors the average energy required for generation of one electron-hole pair in the sensor layer is 3.65 eV, resulting in an applicable photon energy between approximately 30 eV to 20 keV based on small signal amplification and the required absorption depth of the sensor layer respectively. The incident photons generate a charge cloud in the sensor layer proportional to the photon energy which can then be coherently amplified for readout. The absorption process has a spread in the number of e-h pairs produced which can be found using the fano factor, $f = 0.12$ for Silicon [52], whereby for an average $N_e = \hbar\omega/[3.65\,\mathrm{eV}]$ will result in a width of $\pm 2.355\sqrt{fN_e}$ where the factor of 2.355 relates the standard deviation to the FWHM. The electrons are collected in a charge depletion region, to then be read out by the detector with its corresponding gain – schematically shown in figure 2.5 – outputting a signal level in Analogue-to-Digital Unit (ADU). If the charge is generated in the sensor layer between two pixels, the charge cloud can split between them. For lower energy x-rays, where the charge is generated closer to the surface of the sensor this becomes more of an issue as the number of electrons is low and the charge cloud has a greater distance to diffuse over before being collected. Another example is using a Charge Coupled Device (CCD), whereby pixel values are read out in a

serial register, shifting the 'bucket' of electric charge along. The architecture of the CCD can leave some residual charge leading to further photon 'smearing'. A schematic view of charge generation, spread and readout is shown in figure 2.5, as well as example detection events on an image of single and multi-photon clusters with limited charge spreading.

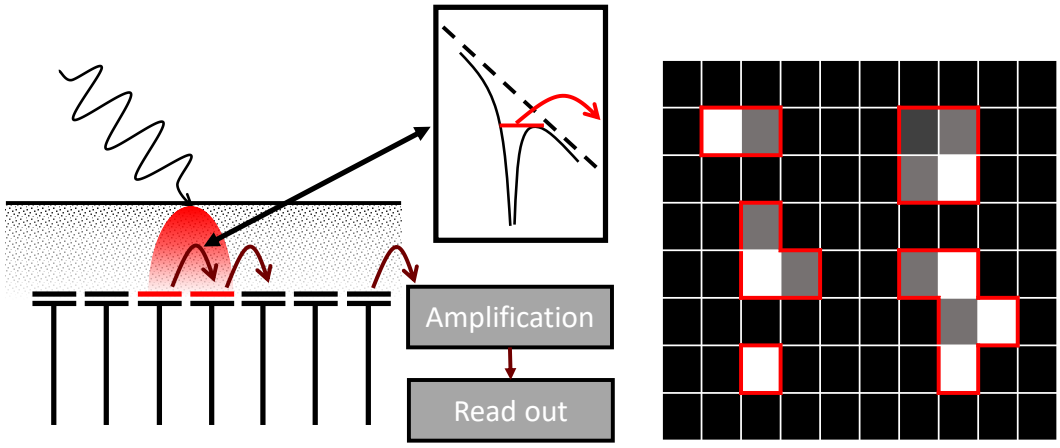

Figure 2.5: Schematic view of CCD charge generation in a sensor layer, collection in charge depletion regions, and serial amplification and readout. Example detection events are also shown for single and multi-photon clusters on the image with limited charge spreading. Charge generated higher in the sensor layer due to a small attenuation length of low energy photons has a greater distance to diffuse before being collected in charge depletion regions (i.e. pixels), and therefore greater noise as well as lower total charge.

Importantly, many of the detectors discussed are capable of resolving single photon events, whereby the collected intensity must be viewed as having been drawn from a Poisson distribution with some expectation value that must be reconstructed to find the emission function. Droplet algorithms can reconstruct smeared charge clouds into a photon detection event, returning the energy resolution attributable to the amplification stage. The statistics of single-, or often

multi-photon counting is a rich topic in optimisation to recover the best estimate of collected emission, with stringent requirements on characterising the detector response.

2.3 Single photon counting

Using the single-photon resolving capabilities of CCDs and x-ray cameras, a spectrum can be reconstructed purely from the localised charge generated from a photon absorption. Care must be taken that the charge collected is the result of a single photon, and data must therefore be sufficiently sparse across the image making multiphoton events rare. Fig. 2.6 shows part of a collected image of emission from a Hafnium foil heated with the ELFIE short pulse optical laser at LULI, along with a simple droplet reconstruction of detected photons showing the 3 L-shell emission lines. The 'droplets' here are defined as a finite set of allowed polyomino forms of the charge accumulated in a photon detection event on the image, from which a spectrum may be formed as a histogram in the detected charge (which is proportional to energy). The set of allowed droplets is chosen due to the point-spread function on the camera, and to limit the noise accumulated over a large number of pixels which may contain multiple photon events where the charge generated from each photon becomes indistinguishable. As the system was optically heated, the position of the emission lines will be shifted compared to the cold case due to ionization, however the shifts would be small compared with the resolution of the SPC spectrum, which is 200 eV for two pixel events, with additional noise accumulated over larger droplets. As pixels on the Andor camera used were only 13.5 µm × 13.5 µm, charge spreading is significant, as seen

in Fig. 2.6b where there are very few photons confined to single pixels. In order to ensure multi-photon events were rare, the detector was placed 4.5 m away from the interaction, and had an additional 300 µm Mylar + 60 µm Al filter to screen out low energy photons.

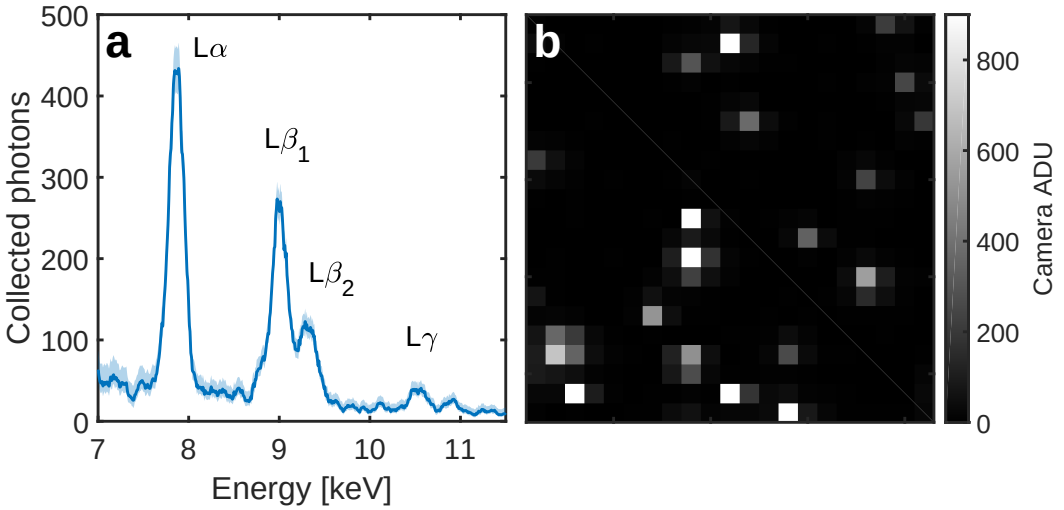

Figure 2.6: SPC spectrum of 140 µm Hf foil heated with the ELFIE laser (350 fs, ∼7.5 J, 10 µm FWHM, $\lambda = 1.057$ µm) collected by 4 Mpix Andor iKon-L SO CCD on 13.5 µm × 13.5 µm pixels, located 4.5 m away from the interaction, showing (a) the retrieved spectrum of 2-pixel photon detection events (to avoid additional noise) and (b) part of the collected image where photon charge spreading can be seen. Retrieved peak widths are 200 eV broad, corresponding to an e-h to ADU ratio of 0.44, and a pixel noise of 15ADU. The error band is an estimate of the Poisson noise taken from Garwood [53]. More details of the experimental setup are described in chapter 4 and Fig. 4.3

When considering an image even without spreading of charge from photons to adjacent pixels, there is an upper limit on the level of signal that yields meaningful results. An exercise in indexing polyominos generated on an image by Poisson-sampling an average number of photons per pixel, and then computing the indistinguishable clusters, shows the measured cluster density deviating from

linearity and then inverting as average cluster size tends to infinity. The number of distinguishable single-pixel *and* single-photon events is 10% away from the linear response at only 0.021 photons/pixel average, and inverts at $p = 20\%$, as shown in Fig. 2.7, with charge spreading only exacerbating this effect. This dependence gives a fundamental limits to SPC in terms of not only the signal, but also the signal/noise achievable from such a diagnostic.

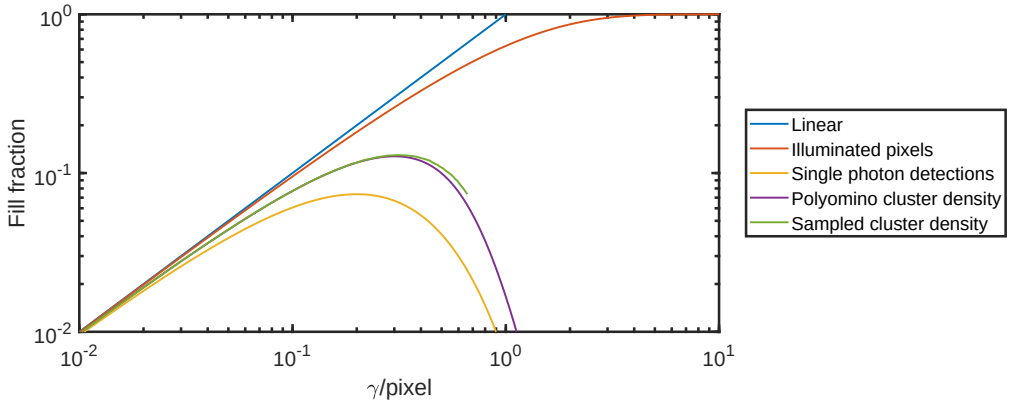

Figure 2.7: Plot showing the number of photon detection islands as a function of single-pixel Poisson detection likelihood (neglecting the effects of charge spreading) in comparison to the linear dependence. The number of fraction of single-pixel *and* single-photon detections rapidly deviates from linear, by 10% at 0.021 photons/pixel, and inverts at $p = 0.2$. The polyomino cluster density is only computed for terms up to 20 pixel clusters due to computational expense $\mathcal{O}(4^n/n)$, which peak at $p = 0.59$. A 1 Mpix simulation was performed to maximum $p = 0.66$, after which the number of clusters fell to single digits as they span the entire image.

While the ability to detect single photons can be used to form a spectrum from their amplification in the camera, the method of localising charge from one photon can also assist in Bragg spectroscopy, whereby in regions of low signal SPC is performed, with a multi-photon limit for intense parts of the spectrum, where the signal/noise ratio is already good - as seen between the continuum background and the peaked emission lines in Fig. 2.3c. In the region between single-photon

and many-photon parts of the spectrum, a careful consideration of the possible charge sharing modes is required in order to ensure that the spectrum is accurately retrieved, while minimising the accumulated noise.

To perform this analysis, the measured image values, x, can be transformed into a set of measures of the probabilities of having been due to detection of N_γ photons. By attributing each pixel to a set of probabilities, it in effect fixes low photon counts to discrete values, removing the associated noise, while the broad amplification noise from many photons will result in a natural width of the distribution over many possible photon numbers:

$$P(x|N_\gamma) = \frac{\exp\left(-\frac{1}{2}\frac{(x-N_\gamma)^2}{\Gamma N_\gamma+\zeta}\right)}{\sqrt{2\pi(\Gamma N_\gamma+\zeta)}}, \tag{69}$$

where here Γ is noise in due to the Fano factor in e-h pair charge generation and subsequent charge amplification, and ζ is the detector noise as in equation (62).

Using Bayes' theorem with a flat prior on the discrete $P(N_\gamma)$, and finding $P(x) = \sum_{n=0}^{\infty} P(x|N_\gamma = n)$ gives

$$P(N_\gamma|x) = P(x|N_\gamma)/\sum_n P(x|N_\gamma = n). \tag{70}$$

A one-sided probability distribution is taken for $x < 0$, $N_\gamma = 0$ to prevent the larger width of higher distributions attributing large noise values to positive photon counts. The non-linear transform of image pixel intensities, $\langle N_\gamma(x)\rangle = \sum_n nP(N_\gamma = n|x)$, is shown in figure 2.8, along with the standard deviation of the transform.

An example of applying the non-linear transform to a photon detection proba-

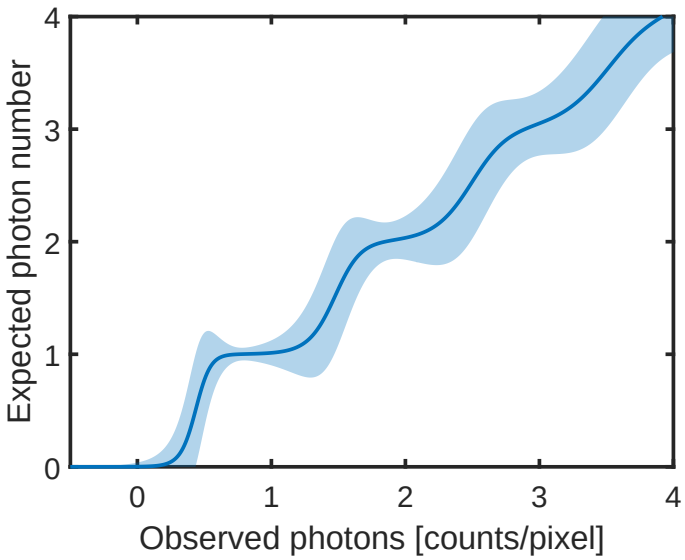

Figure 2.8: Non-linear transformation of observed image photon numbers into expected photon number/pixel as a result of Eq. (69) using noise value from (67). Low image counts are quickly fixed to discrete photon numbers, while the width of the expected charge distribution at higher photon numbers results in the trend becoming linear. When the response is between discrete photon numbers, the variance in the transform is larger.

bility distribution is shown in figure 2.9. The transform localises peaks at integer photon values, according to the expected broadening of the charge generated in the amplification process, allowing recovery of spectra with higher dynamic range and better quantification of noise than using the raw signal.

From this estimate of the discrete number of photons detected on each pixel, in order to construct the spectrum the mean of the Poisson distribution the camera values were drawn from must be found. Each pixel has a slightly different mean value due to the energy dispersion and differential solid angle. The spectrum can be formed by a simple integration of observed values and subsequent normalization by the accumulated projection factors. Error on the spectrum is found via considering

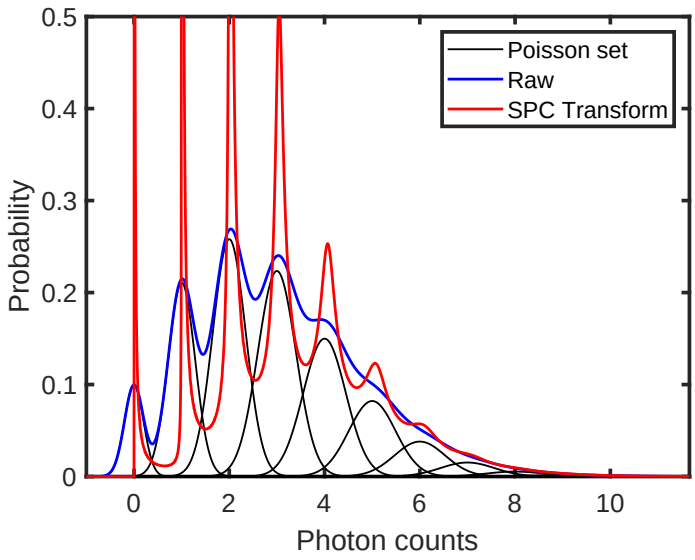

Figure 2.9: An example of applying the non-linear SPC transform to an expected detector probability density function for $\lambda = 3$. The raw signal is localised around discrete photon peaks according to the expected broadening of the charge generated on photon detection

the error the mean of the Poisson distribution from a single observation on each pixel. If I is used from equation (53) with again a flat prior on $P(I)$ and realising that $P(N_\gamma) = \int_0^\infty dI\ I^{N_\gamma} e^{-I}/\Gamma(N_\gamma + 1) = 1$:

$$N_\gamma = Poiss(I) \tag{71}$$

$$P(I|N_\gamma) = P(N_\gamma|I)P(I)/P(N_\gamma) = P(N_\gamma|I) \tag{72}$$

$$\langle I \rangle (N_\gamma) = \left\langle \int_0^\infty dI \; IP(I|N_\gamma) \right\rangle \tag{73}$$

$$= \langle N_\gamma \rangle + 1 \tag{74}$$

$$\langle I^2 \rangle (N_\gamma) = \left\langle \int_0^\infty dI \; I^2 P(I|N_\gamma) \right\rangle \tag{75}$$

$$= \langle \Gamma(N_\gamma + 3)/\Gamma(N_\gamma + 1) \rangle \tag{76}$$

$$\langle I^2 - \langle I \rangle^2 \rangle (N_\gamma) = \langle (N_\gamma + 2)(N_\gamma + 1) \rangle - (\langle N_\gamma \rangle + 1)^2 \tag{77}$$

$$= \langle N_\gamma^2 - \langle N_\gamma \rangle^2 \rangle + \langle N_\gamma \rangle + 1 \tag{78}$$

The variance in N_γ is retained in the variance of the estimate of the mean pixel photon probability in equation (78), and is found from the moments of the non-linear transform of image intensities in equation (70), shown as the standard deviation in Figure 2.8. The additional factor of $+1$ in equation (74) to estimate the average incident spectrum, while true when basing an estimate on the single-pixel, is removed when accumulating the spectrum over multiple pixels. Finally this variance in the estimate of the spectrum can be accumulated along the same line integral over the camera image as the spectral average, and normalized to integrated solid angle and dispersion as in equation 61 to give an estimate of the error in the measured spectrum. The combination of these transforms yields a very good reconstruction of the incident spectrum, as shown in Fig. 2.3, along with a consistent treatment of all sources of noise without resorting to an expensive maximum-likelihood estimator by reconstructing the entire image.

In regions of extremely low intensity on the image, if multiple adjacent pixels have been identified as belonging to a single photon event they can be attributed to the spectrum using the centre of mass of the charge cloud with the calculated detector instrument function after transforming using a modified form of equation (69) to account for the additional pixel noise. In regions of the image where it is not possible to identify the charge associated with a single photon, the linear dependence at high photon numbers recovers the intensity well. This non-linear transform of the image intensity works well in low-signal regimes, where detector noise terms are dominant, and recovers a linear dependence at high signal. The combination of single photon statistics with Bragg spectroscopy can deliver the excellent signal/noise of purely SPC diagnostics, while significantly improving the energy resolution from $\sim 200\,\mathrm{eV}$ to $\sim$ eV, depending on the particular spectrometer setup.

2.4 Ultra-fast x-ray streak cameras

The next detector to be detailed for the purposes of the analysis presented in this thesis is the X-ray Streak Camera (XRSC), which resolves emission in time. In conjunction with a focusing spectrometer this can be used to temporally resolve the x-ray emission spectrum, while sacrificing the one of the spectral dispersion directions as an X-ray Streaked Spectrometer (XRSS). Removing a secondary (azimuthal) spectral dispersion direction is often beneficial as it increases the x-ray intensity on the detector, which can be necessary to overcome the signal/noise limit on e.g. x-ray film. The most prevalent focusing crystals used in hard x-ray studies are higly-annealed or highly-oriented pyrolitic graphite, which can suffer

focal spot abberations due to the mosaic focusing [54]. The XRSS can also be used with a pinhole and slit for time- and spatially-resolved emission [55]. The XRSC diagnostic uses a spectrometer in a von Hamos geometry to focus the spectral dispersion to a line, where the target and detection plane are on the axis of a cylindrically-curved crystal. For the time resolution, the energy-dispersed spectrum is incident on a photocathode screen (plastic with CsI coating) to generate electrons, which are then passed through a time-dependent voltage to deflect electrons based on their time of arrival. An example detector geometry is shown in Fig. 2.10.

The quoted time resolution of commercial devices is 450 fs, however this is under optimal conditions. The time resolution can be decreased in order to increase detector efficiency when signal is very low. The photoelectrons produced at the far end of the cathode have a time delay compared to those closer to the target which must be corrected for in the data. In addition, there is an intensity broadening effect, whereby when the spectrum is intense enough to create many photoelectrons, their Coulomb interaction spreads out the bunch charge over the electron Time Of Flight (TOF) through the sweep plates. Further details of the point-spread function of XRSCs have been discussed by Von Marley [56].

2.5 Spectrometer calibration

Finally on the topic of spectroscopy, the calibration of these diagnostics must be discussed. Ensuring an accurate calibration is vital for measuring line position or shifts accurately, in order to determine the relevant emitting plasma conditions. Some spectrometers have a very simple calibration, such as a properly aligned von

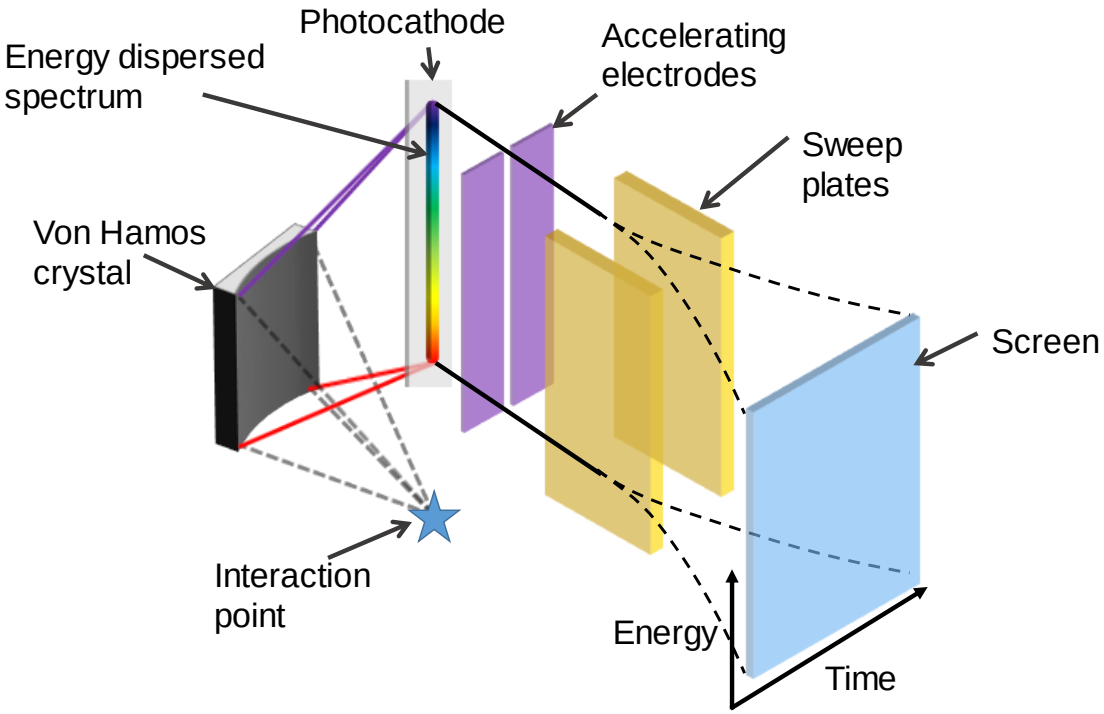

Figure 2.10: Key components of an x-ray streaked spectrometer diagnostic, showing the energy-dispersive von Hamos spectrometer, illuminating a photocathode sending electrons through a ramp voltage to the detector.

Hamos spectrometer, where

$$\mathbf{E}\text{eV} = \frac{hc}{2de}\frac{(R_0)^2 + (x + x_0)^2}{R_0} \tag{79}$$

given the radius of the cylindrically curved crystal, R_0, camera coordinate and origin, x and x_0 respectively. However a simple misalignment of the spectrometer axis with respect to the source, or the plane of the camera, results in massive modifications to this as the emission is no longer ideally confined to a single line, rather there is additional lateral dispersion. Beginning with the plane of the crystal, defined as

$$z_c = -\sqrt{R_0^2 - y^2} \tag{80}$$

and constructing the normal to the curved crystal plane, namely

$$\mathbf{a}_{crystal} = \begin{pmatrix} 0 \\ -z_c \\ -y \end{pmatrix}. \tag{81}$$

From the set of crystal coordinates, (x, y, z_c), adjusting the beam path for the misalignment in target position, $\mathbf{x}_t$ in the y and z directions (where $x_t = 0$ as translation along the cylinder axis is considered in the position of the camera plane), identifying the x-coordinate of the reflection on the crystal plane from the Bragg angle:

$$x_c = \sqrt{\frac{\left(\mathbf{a}_{crystal} \cdot \begin{pmatrix} 0 \\ y - y_t \\ z_c - z_t \end{pmatrix}\right)^2}{\sin(\theta)^2} - (y - y_t)^2 - (z - z_t)^2}. \tag{82}$$

One can then obtain the path of the reflected beam simply from the intercept at $\mathbf{x}_c$, and the gradient vector of the reflection in the crystal normal:

$$\mathbf{m} = (\mathbf{x}_c - \mathbf{x}_t) - 2(\mathbf{a}_{crystal} \cdot (\mathbf{x}_c - \mathbf{x}_t))\mathbf{a}_{crystal}. \tag{83}$$

The plane of the detector is now introduced, rotating the norm of the plane $\mathbf{a}_{plane} = \mathbf{R}(\boldsymbol{\alpha})\hat{\mathbf{z}}$, and finding the intercept of the reflected beam

$$\lambda = \frac{\mathbf{a}_{plane} \cdot (\mathbf{x}_0 - \mathbf{x}_c)}{\mathbf{a}_{plane} \cdot \mathbf{m}} \tag{84}$$

$$\mathbf{x}_{plane} = \mathbf{x}_c + \lambda \mathbf{m}. \tag{85}$$

Finally transforming back to obtain the energy contour in camera coordinates

$$(x,\ y,\ 0) = \mathbf{R}^{\mathrm{T}}(\mathbf{x}_{plane} - \mathbf{x}_0) \tag{86}$$

Inverting the above problem is non-trivial, and highly non-linear as the square root appears in multiple places in the equation. An example dispersion for $\boldsymbol{\alpha} = (10°,\ 10°,\ 0°)^{\mathrm{T}}$ is shown in Fig. 2.11 around the single point in focus. Without imposing the single-value square-root, the problem becomes entirely non-invertible as multiple energy values project onto points of the camera plane. Any problems in aligning a von Hamos spectrometer are further compounded by use of mosaic crystals, which generate a cross-pattern when in focus due to finite grain size.

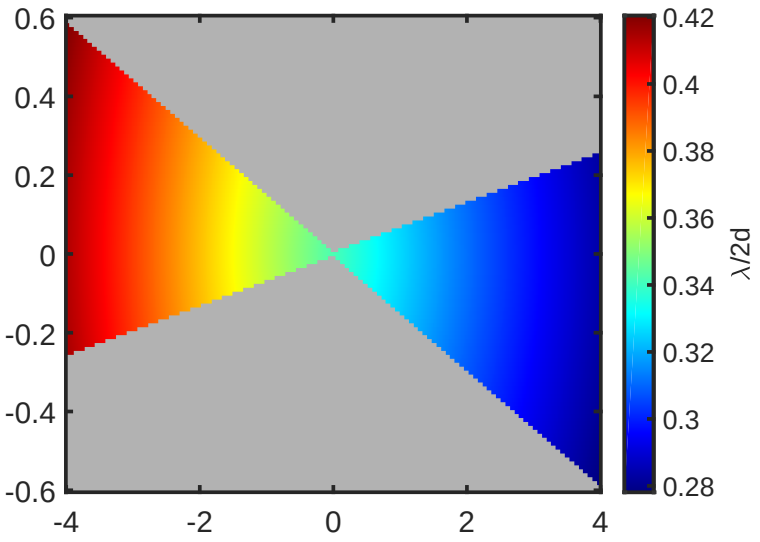

Figure 2.11: An example energy dispersion from a misaligned von Hamos spectrometer for $\boldsymbol{\alpha} = (10°,\ 10°,\ 0°)$, $\mathbf{x}_t = 0$, $R_0 = 5$, $\phi_{crystal} \epsilon [-30°,\ 30°]$ around the single focused point at $(0,\ 0)$, showing the complex dispersion generated by small misalignments.

The complex dispersion relations shown here, and for flat crystal spectrometers

in equation (52) demonstrate the importance of not only precise initial placement of diagnostics to achieve the desired spectral reconstruction, but also validation via calibration of the free parameters. In order to do so it is common to use calibrant characteristic x-ray emission lines that fall within the range of your spectrum, e.g. (K/L)(α/β), and while this is a useful starting point, it is not general solution to the problem. If the example from figure 2.3 is used, where spectral emission is reconstructed from a synthetically created image, it should be clear to see that within the bounds of a good initial guess by the 2 emission lines present within the spectral range, the calibration can be improved by considering not only the peaks of the emission, but the complete dependence of the continuum as well.

In order to construct a useful metric to optimize, consider that if the correct dispersion is obtained, $E(x, y, \boldsymbol{\theta})$, then the contributions of intensities of the spectral peaks will be maximised, and therefore the integral of the square of the spectrum will also be maximised,

$$J(\boldsymbol{\theta}) = \int dE\ \tilde{S}(E|\boldsymbol{\theta})^2, \tag{87}$$

however this is not quite true. As in constructing the spectrum it is also normalized to solid angle and dispersion, although photon numbers are conserved absolutely in the correct dispersion, the intensity on the image is not since it requires a transform for the detector amplification. In order to preserve the integrated image intensity while still performing the required normalization, the linear expansion of equation (53) on the contour $E(x, y, \boldsymbol{\theta} + \Delta\boldsymbol{\theta}) = E_0$ is found, assuming that E and

Ω are smooth functions in $\boldsymbol{\theta}$ over the range of the integral

$$\frac{\partial}{\partial \boldsymbol{\theta}'}\bigg|_{\boldsymbol{\theta}'=\boldsymbol{\theta}+\Delta\boldsymbol{\theta}} \left[\int_{E(x,y,\boldsymbol{\theta}')=E'} d\ell \; S\left(E\left(x,y,\boldsymbol{\theta}\right)\right) \frac{d^2\Omega}{dxdy} \left|\nabla_{x,y} E\left(x,y,\boldsymbol{\theta}\right)\right|\right] = \\ - \Delta\boldsymbol{\theta} \cdot \int_{\Gamma} d\ell \; \left(\frac{\partial E}{\partial \boldsymbol{\theta}} \frac{dS}{dE} \frac{d^2\Omega}{dxdy} \left|\nabla_{x,y} E\left(x,y,\boldsymbol{\theta}\right)\right| \right. \\ + S(E') \frac{\partial(\partial^2_{x,y}\Omega)}{\partial \boldsymbol{\theta}} \left|\nabla_{x,y} E\left(x,y,\boldsymbol{\theta}\right)\right| \\ \left. + \; S(E') \frac{d^2\Omega}{dxdy} \frac{\partial \left|\nabla_{x,y} E\right|}{\partial \boldsymbol{\theta}}\right). \quad (88)$$

As here the collected spectrum has not been normalized to the total integrated solid angle and dispersion, and assuming that the spectral gradients due to slight changes in the dispersion is a much greater effect than changes in the solid angle projection (valid so long as a detector would not be set up at large oblique incidence), or the change in the dispersion (valid for $\alpha_{x,y,z} \nsim \pi/2$) - a likely case due to the strong functional dependence of characteristic emission lines, then maximising $J(\boldsymbol{\theta})$ can be used to obtain the dispersion parameters. In order to formulate this as an optimisation problem, where as stated photon conservation is key, the image is subdivided into equal areas according to the input energy dispersion to create a spectrum on a non-linear energy scale that is unbiased when squared and summed.

In certain cases - such as parallel crystal and detector planes - the dispersion relation is not unique to an energy range given the crystal $2d$ spacing. This is also the case when there is a small degree of curvature in the emission lines across the range of the image, it is impossible to distinguish between conic sections as at distance all tend toward straight lines. It is possible to uniquely form a spectrum in this case, as a function of $D\sin\left(\bar{\theta}\right)$, however not a unique energy calibration.

In order to arrive at the set of energies across an image, the desired form of input to calibrate the spectrometer in this case is a simple list of energy values corresponding to emission lines, avoiding the need to specify where on the image these emission lines are present as this would lead to bias in the human (or algorithmic) input. When this is the case, a very good initial set of parameters is required, as the initial calibration must have the line energy fall within the width of it's emission. The optimisation parameter is then the integral $J(E)$, confined to energy values containing a fixed pixel area within the target energy value, maximising the emission line intensity rather than the extremizing the spectrum as a whole.

This method to calibrate spectral dispersion is hugely beneficial, as additional calibration shots are not fundamentally required in each new geometry, the method works at low signal levels where an emission peak cannot be accurately located in smaller parts of the image, and bias from pixel-based maxima have been removed. The principle of maximising the integrated sum of squares of the spectrum does extend to the ideal case of a von Hamos spectrometer, however the mosaic nature of the crystals used present a non-uniform reflectivity, and therefore a similar procedure cannot in general be used.

3 Temperature diagnosis of XFEL heated Ni

Applying the understanding of x-ray detection and spectroscopy to an emitting plasma has the potential to access information on the structure factor and atomic levels of a system as shown in equation (46). The detail of this atomic structure can be used to great effect in untangling the importance of particle correlations and quantum effects in governing ground- and excited-state plasma properties at high density, including collisional plasma dynamics [57, 34], transport properties [58, 59, 60], x-ray opacities [61, 62, 63] and the equation of state [64, 65]. Due to their large penetration depths, x-rays are often used to interrogate dense plasmas via spectroscopic techniques based on x-ray absorption, emission or (in)elastic scattering. For example, x-ray Thomson scattering (XRTS) [66] is widely used to diagnose warm-dense plasmas [37], to measure electron temperatures and densities [67, 68], ionization and degree of IPD [69], ion temperatures and plasma viscosity [70, 71]. Hotter plasmas, with higher atomic numbers and high degrees of partial ionization, are in turn better suited to be interrogated via x-ray emission [72, 73] or absorption spectroscopy [61, 74, 75].

In contrast, RIXS has long been used to study the energy and momentum dispersion relations of elementary excitations in condensed matter systems but not in HED physics research. Seminal works observed the electronic structure of the valence states in metals and semiconductors [76, 77, 78], and the technique has been developed over the years to measure increasingly low-energy excitations such as phonons [79], (bi-) magnons, and d-d excitations [80, 81], with correspondingly increasing demands on the x-ray sources and spectral resolution of measurements.

The limitation in scope of RIXS research to date can be traced to the set of requirements for a RIXS experiment: a spectrally bright, stable x-ray source with a tunable narrow bandwidth to match the resonance condition. Historically HED experiments have had limited access to x-ray sources with the required properties.

The advent of XFEL light sources, such as the LCLS at SLAC, has offered a new avenue to pursue this field, with x-ray sources of unparalleled brightness [14] in transform limited pulse lengths [82] able to give single shot or time resolved studies. These characteristics enable frontier science including discovering and probing new states of matter, following chemical reactions in real time, and imaging structural properties on the nanoscale. In the context of RIXS these fourth-generation light sources provide the capabilities to both create and probe extreme plasmas on ultra-short, inertially confined timescales, and probe transient dense plasmas for the first time.

RIXS measurements of HED systems opens a large parameter space that may not be otherwise accessible. This chapter will detail a study of RIXS on the Ni K-edge using the LCLS, where the extreme fluence of the x-ray source isochorically heats to temperatures of order 10 eV on femtosecond timescales. Measurements of the inelastic scattering over ranges of 100's of eV off-resonance are used to give single shot measurements of electronic structure, temperature and IPD. The full capability of fourth generation x-ray light sources is demonstrated in their potential to diagnose a wide array of plasma parameters with single-shot spectra, with the RIXS spectrum providing a unique wealth of information on the heated Ni system not simultaneously diagnosable using other techniques.

3.1 Modelling resonant inelastic x-ray scattering

As discussed at the beginning of chapter 2, observed scattering spectra can be modelled using the form of the differential cross section given by Kramers and Heisenberg [45]. The form of the scattering cross section as a result of the hamiltonian interaction shown in equation (46) is reproduced here:

$$\frac{d^2\sigma}{d\Omega_{\mathbf{k}_2} d\omega} = \frac{\omega}{\Omega}\left(\frac{e^2}{mc^2}\right)^2 \delta(E_f - E_i + \omega - \Omega)\times \left| \langle f|\rho_{\mathbf{k}_1-\mathbf{k}_2}|i\rangle\,(\boldsymbol{\eta}_1\cdot\boldsymbol{\eta}_2) + \frac{1}{m}\sum_n \left(\frac{\langle f|\mathbf{p}(\mathbf{k}_2)\cdot\boldsymbol{\eta}_2|n\rangle\langle n|\mathbf{p}(-\mathbf{k}_1)\cdot\boldsymbol{\eta}_1|i\rangle}{E_n - E_i - \Omega} + \frac{\langle f|\mathbf{p}(\mathbf{k}_1)\cdot\boldsymbol{\eta}_1|n\rangle\langle n|\mathbf{p}(-\mathbf{k}_2)\cdot\boldsymbol{\eta}_2|i\rangle}{E_n - E_i + \omega} \right) \right|^2, \quad (89)$$

and a schematic representation of the scattering channels is shown in figure 3.1. Recalling that $|i\rangle$, $|n\rangle$ and $|f\rangle$ are initial, intermediate, and final states of the system, with respective energies E_i, E_n and E_f. $\boldsymbol{\eta}_1$ and $\boldsymbol{\eta}_2$ are unit polarization vectors of incident and outgoing photons, with energies Ω and ω respectively.

When the incident photon energy is close to or above an electron excitation threshold, the second matrix term in equation (89) becomes dominant as the denominator vanishes. If the lifetime of the intermediate state is considered, the energy of the state is modified $E_n \to E_n + i\Gamma_{nf}$, and the divergence is removed. The essential part of the differential cross section then becomes

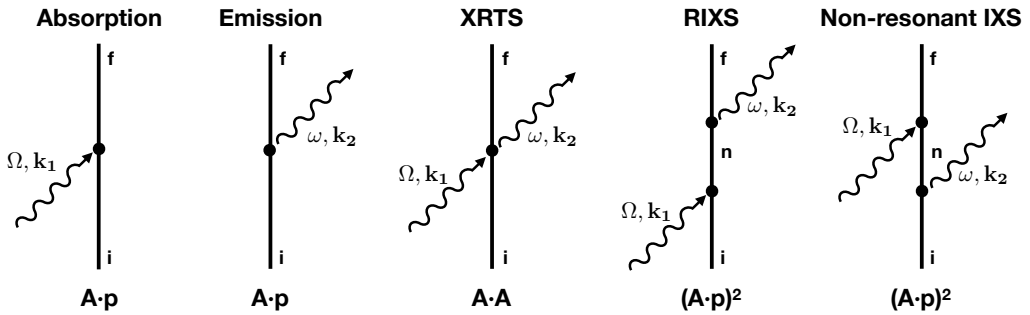

Figure 3.1: Schematic representation of x-ray-matter interactions to second order, and the scattering channels corresponding to the interaction terms in equation (89).

$$\partial_\omega \sigma = 4\pi \left(\frac{e}{mc}\right)^4 \frac{\omega}{\Omega} \sum_j \delta(E_f - E_i + \omega - \Omega) \times \left| \sum_n \frac{\langle f|\mathbf{p}(\mathbf{k}_2)\cdot\boldsymbol{\eta}_2|n\rangle\langle n|\mathbf{p}(-\mathbf{k}_1)\cdot\boldsymbol{\eta}_1|i\rangle}{E_n + i\Gamma_{nf} - E_i - \Omega} \right|^2 . \quad (90)$$

At this point a number of approximations and substitutions can be made:

$$|\langle f|\mathbf{p}(\mathbf{k}_2)\cdot\boldsymbol{\eta}_2|n\rangle|^2 = A_f \quad (91)$$

$$\Gamma_{nf} \to \Gamma_f \quad (92)$$

$$\sum_n \to \int_0^\infty dE_n \, \frac{\rho(E_n)}{1 + \exp\left(\frac{E_n - \mu(T)}{T}\right)} \quad (93)$$

$$\langle n|\mathbf{p}(-\mathbf{k}_1)\cdot\boldsymbol{\eta}_1|i\rangle = M_{in} = M(E_n) \quad (94)$$

$$E_f - E_i = \varepsilon_{\mathbf{k}} - \epsilon_{L,f} \quad (95)$$

$$E_n - E_i = \varepsilon_{\mathbf{k}} - \epsilon_K . \quad (96)$$

A schematic of the energy levels is shown in figure 3.2. The reasoning for each

of the approximations used, when applied to the particular case of a core hole pumped around the continuum edge, is as follows:

- The transition matrix of a K_α decay is largely independent of the intermediate state which has an additional electron in a low-lying continuum state, so the transition matrix element is only dependent on the final state, $|f\rangle$.
- The lifetime of the intermediate state is largely governed by the short-lived core hole, hence the rate can be taken as the core hole lifetime.
- Replacing a sum over all intermediate states with an integral over the accessible (via Pauli exclusion) DOS.
- The matrix element for the transition can be represented as a function of the energy of the final state.
- The difference in energy between initial and final states is the energy of the ionized electron, $\varepsilon_{\mathbf{k}}$, and the binding energy of the L-shell electron that has decayed to fill the core hole, $\epsilon_{L,f}$.
- Similarly for the intermediate state, the difference in energy is the energy of the ionized electron and the binding energy of the core hole.

Applying the substitutions to equation (90) to obtain

$$\partial_\omega \sigma = 4\pi \left(\frac{e}{mc}\right)^4 \frac{\omega}{\Omega} \sum_f A_f \int_0^\infty d\varepsilon_{\mathbf{k}} \frac{\rho(\varepsilon_{\mathbf{k}})\delta(\varepsilon_{\mathbf{k}} - \epsilon_{L,f} + \omega - \Omega)}{1 + \exp\left(\frac{\varepsilon_{\mathbf{k}} - \mu(T)}{T}\right)} \left| \frac{M(\varepsilon_{\mathbf{k}})}{\varepsilon_{\mathbf{k}} - \epsilon_K - \Omega + i\Gamma_f} \right|^2 . \quad (97)$$

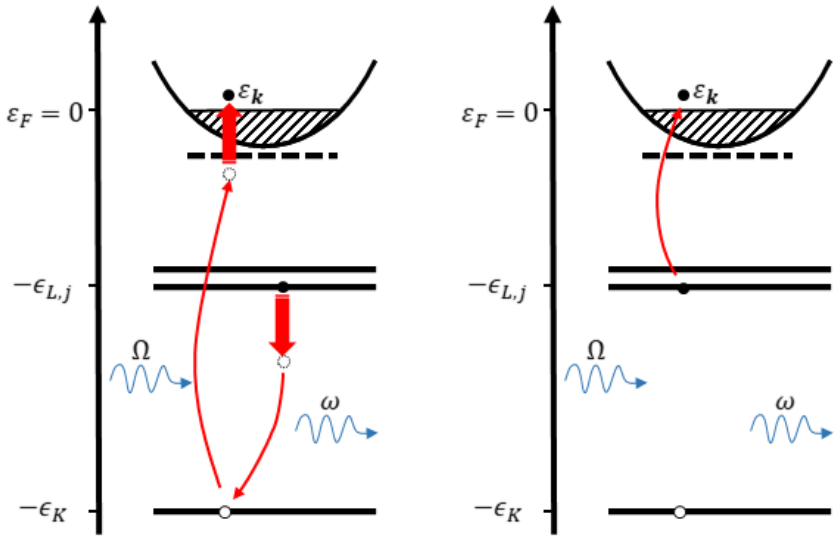

Figure 3.2: Schematic view of transitions in RIXS, where (a) an incident photon close to an absorption edge promotes a non-energy conserving intermediate virtual state, followed by an emission detuned by the same energy from the characteristic transition. (b) Schematic when considering only initial and final states in RIXS process, showing that when energy is conserved the photon energies will be correlated.

After evaluating the integral and squaring the denominator, a form of the differential cross section which is used for modelling the spectra is arrived at

$$\partial_\omega \sigma = 4\pi \left(\frac{e}{mc}\right)^4 \frac{\omega}{\Omega} \sum_f \left(\frac{A_f \rho(\Omega - \omega + \epsilon_{L,f})}{1 + \exp\left(\frac{\Omega - \omega + \epsilon_{L,f} - \mu(T)}{T}\right)} \frac{|M(\Omega - \omega + \epsilon_{L,f})|^2}{(\omega - (\epsilon_{L,f} - \epsilon_K))^2 + \Gamma_f^2} \right). \quad (98)$$

Here A_f represents relative line intensity (for K_{α_f}), Γ_f is the natural line width, and M is the dipole matrix elements. Using this understanding of the form of the RIXS spectrum as a projected DOS of available excitaions damped by a lorentzian lifetime, experimental observations can be understood and interpreted to give mea-

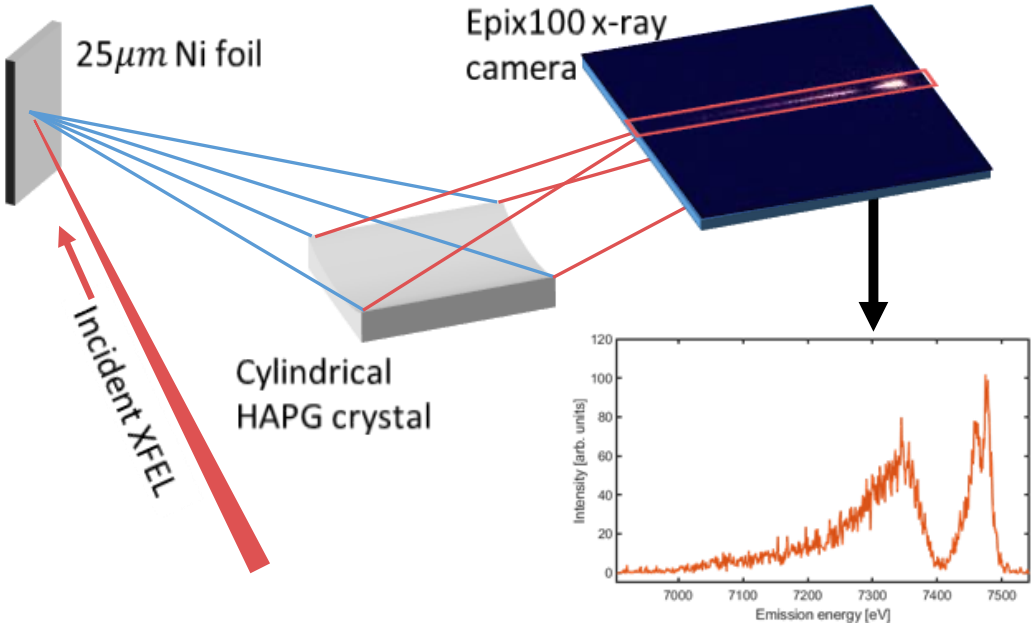

Figure 3.3: A schematic of the experiment, showing the energy dispersive HAPG crystal forming a spectrum on the ePix camera, focused into a line by the cylindrical geometry, along with a representative single shot spectrum.

sures of the conditions of the target.

3.2 Experiment

An experimental campaign to investigate RIXS in HED research was undertaken at the MEC endstation of LCLS [83] in April 2017. A 25 µm Ni foil target was illuminated by the XFEL in a range of focal spot sizes 1 µm to 40 µm FWHM, yielding intensities on target ranging between $2 \times 10^{16}\,\mathrm{W\,cm^{-2}}$ to $1.2 \times 10^{17}\,\mathrm{W\,cm^{-2}}$. The thickness of the target was chosen to be around one absorption length for irradiation below the Ni K-edge in order to maximize the total scattering signal while limiting the heating gradient in the beam direction. The central XFEL photon energy used was between 8080 eV to 8360 eV with a bandwidth of 0.3%. The

XFEL provided a photon flux in excess of 10^{12} photons per shot, over a duration of ∼60 fs. The third harmonic component of the beam was measured at 0.1%.

The spectrum was collected using a cylindrically curved Highly-Annealed Pyrolitic Graphite (HAPG) crystal coupled to an ePix100 x-ray camera in a von Hamos geometry. The resulting spectrum in the range 6.9 keV to 7.55 keV had a 9 eV spectral resolution [83, 54]. A schematic of the experiment is shown in figure 3.3, and a map of the emission spectra collected for the the highest intensities, where all features of interest are clearly visible and labelled, is shown in figure 3.4. The LCLS photon energy is tuned below and across the K-edge of Ni (at 8333 eV), illustrating a rich spectrum of down-scattered photons mapping out the valence electronic structure of the system. The relatively broad (2 eV FWHM [84]) Lorentzian tail of the K_α emission lines at 7460 eV and 7478 eV, combined with the high collection efficiency of the HAPG spectrometer is able to reconstruct scattered intensity over nearly 500 eV with a dynamic range of $\sim 10^5$, capturing features from across a wide band of bound (3s and 3p) and valence band (3d, 4s and 4p) states.

Above 8310 eV the bandwidth of the XFEL pulse contains the K-edge of Ni, the K-shell electrons can be directly photoionized, giving intense characteristic Kα radiation which quickly saturates the detector. All parts of the spectrum that contain saturated pixels on the detector were not considered in further analysis. Additional shots to recover the peak intensity of the K_α by attenuating the beam showed a dynamic range of 10^6, however attenuation limits the heating of the system and so does not produce comparable data. Here a range of incident intensities was sampled by moving the target away from best focus. Spectra collected via

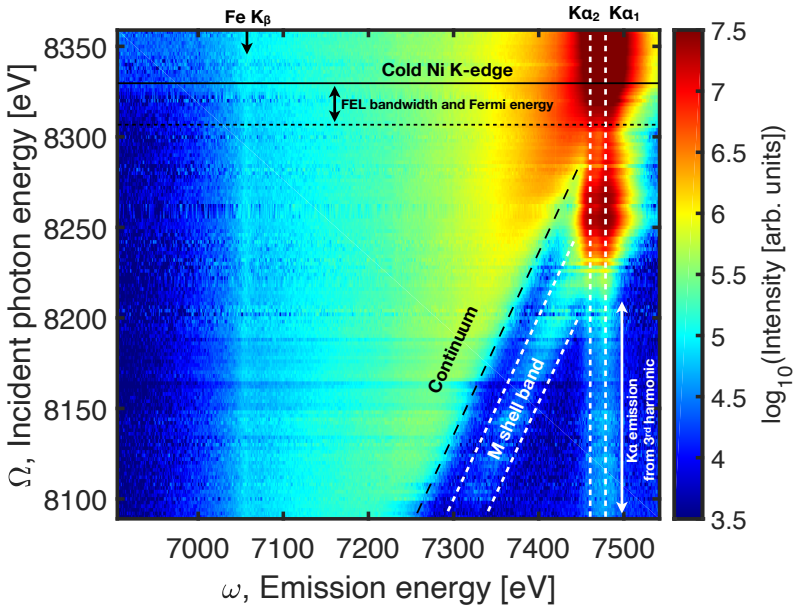

Figure 3.4: Experimental RIXS spectrum map of warm dense Ni. The $K_{\alpha_{1,2}}$ emission lines are driven by 3 distinct processes: below 8.2 keV core electrons are photoionized by the weak 3rd harmonic component of the XFEL; 8.2 keV to 8.3 keV the XFEL resonantly pumps the K-M transition; and above 8.3 keV the x-ray bandwidth is sufficient to begin directly photoionizing the core K-shell electrons into the continuum. The continuum and M-shell features are visible in the spectrum below the K_α emission, where the photons are inelastically down-shifted, as indicated on the figure. A contaminant gives an emission line at 7057 eV, corresponding to the Fe K_β.

moving target foil both up- and down-stream of best focus to result in the same incident intensity were found to be indistinguishable, and well characterised the best focus from the heating of the sample.

3.2.1 Spectral fitting

The form of the differential cross-section of RIXS is now applied to the particular case of a core hole pumped around the continuum edge. The attenuation length of

photon energies used below the K-edge is ~ 20 µm in Ni, and additional spectra were taken on 1 and 3 µm foils which were found to give similar spectral features within error once normalized to target thickness, so opacity effects were neglected in simulating the emission spectra. The final spectrum is described by integrating equation (98) over the incident photon energies,

$$I(\omega) = \Omega_{SA} \int_0^\infty d\Omega \; \Phi_0(\Omega) \partial_\omega \sigma, \tag{99}$$

where $\Phi_0(\Omega)$ is the incident beam energy profile, and Ω_{SA} is the solid angle subtended by the detector, which is also a function of scattered photon energy, ω.

Matrix elements used to construct the spectrum in equation (98) were produced using the DFT code ABINIT [85] and ATOMPAW [86]. Documented values were taken for electron binding energies, line ratios and line widths [87].

$$A_f = \{100, 51\} \tag{100}$$

$$\epsilon_K = 8333\,\text{eV} \tag{101}$$

$$\epsilon_{L,f} - \epsilon_K = \{7478.15, 7460.89\}\ \text{eV} \tag{102}$$

$$\Gamma_f = \{1.96, 1.94\}\ \text{eV}. \tag{103}$$

The incident photon energy profile was assumed to be a gaussian with 0.3% FWHM as a result of SASE amplification within the XFEL.

$$\Phi_0(\Omega) = \frac{N_\gamma}{\sigma_\Phi \sqrt{2\pi}} \times \exp\left(-\frac{1}{2}\left(\frac{\Omega - \Omega_0}{\sigma_\Phi}\right)^2\right) \tag{104}$$

$$\sigma_\Phi = \frac{0.003 \times \Omega_0}{2\sqrt{2\ln(2)}}. \tag{105}$$

The experimental spectra were averaged according to the central XFEL frequency in bins of 2 eV width and normalized to incident pulse energy, with a total of 11,383 XFEL shots included across the full intensity range from $2 \times 10^{16}\,\mathrm{W\,cm^{-2}}$ to $12 \times 10^{16}\,\mathrm{W\,cm^{-2}}$. The averaging results in between one and 63 shots per bin, populated by tuning the XFEL photon energy in 20 eV increments with a ± 10 eV stochastic spread. The final spectra are fitted to the data as a function of IPD energy shift and temperature, and show overall excellent agreement. The fitting results for a few specific photon energies are shown in figure 3.5. Temperatures are due to XFEL heating of the Ni foils to values of up to ~ 15 eV, which marginally ionizes the target, removing M-shell electrons, which have a binding energy of 67 eV.

The temperature values extracted are a good indication of the peak temperature in the target, as the ionization has a strong, almost exponential dependence on temperature while $T \ll E_{bind}$, so the peak ionization will dominate the emission. This is also found in optimising the fitting parameters, as it imposes strong constraints on the temperature. The IPD is also fitted, however multiple emission spectra from different parts of the target can overlap with similar weightings - and while the M-shell IPD can be extracted reliably, the L-M feature is not always visible, so when this is the case its position cannot be used, and the constraint on extracted values based on the continuum position is not as strong. This could be improved using a dedicated pump beam to generate uniform target conditions, rather than relying on the incident XFEL profile as both pump and probe.

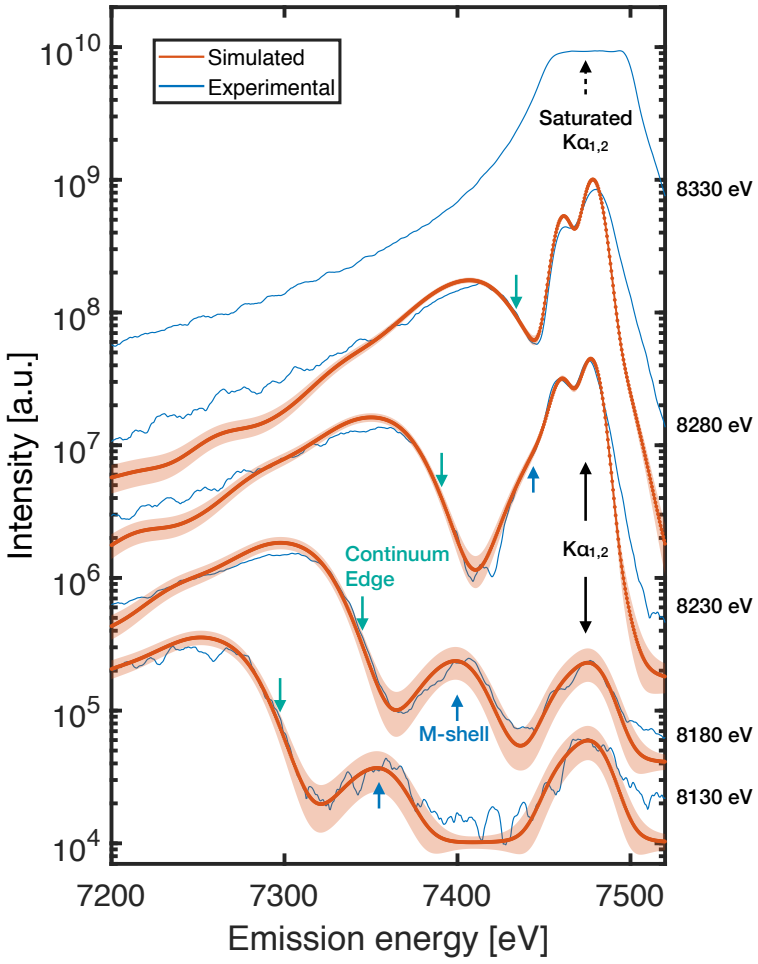

Figure 3.5: RIXS spectra and fit for five different XFEL energies, showing the key features of continuum, M-shell and K_α emission. For lower photon energies the K_α peaks are washed out as they are generated the unfocused 3rd harmonic component of the beam and are source broadened. At high photon energies, above edge photoionization causes the detector to become saturated.

3.2.2 Energy and intensity dependence

The map of RIXS spectra presented in figure 3.4 shows the full energy resolved dependence of the scattering cross section around the nickel K_α. Both the continuum DOS and the vacant M-shell states can be seen off-resonance when the incident XFEL energy is below the K-edge, with off-resonant emission damped by the lorentzian lineshape of the K_α. In the ground state this would typically yield the unoccupied DOS above the Fermi energy [76], however, in the results presented here the x-ray intensities are sufficiently high to heat the system, further ionizing it, and creating vacant states across the entire band. For temperatures around the Fermi temperature the population of vacant states follows the typical shape of the Fermi distribution. This dependence can then be used to extract valence electron temperatures and absolute measurements of the onset of the continuum with respect to the core electron binding energy. Comparing the observed binding energy to known values can be used to extract a measure of IPD in the system, as a function of the temperature (or corresponding ionization) and density (which is static over the duration of the pulse).

When the incident photon energy is below the Ni K-edge there is no direct K-shell photoionization and no characteristic K_α emission is seen apart from source-broadened (unfocused) third harmonic ionized Ni. Absorption occurs via the the 2-electron RIXS scattering cross-section, as well as absorption in L-shell electrons, which heats the target for the duration of the 2 mJ pulse. The two main features in the Ni ion where photons are observed to be inelastically downscattered are for L-shell excitations into the M-shell and the continuum band, as shown in

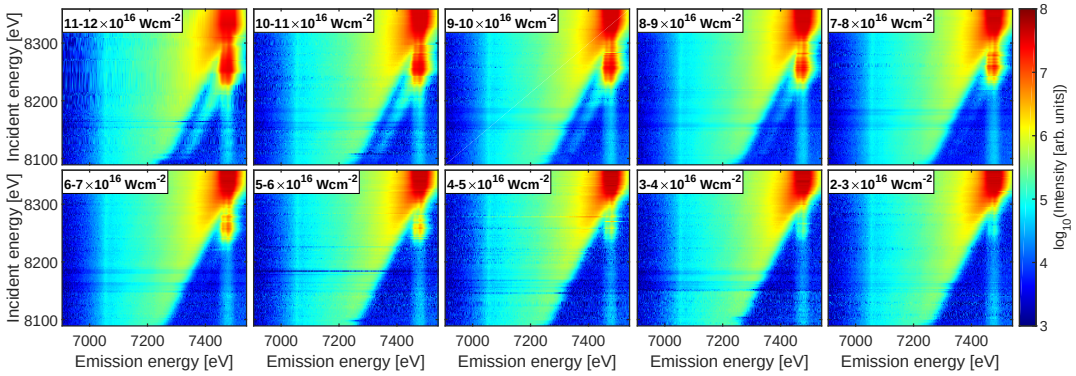

Figure 3.6: Experimental map of RIXS spectra of warm-dense Nickel collected for a range of incident XFEL intensities. The x-ray pulse drives isochoric heating of the target, with higher intensities creating correspondingly hotter, more ionized plasma conditions. The intensity of the M-shell feature is strongly dependent on the pump intensity, including when the XFEL resonantly pumps the K-M transition at 8250 eV.

the schematic of transitions in figure 3.2, and both features are marked in figure 3.4. Individual states within the M-shell cannot be resolved here because of the relatively broad 20 eV bandwidth of the x-ray pulse which broadens the inelastic spectrum.

For lower XFEL intensities the system is not ionized to such a large degree, with fewer vacant M-shell states, and therefore lower emission due to electron transitions into those states. This effect is shown in figure 3.6, where the same map as figure 3.4 is presented, but for a range of different incident intensities. By changing the intensity on target the degree of isochoric heating and inner-shell ionization can be tuned, resulting in different systems with corresponding different RIXS spectra. The main K_α emission features are present in all ten spectral maps, due to above edge photoexcitation. In contrast, the scattering signal from L-M excitation shows a strong dependence on XFEL intensity. At $<7 \times 10^{16}\,\mathrm{W\,cm^{-2}}$

there is very little observable L-M signal inelastically. The XFEL photon energy coincides with the K-M transition at $\sim 8250\,\mathrm{eV}$ and resonantly enhances the signal, seen as an enhanced K_α feature down to $3 \times 10^{16}\,\mathrm{W\,cm^{-2}}$ incident intensity.

3.3 Experimental results

Key plasma parameters are determined by fitting the identified form of the RIXS spectrum to the experimental data using weighted least squares. Temperatures of the XFEL heated plasma are determined in the range 6 eV to 15 eV, as shown in Fig. 3.7a, resulting in an average of up to 0.06 electrons removed from the 3p shell. Above 30 eV temperature the approximation used in the fitting of a constant DOS would break down as multiply ionized states become significant, causing more significant changes in the structure of the DOS and bound states, however these conditions were not reached in this experiment.

Heating in the target changes little with photon energy, as seen in figure 3.7a, and temperatures can be determined to within 1 eV accuracy from the scatter of the data. This limitation is purely an aspect of the experimental design - utilising a narrower bandwidth source or higher resolution spectrometer could yield substantially more accurate measurement directly from the slope of the Fermi function, although these requirements may also come with a drop in pulse energy or collection efficiency. Increasing intensity of the incident x-rays has a large effect on the temperature achieved in the system, consistent with larger energy deposition and higher final energy. While here the XFEL was used as a pump and probe for the sample, the constant temperature for each intensity shows that in this case RIXS did not contribute significantly to the heating and rather L-

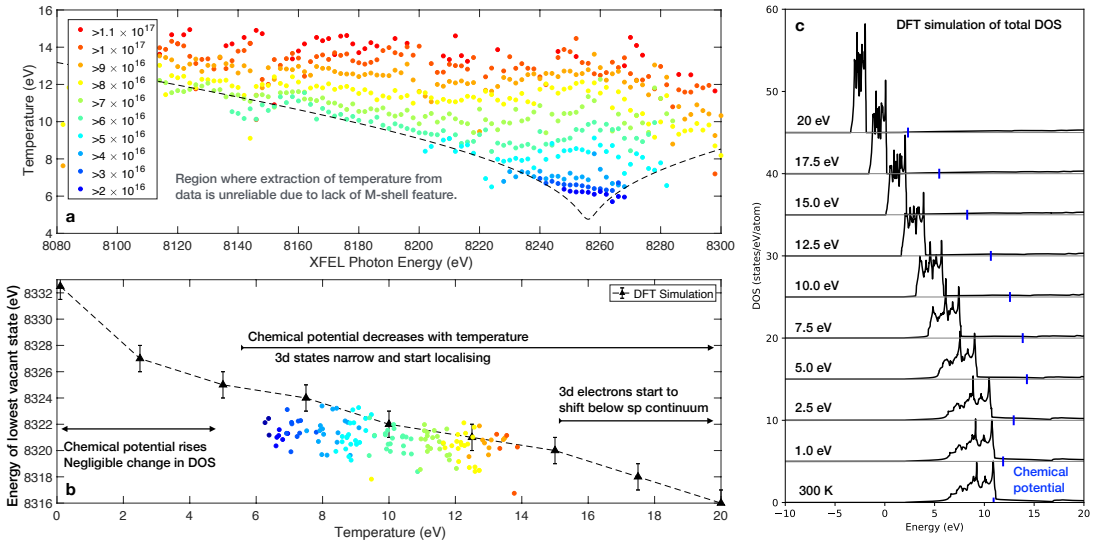

Figure 3.7: (a) Temperature and (b) IPD values as a result of fitting the RIXS data for all incident intensities with the spectral model as described. (c) Calculations of the DOS indicate good agreement with the observed continuum edge positions as a function of temperature. The resonant dependece of rixs emission on photon energy limits the range of temperatures that can be measured in this case, as indicated in (a).

shell absorption was the dominant heating mechanism - also demonstrated by the linear dependence of temperature on incident intensity. The strong non-linear dependence of the RIXS signal on incident intensity leaves the possibility that this could be used as a method for creation of well defined conditions using the XFEL by tuning the photon energy, and therefore the relative contribution of the second order heating process.

In this example of collected RIXS spectra the temperature is mainly bound by the intensity of the M-shell band rather than the slope of the Fermi function. In order to observe the shape of the Fermi function, as well as features in the DOS, spectrometer resolution would need to be improved from this proof-of-principle

experiment, which has the potential to allow temperatures of transient systems to be measured down to eV-level - beyond which the scattered number of photons within k_BT of the chemical potential is likely to be insufficient to place reasonable error bounds. Accurate temperature measurements and error bounds on transient WDM systems at the eV-level has been a longstanding goal, and RIXS has the potential to further constrain the parameter space, including those which can reproduce XRTS observations [88]. In regions where the M-shell is no longer visible above noise in the spectrum, due to detuning or lack of ionization creating vacant states to transition into, temperature can no longer be accurately bound. This region is shown with a dashed line on figure 3.7a, below which fits to the data are unreliable. Fitted values of temperature and the corresponding fitted IPD are plotted in figure 3.7b, where the range of measured values can be seen to be consistent with DFT calculations of the onset of the continuum band in heated Ni.

Figure 3.7c presents the DFT structure of the DOS of Nickel around the Fermi edge. The continuum edge decreases in energy as expected on heating, and corresponds well with the measurements of IPD. The chemical potential is seen to increase upon initial heating, due to the weight of the 3d states, hybridized at the base of the continuum. The 3d electrons are depopulated on heating, requiring the chemical potential to rise in order to maintain the electron population. If an experiment to measure lower temperatures using the slope of the Fermi function was fielded, this rise could play a complicating role, as there is additional structure in the DOS and matrix elements which is included the functional dependence of the emission.

The use of RIXS to measure IPD relies on accurately diagnosing the emission energies of key spectral features. As the IPD shifted continuum will be seen to emit at all temperatures, the position of the M-shell is the key indicator of IPD. As the M-shell peak's location is not always accurately discernable within spectral noise, especially at lower intensities, there is a large error on IPD measurements. The correlation between fitted temperature and IPD is as expected by all models, and if spectra can be measured with increased resolution, and decreased bandwidth, a more accurate measure of IPD at these marginal ionizations could be found to attempt to distinguish them.

3.4 Discussion

The ability to measure temperatures on the order of a few eV is an often sought after goal of WDM studies, as an accurate diagnosis of the conditions in these transient systems is challenging. The temperature measurements made here establish good bounds of $\pm 0.5\,\mathrm{eV}$ up to $15\,\mathrm{eV}$. The range over which these measurements are useful is limited here due to the particular binding energy of the Ni 3p electrons, $67\,\mathrm{eV}$ below the fermi energy. The limitation of the M-shell feature being visible above spectral noise could be remedied by using another element so long as the experimental platform supports this. Above $30\,\mathrm{eV}$ temperatures multiply ionized states begin to dominate - however this too can be remedied by using either a different element, a different transition, or extending the model to consider multiply ionized atoms.

The RIXS spectrum corresponding to an inner shell excitation contains the same information on the unoccupied DOS as an x-ray absorption spectroscopy

experiment [89]. RIXS also offers several additional advantages in terms of symmetry projection selectivity, access to higher multipole excitations and the absence of lifetime broadening on observed features [90]. For a system with short-lived core holes, as is the case for typical high-Z ions, very broad absorption spectra can be collected, where the bandwidth of the source only acts to limit the resolution of the absorption features that can be observed rather than limiting the spectral range. The results show that the peak spectral brightness of an XFEL is sufficiently large to yield single-shot RIXS measurements of the vacant DOS. Self-seeding of the XFEL is a promising route forward in these studies to limit XFEL bandwidth to $\sim 10^{-4}$, however the stochastic amplification in the undulator causes large variation ($\pm$100% RMS) in the pulse energy as the monochromator may not align with one of the peaks of the SASE spectrum, and would require additional shot selection, which may limit its use as a diagnostic capability.

While RIXS has been observed over similar energy ranges in early studies [76], the potential of this technique using the extreme intensities of tuneable XFEL sources to observe transitions 100's of eV off resonance while maintaining resolution requirements allows it to be applied in new areas. The ability to measure extremely low levels of partial ionization has a myriad of potential applications in time-resolved charge transfer studies to determine the active component of enzymes, such as Fe^{2+} activation, extending existing synchrotron work on charge transfer [91]. Using nanometre thin-foils or nanostructured targets to achieve uniform plasma parameters on optical heating would allow similar measurements to be extended to higher energy densities. This technique could also be used as a temperature diagnostic of ramp-compressed shocks, where the plasma conditions

are no longer confined to the Hugoniot curve, of interest in shocked HED studies where temperature measurements of these transient systems is difficult.

3.5 Conclusions

The application of RIXS in this case can be viewed as an effective pump-probe experiment, where the absorption is the pump and the emission is the probe, with the core-hole lifetime as an effective clock. In the measurements of incident intensity and photon energy dependent temperature and IPD a new method to access these key plasma parameters has been established. Temperatures measured from the XFEL-heated solid-density Ni plasma were well-bounded between 6 eV to 15 eV, giving M-shell ionizations of up to 6%, with the range of valid measurements determined by the XFEL photon energy and the binding energy of the 3p electrons in Nickel. Simultaneous diagnosis of IPD and $\mathcal{O}$(eV) transient WDM conditions to this accuracy is, to the authors knowledge, unprecedented. Measured values of IPD are shown to correspond well with DFT calculations of the density of states in the observed temperature range. With an expanded dataset it may become possible to use RIXS to fully characterise and explore IPD depedence up to higher charge states. This approach shows promise to enhance experimental capabilities in probing extreme states of matter, of broad relevance to planetary science and ICF research.

The unprecedented brightness and tunability of XFEL sources extends the potential range of studies using RIXS, as here it has been demonstrated that key plasma parameters can be extracted on a single-shot basis. Utilising this technique offers unique opportunities for investigating time-resolved electronic state

dynamics, understanding and following chemical reactions and energy conversion processes in real time, and imaging chemical and structural properties of materials on the nanoscale. This has potential applications in a myriad of studies, including measurements of charge transfer in alloys and biological systems, and off-hugoniot plasma parameter determination in ramp-compression studies. Time resolved measurements of IPD could also be taken using the two-colour mode at LCLS or EuXFEL, allowing sufficient time to fully thermalize between pulses to determine the range of validity of the Ecker-Kröll vs. Stewart-Pyatt models, where the timescale of heating vs. equilibration is a key differentiating factor [92].

4 Nanostructured targets irradiated at petawatt intensities

As laser systems have increased in power the conditions achievable in driving targets to HED using them has broadened, as well as the requirements on diagnostic capabilities. X-ray radiography remains a key diagnostic in visualising target geometries, but there is a drive toward more intense, and better characterised x-ray emission sources to increase the reliability and shot-to-shot performance of these measurements. Nanowire array targets were proposed as a route forward, as their geometry allows increased laser absorption [39, 93], as well as volumetric heating of the target, minimising the strong plasma parameter gradients seen in flat targets due to the short attenuation length scale [94, 95].

Nanowire array targets have demonstrated huge increases in x-ray emission intensity, as the improved energy coupling allowed targets to be driven to extreme ionizations, with energy densities of $2\,\mathrm{GJ\,cm^{-3}}$, comparable to the conditions achievable in ICF implosions. Scaling the performance of these targets further for use as x-ray backlighters has been an ongoing effort, as the plasma dynamics at extreme intensities ($>10^{18}\,\mathrm{W\,cm^{-2}}$) using ultrafast, short-pulse laser systems ($<100\,\mathrm{fs}$) is almost universally characterized by low optical absorption. On these short timescales the large number of liberated electrons in a laser target form a metal-like system, with step-like changes in the index of refraction leading to a large Fresnel reflectivity, and reduced coupling of the laser energy to the target. Nanostructured targets modify the dielectric tensor on the scale of the optical laser wavelength to reduce the reflectivity and produce a greater quantity of x-ray

emission, however they are difficult to model for the spatial scales and timescales needed to observe the full hydrodynamic evolution of the nanostructure within the laser focal spot. Example Scanning Electron Microscope (SEM) images on nanowire targets are shown in figure 4.1.

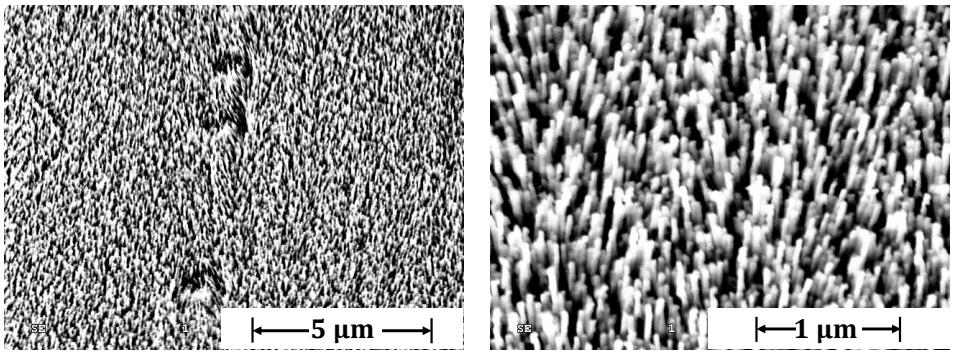

Figure 4.1: Scanning Electron Microscope images of an aligned nanowire array laser target. If the aspect ratio of the wires is too extreme, then wires can magnetically clump together.

Utilising the Orion laser at AWE, an experiment to drive Ni nanowire targets at relativistic intensities was performed by the Materials Modelling Group in August 2016. The x-ray emission of the Ni K_α, He_α, and Ly_α lines were collected on an ultrafast XRSS (as described in section 2.4), giving observations of the shifting ionization stages and conditions present in the target over the full duration of emission. Using this time-resolved emission, it is possible to fit the range of plasma conditions present in the target, in order to compare with, and benchmark simulated laser-target interaction. All subsequent analysis of spectral data was performed by the author, and is included in two manuscripts submitted for publication [38, 96].

4.1 Nanowire optical absorption

Before extending the description of nanowire interaction to the relativistic intensities at the Orion laser, a description of their absorption at mid-intensities is useful to contextualize the investigation of nanowire response. The physical interaction of laser radiation incident on nanowire targets can be described for intensities $10^{14}\,\mathrm{W\,cm^{-2}}$ to $10^{17}\,\mathrm{W\,cm^{-2}}$ as an effective anisotropic dielectric: a normal bulk metal supports currents at the interface, and internal material fields, which are driven by the incident electromagnetic wave; these re-radiate to give the specularly reflected field. The same currents and material fields also radiate forward-going fields which destructively interfere with the forward-going incident field to produce attenuation on the scale of the skin depth. In a nanowire target, the anisotropic material does not support the same response, so the reflected field is weaker and the net forward-propagating field stronger, as it cannot support the same Fresnel reflection as bulk metal. The material response to p-polarized light is largely along the length of the wires, thus the radiation pattern of each wire is similar to a linear antenna, sending very little radiation in direction of the target normal – either specularly or forward-going – and therefore light is transmitted well through the surface and into the highly absorbing solid density metal wires.

The effects of the anisotropic dielectric at medium intensities is well described by Marjoribanks *et. al* [39], where the dielectric tensor is spatially averaged at the meso-scale, interacting with nanowires with a fill fraction, f, to find the refractive index and skin depth. The polarizability of a cylinder, given that its diameter is

$\ll \lambda$, is taken as that of a needle as in Venermo [97]:

$$\chi = \frac{\epsilon_B - 1}{1 + L(\epsilon_B - 1)}, \tag{106}$$

where ϵ_B is the relative permittivity of the bulk, and L is the depolarization factor, taking the value $L_\perp = 1/2$ and $L_\parallel = 0$, as the relation $\sum_i L_i = 1$ can be used with rotational symmetries of the system. Spatial averaging of the system can be constructed over a series of artificial cylinders containing an increasing number of uniformly distributed nanowires as in Kulcsár [98]. Averaging over the fill fraction the macroscopic dielectric tensor is found

$$\epsilon_\parallel = 1 + f(\epsilon_B - 1) \tag{107}$$

$$\epsilon_\perp = 1 + \frac{2f\frac{\epsilon_B - 1}{\epsilon_B + 1}}{1 - f\frac{\epsilon_B - 1}{\epsilon_B + 1}}, \tag{108}$$

which is correct for the limiting cases $f \to 0$, $\epsilon_{\perp/\parallel} = 1$ and $f \to 1$, $\epsilon_{\perp/\parallel} = \epsilon_B$. For values of $\epsilon_B = -17.5 + 29i$ at $\lambda = 1\,\mu\text{m}$ [99] for nickel nanowires, identifying the extinction index from $\epsilon = (n + i\kappa)^2$, plotted in Fig. 4.2 as a function of fill fraction.

While direct absorption is low for perpendicular applied fields, coupling to the target is increased due to the low refractive index, and propagates to a much greater depth in the target. The low reflectivity at the vacuum interface allows greater energy coupling to the target over flat foils. A full exploration of the absorption of nanowire targets as a function of nanowire length, fill fraction and polarization is found in Marjoribanks *et. al* [39].

As the length of the nanowires is reduced, light will reflect from the substrate

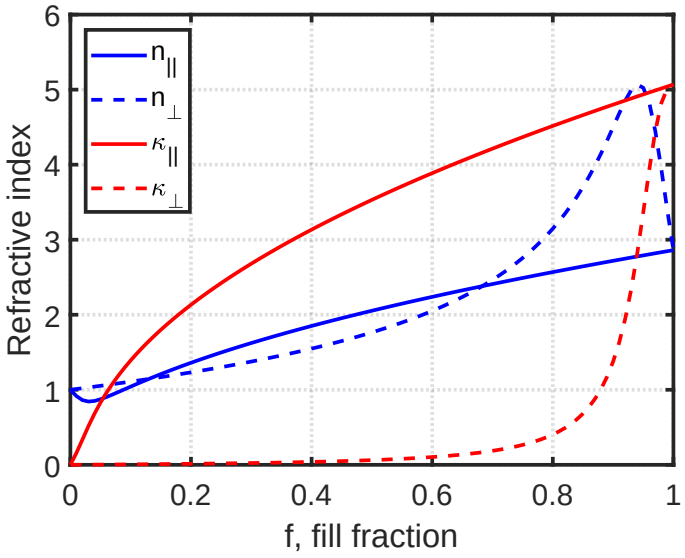

Figure 4.2: Real and imaginary components of refractive index of a Ni nanowire material, for parallel and perpendicular applied electric fields ($\lambda = 1\,\mu m$), as a function of fill factor. Reproduced from Marjoribanks *et. al* [39]

that the nanowires are electrochemically deposited on, and thin layer interference will create more complex structures in the absorption patterns. The absorption of nanowire targets has been seen to saturate at a thickness of $\sim 4\,\mu m$ [94], so for sufficiently long nanowires this is a small effect. Treating nanowires as an effective dielectric works well for mid-range intensities, and illustrates the key features of increased absorption, however higher intensity radiation begins to alter the nanostructure.

4.1.1 High intensity absorption

The extremely low reflectivity of nanowire targets due to limited material fields makes them a prime suspect for making more efficient use of intense ultrafast laser pulses to create HED systems. At high intensities, $10^{17}\,W\,cm^{-2}$ to $10^{19}\,W\,cm^{-2}$,

nanowires with a diameter $\ll \lambda$ will be rapidly and uniformly heated due to the large skin depth by laser-driven electrons released by ionization of the target material. The nanostructured target can be expected to rapidly disassemble and homogenize, governed by the speed of rarefaction in the nanowires. The speed of the rarefaction wave will be governed by the ion-acoustic speed of the heated plasma, resulting in a characteristic void closure time of 1 ps down to roughly 100 fs.

After void closure of the wires has occurred, the advantages of the anisotropic dielectric limiting material fields available in nanowire targets to support Fresnel reflectivity are removed, and a plasma mirror is formed at the critical density, n_c, limiting any further coupling of laser energy to the target to the same avenues as flat foil targets of inverse bremstrahlung and resonance absorption.

To see the effects of void closure on absorption at high intensities, an experiment was performed at LULI where Ni nanowire targets were driven with the ELFIE short pulse laser ($\lambda = 1.057\,\mu$m, $\sim$8 J, 350 fs, focal spot FWHM $\sim 10\,\mu$m), with approximately 1% converted into a frequency doubled probe beam which could have its arrival time adjusted relative to the main pulse. A schematic of the setup is shown in figure 4.3, where the reflectometry screen can be seen positioned at the angle of the specular reflection of the drive laser. The 2ω component of the light incident on the reflectometry screen was then captured, to see the differences in reflectivity of the target depending on the time of arrival of the probe beam. The setup was designed to allow the timing of the probe to be scanned through zero delay by reflecting from the back surface of paired glass wedges, so the group delay in the glass could overcompensate for the shorter path length, as well as reject the

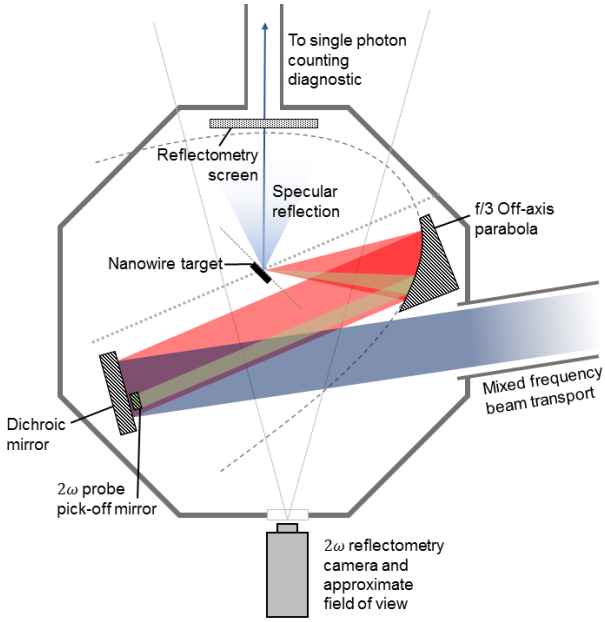

Figure 4.3: A schematic layout of the experiment at ELFIE to investigate the effects of prepulse and void closure on absorption of nanowire targets at high intensities, showing the relative positions of the drive and reflectometry screen to the target. An example SPC image and spectrum is shown in figure 2.6.

reflections of the fundamental.

A series of reflectometry images from Ni nanowires illuminated as in figure 4.3 are shown in figure 4.4, scanning the time of arrival of the probe from ∼30 ps prior to the main drive to ∼16 ps post pump-pulse, corresponding to a scanning in position of the pick-off mirror of ∼7 mm. The change in probe timing has large effects on the reflectivity of the target, understood to be as a result of:

a) Before the main pulse, where a dappled reflection of the 2ω probe from the target substrate can be seen along with $\mathbf{J} \times \mathbf{B}$ effects frequency doubling the reflection of the pump-pulse from damaged nanowires

b) Coincident, where almost all light is absorbed as both beams interact with

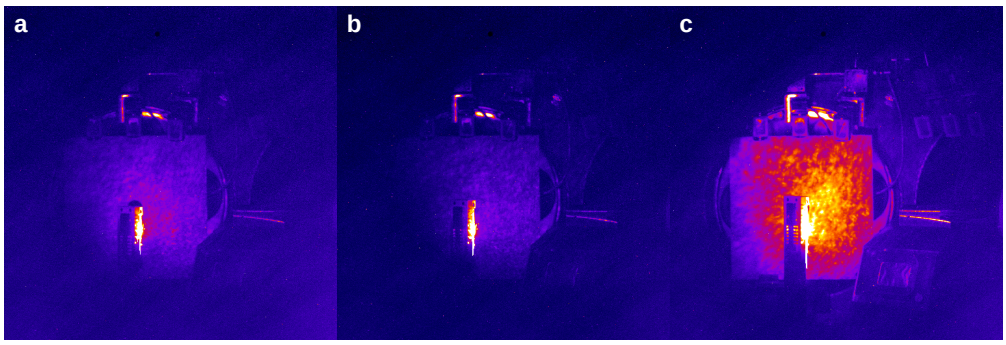

Figure 4.4: False colour reflectometry images of 2ω radiation around the specular reflection angle from Ni nanowire targets, for a 2ω probe pulse timed to be (a) $\sim$ 30 ps prior to, (b) coincident with and (c) $\sim$ 16 ps post pump pulse. The pump pulse was the ELFIE short pulse drive, with $\sim$ 1% converted to a frequency doubled probe.

undamaged nanowire targets

c) After the main pulse, a plasma mirror has formed and there is a bright specular reflection of the probe beam.

Although the timings of the pre- and post-pulse used at ELFIE are far above the expected dynamic timescale of void closure, the dramatic change in behaviour of the nanowire target is evident, and the conditions under which the performance of these targets can be scaled to higher intensities was further investigated at the Orion laser at AWE.

4.2 Experimental details

An experimental campaign investigating the potential to scale nanowire targets to kilojoule-scale laser facilities was undertaken using the high-contrast Orion petawatt laser at AWE, UK [100]. Full details of the experimental setup are

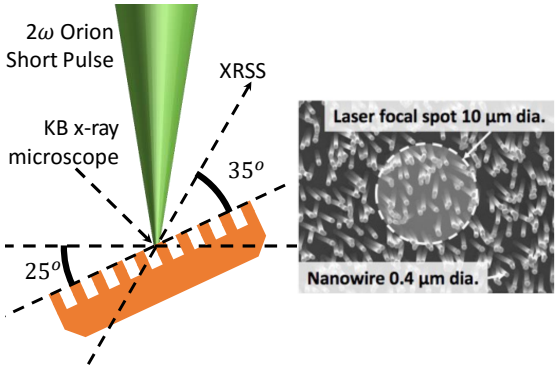

Figure 4.5: Schematic of experimental geometry, showing incident Orion short pulse on Ni nanowire array, and the primary diagnostic, the ultrafast X-ray Streaked Spectrometer. Inset: SEM image of nanowire array target.

provided in ref. [38], with key details for understanding the subsequent spectral analysis performed by the author reproduced here. A schematic of the experimental setup is reproduced in Fig. 4.5.

Arrays of Ni nanowires were shot with the frequency-doubled Nd:glass short-pulse laser (100 J, 600 fs, 10 µm FWHM focal spot), at intensities of $\sim 10^{20}$ W cm^{-2}, normalized vector potential $a_0 \approx 6$. The nanowires had $\sim 15\%$ fill fraction, and were 12.5 µm in length, with diameters of 400 or 1000 nm. The laser was incident at 25° from normal with the ultrafast XRSS observing the front of the target 55° off-normal.

The emission collected on the XRSS has a time resolution of ~ 1 ps, and an energy resolution $E/\Delta E \sim 500$ for the energy range observed (7.4 keV to 8.4 keV). The energy range collected captures emission of the cold K_α, as well as the He_α and Ly_α from high ionization states, including the associated satellite peaks as seen in Fig. 4.7a. By observing the time-resolved satellite emission and comparing to a collisional radiative code such as FLYCHK [101], it is possible to infer the

evolving ionization balance and associated temperature and density of the plasma.

The nanowires, similar to previous high intensity studies, exhibit brighter and prolonged emission compared to a flat foil target [38, 93, 95]. The increase in intensity comes primarily from the high-lying charge states, with a 2× increase in He-like emission brightness, yielding a 3× increase in the time-integrated emission across the full energy range. An example image of raw data collected is shown in Fig. 4.6, where the both the intensity and duration of the nanowire emission can be seen to be enhanced over that of a flat foil target.

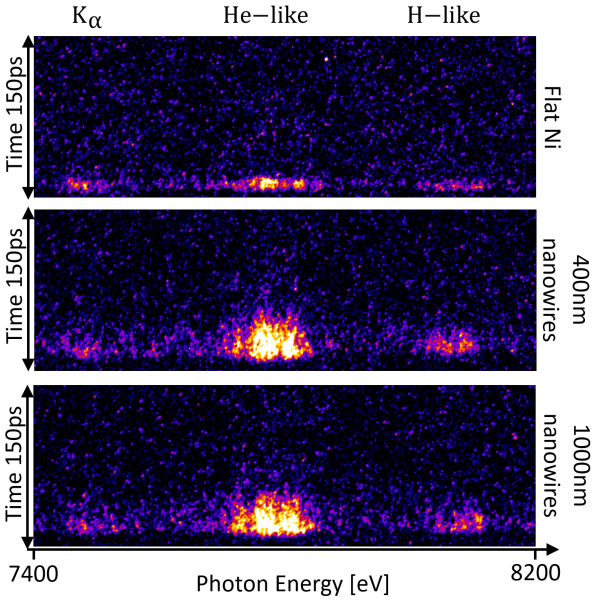

Figure 4.6: Raw emission data from X-ray Streaked Spectrometer, showing the duration and relative intensity of nanowire emission to flat foil, including the primary emission complexes of highly ionized Ni. Note that the high peak brightness of He_α in the nanowire emission leads to intensity broadening during the electron TOF as described in section 2.4, with emission appearing to begin before the laser pulse has arrived.

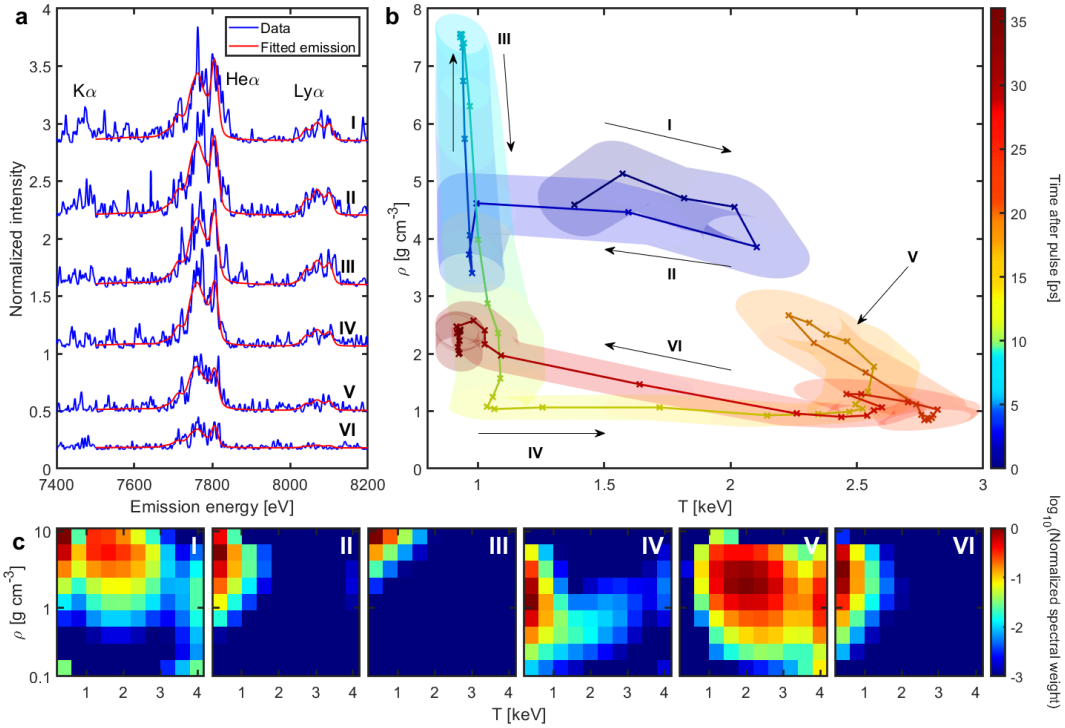

Figure 4.7: (a) Spectral emission data and fits from 400 nm Ni nanowire target showing the key K-shell emission features, with emission from distinct phases of evolution indexed I-VI. (b) Track of the centroid of the fitted emitting plasma distribution on T-ρ showing the evolution of the system in time (as colour). Half of the standard deviation of the distribution is plotted as an ellipse for each time step, which are then connected along the time evolution with their common tangents to represent the uncertainty in the dynamical path. (c) Normalized fitted distributions at the times indexed I-VI, with details provided in section 4.4 of the main text.

4.3 Fitting

In order to identify the conditions present within the plasma, the FLYCHK collisional radiative code [101] was used to produce spectra over a wide range of temperature and density conditions that would be present in the plasma. The FLYCHK code uses a screened hydrogenic model with relativistic corrections, which when simulating a Ni plasma includes all detailed term levels for Li-like satellite

states up to $n = 4$ from the HULLAC database. Spectra resulting from H-, He- and Li-like ions have good line positions as a result of the detailed level structure which is beneficial for this study of high-lying charge states. As expected, a single temperature-density condition was insufficient to model the emission due to the range of conditions present in the target, so a combination of steady-state emission profiles had to be used.

As the hydrodynamic timescales of the plasma are long ($\sim$ ps) compared to the transition rates of highly charged ion stages, and conditions are fitted for much longer than the laser pulse is directly perturbing populations, the system can be modelled as a combination of these steady-state profiles, depending only on the set of local temperature and density conditions in the plasma. Some interaction physics will be missed with the assumption of steady state, however in order to run in time-dependent mode knowledge of the evolution of the hot electron population and the spatially resolved temperatures and density from hydrodynamic simulations would be required as an input for the zero-dimensional FLYCHK code, and using a summation of steady states includes fewer built-in assumptions about the plasma.

A grid of 10 temperatures, 0-4 keV, and 10 densities, exponentially sampled between 0.1-10 g cm^{-3}, was used to produce simulated emission spectra. The limits on the T-ρ grid were chosen to correspond to the estimated conditions of the plasma based on particle-in-cell and radiation-hydrodynamic simulations [38], while still having observable emission in the energy range collected by the spectrometer. The functional form of the spectrum is reliably reconstructed by a linear combination of these steady state emission profiles over the duration of the emission, as seen in

Fig. 4.7a.

In the interest of avoiding over-parameterising the dataset, a subset of weighting points within this $10x10$ sample grid was chosen as the set of fitting parameters, with the remaining spectral weightings being interpolated between them as seen in figure 4.8. This interpolation scheme allows a reduced number of free parameters to converge on a well conditioned fit to the data over the full temperature-density parameter space, and can be seen as fitting a generalised functional form to the T-ρ profile of the plasma with a resolution determined by the number of fitted points. Weightings were log-interpolated for density, due to the expected properties of the ablating plasma, and the exponentially sampled density grid. The fitted spectral weightings were found by minimizing a weighted least squares cost function, with weightings taken from the combined absolute and relative noise on the level of retrieved signal from the XRSS.

In order to remain sensitive to all spectral emission distributions, the points chosen as the subset of fitting parameters was sampled over all possible subsets. The resulting ensemble fit to the data, with examples shown in Fig. 4.8, was then averaged for each time step in the emission, with uncertainty due to the sampling and interpolation estimated by taking the deviation of the fitted spectral weightings. In order to fit the data, five points were taken in both temperature and density, retaining end points to construct a valid interpolant. A selection of fitted emitting plasma distributions for 400 nm diameter nanowires is shown in Fig. 4.7c, showing key points in the evolution of the plasma. An example distribution for a flat foil target is shown in Fig. 4.9a, 7 ps after drive.

At late times the collected emission can be seen to exhibit sharp features not

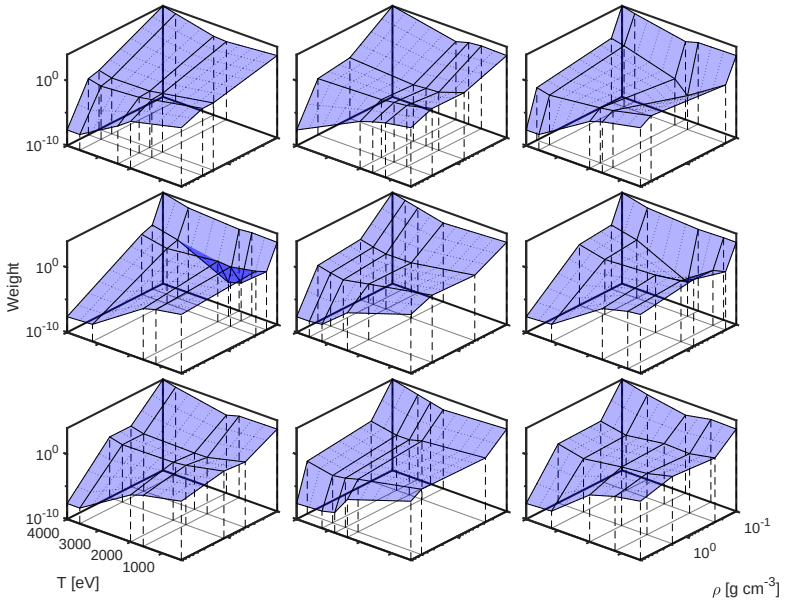

Figure 4.8: An selection of results comprising an ensemble fit to the spectral data, where all possible subsets of the parameter space with a fixed number of points are used to fit to the data, with remaining spectral weightings in T-ρ space being interpolated from the fitting parameters. The surface represents the plasma distribution, which is defined by the fitting parameters, at the intersections of solid lines along the surface. The resulting ensemble can be averaged to yield a well-conditioned fit, sensitive over the whole range of the T-ρ space of interest.

captured by the fitted spectrum as in Fig. 4.9b - this is most likely as a result of low signal levels giving large, Poisson-like noise on the detector below the energy resolution of the XRSS, which can be seen across the full spectral range. Another possible source of the discrepancy is due to the form of the fit yielding a parameter-number limited resolution of the T-ρ profile. At this late time it is possible that the emitting plasma would be better modelled by a narrower distribution than the model supports – or similarly, for a narrower range of conditions than is captured on the 10x10 sample grid – however, the form of the distribution in Fig. 4.9a does not support this. A final possibility is that the emission is due to significant high-

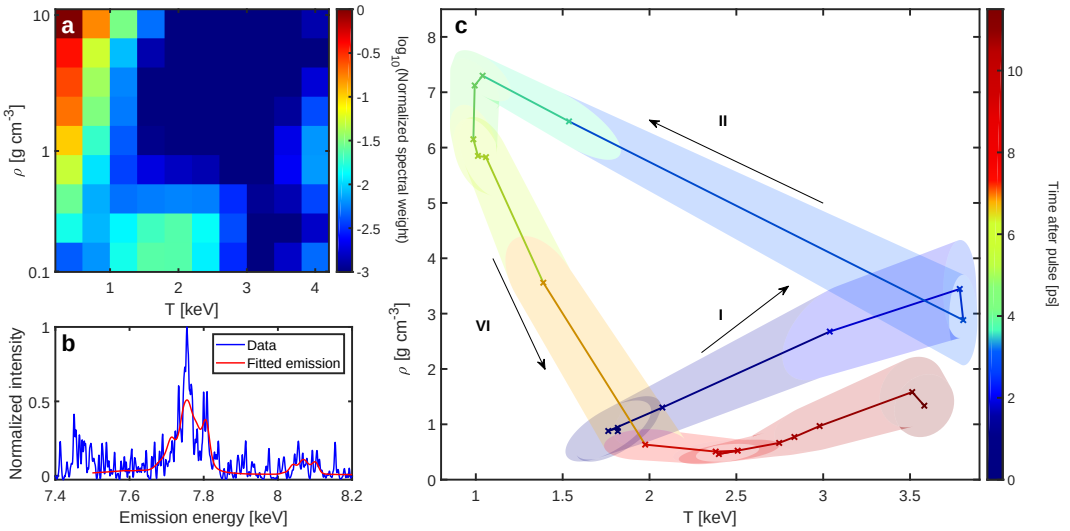

Figure 4.9: The corresponding evolution of a flat foil targets is shown to compare with Fig. 4.7. (a) + (b) Plasma conditions and spectral emission 7 ps after drive, showing the denser parts of the target beginning to expand, after being moderately heated by the highly energetic particles driven into the target, redistributing the energy. (c) The time evolution of the centroid of the distribution, where annotated parts of the dynamics can be understood similarly to nanowires as described in Sec.4.4 of the text. The evolution is not as rich, however, and points **III**-**V** do not feature.

lying satellite state populations not included in the HULLAC atomic database used for Ni satellite energy levels within the FLYCHK model, which is a limitation of the choice of collisional radiative code.

In order to visualize the full time evolution of the fitted plasma distribution, the centroid and variance of the fitted weights are tracked on the T-ρ grid, shown in Fig. 4.7b. Key aspects of the plasma evolution in time are labelled **I**-**VI**, which can be understood with the aid of simulations and theory [38, 94].

4.4 Plasma evolution

The formation of a uniform plasma from nanowires under the extreme intensities present at the Orion laser is a complex and dynamic process, as illustrated by the vermiform path of plasma conditions in Figs. 4.7b and 4.9c. The key features of the emitting plasma profile, indexed **I-VI**, can be understood to result from the plasma dynamics as:

I: **Initial laser heating** – The temperature of the observed emission increases to keV levels as the energy of the laser pulse is absorbed.

II: **Laser reflection and energy redistribution** – The target forms a plasma mirror and reflects the remainder of the laser pulse. Hot electrons redistribute energy in the target.

III: **Heating dense wire cores** – The dense cores of the nanowires are heated by MA-scale return currents.

IV: **Nanowire recollision** – The nanowires coulomb explode, and collide with neighbouring wires within the irradiated area, further heating the system.

V: **High temperature inertially confined stagnation** – The high temperature plasma emits while inertially confined by its volume.

VI: **Expansion and cooling** – The plasma expands and cools to the signal/noise limit of the XRSS.

Snapshots of a 2D PIC simulation of conditions in the nanowire target are shown in figure 4.10, which can be compared with the understood evolution from the

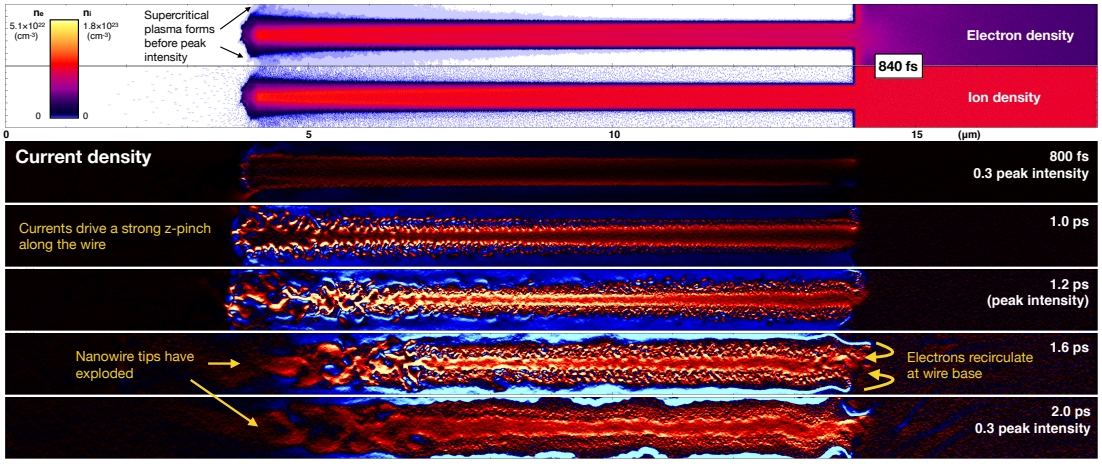

Figure 4.10: 2D PIC simulations showing snapshots of the conditions in the nanowire target on irradiation with p-polarized gaussian 600 fs FWHM pulse, with the peak at $t = 1200$ fs. Blue current density represents right-going electrons, and red denotes left-going.

fitted plasma emission.

During the initial heating of the system, the emission is broadened by the time resolution of the XRSS. The temporal broadening results in the initial observed density lower than 8.91 g cm^{-3} solid density, however this could also be in part due to the inter-wire channel filling before the onset of emission above the noise floor of the detector, as the bulk of the wire is not yet heated.

After sufficient time the expansion of the critical surface limits further laser heating. Hot electrons penetrate further into the target and can heat the dense core of the wires, however this lowers the average temperature of the plasma while increasing the volume that is emitting. The timescale of void closure for nanowire targets at these intensities is estimated as between 100 fs and 1 ps at the tips of the wires [39, 94].

The depletion of electrons from the tips of the nanowires draws a MA-scale

return current along the length of the wires, generating gigagauss magnetic fields. The return current, along with radially propagating shock fronts from the ablating wire edges forms can form Z-pinch, which compresses and heats the dense wire cores [38]. The nanowires then explode and collide, stimulating significant secondary heating in the target. The overall density of the emitting plasma plateaus at $\sim 1\,\mathrm{g\,cm^{-3}}$, or $\sim$11% solid density, corresponding to the initial $\sim$15% nanowire fill fraction. The width of the plasma distribution narrows in density as the system homogenizes along the length of the wires, seen in Fig. 4.7b as the height of the shaded region around the dynamical path. Transverse temperature gradients will still exist in the target due to the focal spot intensity profile, the distribution is not seen to collapse around a single T-ρ point within the resolution of the generalised functional form.

The large volume of high-temperature plasma undergoes a prolonged period of stagnation and homogenisation, along the full length of the heated wires. As the plasma fully thermalizes it begins to expand out of the plane of the target. At late time the plasma expands to low densities. The larger volume of nanowire plasma cools more slowly than the relatively thin layer in the foil target. This manifests as a slight increase in apparent density at late times, as emission from the cooler low-density regions drops below the dynamic range of the XRSS.

4.5 Discussion

The ability to probe the complete evolution of complex plasma conditions using time-resolved emission from single-shot XRSS data is vital in benchmarking and improving physical models. The sustained high temperatures and densities in the

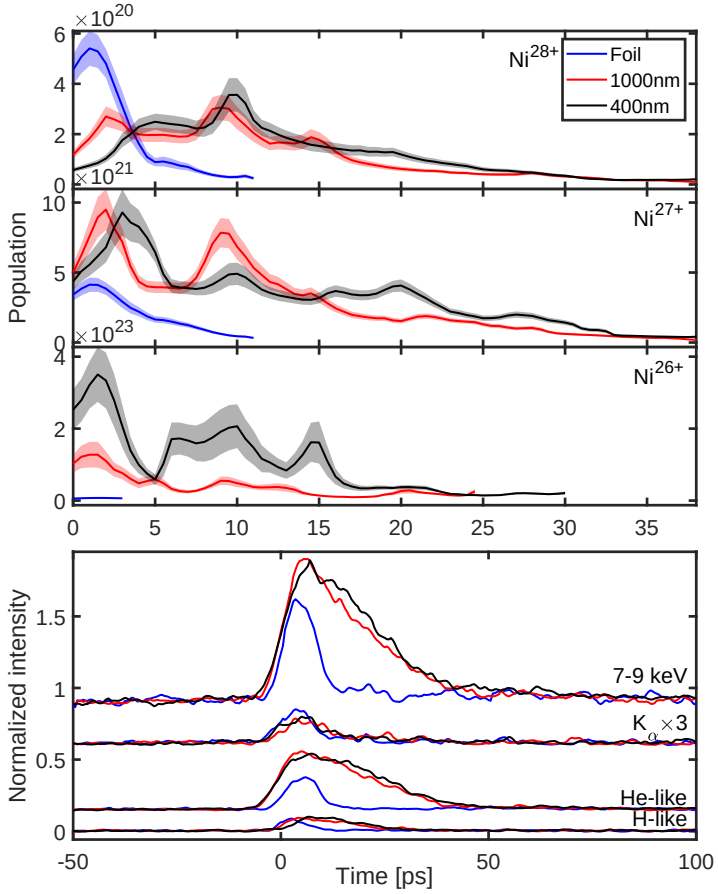

Figure 4.11: (a) Extracted FLYCHK ion populations for high-lying charge states for both nanowire and flat Ni targets, showing a late time jump for the nanowire targets, compared to (b) the spectrally integrated emission from the primary emission complexes, where no spike is discernable. Bands on the data represent the ion-population-weighted standard deviation of the ensemble fit to the time resolved spectral data.

nanowire plasma offer a unique platform bridging the regimes typically associated with particle-in-cell and radiation-hydrocodes. High computational expense and physical complexity from the wide-ranging spatio-temporal scales in this environment force any simulation to make approximations; without experimental data there is no way of identifying which of these are reasonable.

Analyzing the plasma evolution with FLYCHK also offers insights into the time-resolved ion populations from the ensemble fit to the data, including the predicted population of fully stripped Ni^{28+} ions, which are not spectroscopically observable. The fitted evolution of ion populations for both nanowire and flat Ni targets are plotted in Fig. 4.11a, where collisional heating can clearly be seen to generate a late-time jump in highly charged ion stages for nanowires, which cannot be discerned from the spectrally integrated line emission (Fig. 4.11b).

The 15% fill fraction of the nanowire targets, as well as the volumetric heating effects in the nanowire targets allows laser energy to penetrate further than the absorption length into the surface of the target. Heating nanowire targets volumetrically can result in a larger quantity of slightly lower temperature plasma, homogenised along the wire length, notable in the enhanced Ni^{27+} population from early time as well as the prolonged high-temperature stagnation seen in Fig. 4.7b. In contrast, the flat foils reach maximum ionization almost immediately, as the incident laser is able to heat the entire area of the focal spot directly, before rapidly cooling and expanding.

The 1000 nm diameter nanowire target exhibits some of the behaviour of both bulk and nanowire interaction, with notable early- and late-time heating events in the highly-charged ion populations seen in Fig. 4.11a. This dichotomous nature results in significant bimodal distributions in temperature and density which cannot be sufficiently resolved based on the limited resolution of the generalised functional form of the distribution, nor is tracking the centroid of a bimodal distribution a useful exercise. Nevertheless, the irregular wire spacing in both the 1000 nm and 400 nm arrays manifests as multiple ionization peaks in the time his-

tory; it is expected that a regularly-spaced array with a larger number of wires contained within the focal spot would exhibit a more clearly-defined evolution.

4.6 Conclusions

The method presented for extracting time-resolved plasma conditions presented here is applicable to many datasets. Whether time resolution comes from a pump-probe scheme, or a single-shot diagnostic. Computing an ensemble-averaged temperature-density profile can also be used in time-integrated diagnostics, yielding a similarly time integrated plasma distribution.

While the above-described method is not shown to be an exact inversion, or a singular mapping, it is capable of producing meaningful results which correspond well to the developing understanding of the prevalent nanowire dynamics at these incident intensities. The limitations of the fitting procedure are considered negligible in comparison to the signal:noise ratio present in the data, the energy resolution of the collected spectrum, intensity broadening effects, and the limitations of the FLYCHK 0-dimensional collisional-radiative code.

The ability to quantify dynamical plasma effects is crucial in expanding the understanding of high energy density physics, and improving the design of nanostructured targets to access these extreme states of matter. The potential to resolve the population of fully stripped Ni ions, which have no spectroscopic signature is a tantalising indication of the possible advancements when coupling existing plasma simulation capacity, detector architecture and fitting techniques.

5 Measurement of keV solid-density plasmas by nanofocused hard x-rays

As discussed in section 1.3.3, another route to creating HED systems is via direct heating with XFEL sources. Some of the limiting factors in creation of extreme systems using optical lasers are bypassed when using x-ray sources, as higher energy photons can penetrate further into the system and heat volumetrically without the need to modify the target to tailor its absorption properties. While optical lasers heat from the critical surface and generate large plasma parameter gradients – which can still be seen in the evolution of nanowire targets before homogenisation, as shown in Figure 4.7 – x-rays can ionize core electrons within the target over their attenuation length, typically $\mathcal{O}(\mu m)$, placing them in the continuum with keV energies. Heating of the bulk electrons occurs collisionally, while the ions with core holes can decay to emit characteristic x-rays or auger electrons to heat the system further. Although the physics used to create the extreme temperatures is different, the final system is comparable to the conditions generated in the nanowire laser target. The short timescale of heating using an XFEL means that hydrodynamic processes do not occur on the timescale of emission, so the density can be considered to be solid throughout heating. Also, as the characteristic emission observed is due to the creation of core holes in the system via incident x-rays, emission only lasts for the duration of the incident pulse.

The behaviour of solid-density plasma in the HED regime is of great importance in the study of stellar interiors and ICF as discussed in chapter 1, yet many phenomena such as nonlinear transport, partial ionization, strong coupling and

atomic processes are poorly understood in these conditions. The extreme peak brightness of XFELs gives the ability to retrieve single-shot, time-resolved diagnostics of WDM and HED, as seen in chapter 3, and to probe systems in similar conditions to the more dynamic optically heated systems. Volumetric heating to create a single plasma state to probe can allow more accurately bound measurements than in a spatially integrated diagnostic of optical laser experiments.

A correct description of how atoms and ions interact to lower the continuum energy level in a dense system is required to model the ionization balance, directly related to opacity and Equation of State (EOS) models. Iron is of particular interest in solar opacity models due to the solar radiation/convection boundary layer, where despite having a small concentration, iron plays a dominant role in governing radiation transport properties. Direct measurements at extreme conditions have been hindered by inevitable density gradients present in laser plasmas. Diagnosis of many laser-driven plasmas often relies on the presence of higher-order lines, eg. β or γ lines, at higher photon energies where the plasma is optically thin. Incorrectly assigning the IPD can lead to an incorrect characterisation of the bound states of the atom, and the upper levels of these transitions becoming part of the continuum. The scaling of the IPD with temperature and density was investigated by Ciricosta *et. al* by looking at not only pure Mg, Al and Si but also compounds which may be isochorically heated in the same way [13]. These early XFEL studies include the isochoric heating of Aluminium [11] and mixtures, using incident photon energies to track the K-edge of subsequent L-shell ionizations, which have shown data inconsistent with widely used IPD models, calling into question long-standing models of IPD and the deeper understanding of MEC.

As the capabilities of LCLS have extended over the years – with better performing more reliable x-ray pulses, novel seeding schemes to push to higher peak brightness, improved high photon energy performance, and nanofocusing potential – the opportunity has arisen to extend these isochoric heating studies to higher photon energy and higher Z elements with more complicated electronic structures. Studying the dependence of atomic structure, collisional rates and IPD across multiple elements in well controlled, reproducible conditions achievable by XFEL would allow models to be validated over a large range, in addition to uncovering the evolution of the bound states of these elements where predictions have been seen to fall far from observations [61].

Initial characterisation of the nano-focused XFEL beam showed saturation of the Fe K-shell photo-absorption mechanism, showing unambiguously that on average more than one 7 keV photon is absorbed per atom in the irradiated region. If energy coupled to the target has time to thermalize the charge state via collisions, the generated temperatures would be expected to be in the several 100's of eV.

5.1 Experiment

An experiment was undertaken at the Coherent X-ray Imaging (CXI) endstation of the LCLS XFEL to attempt to extend earlier results heating low-Z elements using soft x-rays to Fe, $Z = 26$. In earlier in-house beam time to characterise the nanofocused XFEL using a ronchi shearing technique [102, 29], measurements of absorption vs. intensity on Fe foils was observed to completely saturate the K-shell photo-absorption mechanism, indicating that the target was sufficiently irradiated that on average more than one photon is absorbed per atom. Corresponding K-

shell photoemission was at the time observed up to 5 L-shell holes. This work was extended to a full study of the K-shell emission of over a wide range of incident photon energies, 7 keV to 9 keV, to extract the resonance lines and ionization edges for single and double core hole features.

Spectral emission data was collected on a LiF 220 crystal reflecting onto an ePix100 camera. The target-crystal-camera distance was 169 mm, 70° from target normal, at a central Bragg angle of 40.39°, yielding a spectral range 6183 eV to 7335 eV. The key K-shell emission features lie above the K_α at 6403 eV and below the K_β at 7057 eV. Additional K_β satellite lines are expected to be present, however their intensity compared with the K_α is low except on resonance, and the required spectral range needed to observe all satellites was larger than could be accessed. The target 12.5 µm Fe foil was irradiated with XFEL pulses between 1.5 mJ to 2.5 mJ XFEL pulses in 50 fs FWHM at normal incidence in Kirkpatrick-Baez (KB)-focused spot sizes characterised at 80 nm × 110 nm FWHM, yielding peak on target intensities of up to $\sim 10^{20}\,\mathrm{W\,cm^{-2}}$ after accounting for ∼40% beamline transmission.

The central XFEL photon energy was tuned in 20 eV steps 7 keV to 8 keV, followed by 50 eV steps to 9 keV. The resulting spectral emission collected, normalized to a cross-section, $\partial_\omega \sigma$, of outgoing photons per solid angle per incident photon per eV are shown in figure 5.1.

The spectral analysis was performed using the range of techniques for Bragg spectroscopy and single photon counting detailed in Chapter 2, to optimize the signal/noise ratio over thousands of collected x-ray camera images. In total 18,633 XFEL shots were used to construct the image, averaging spectra from shots in

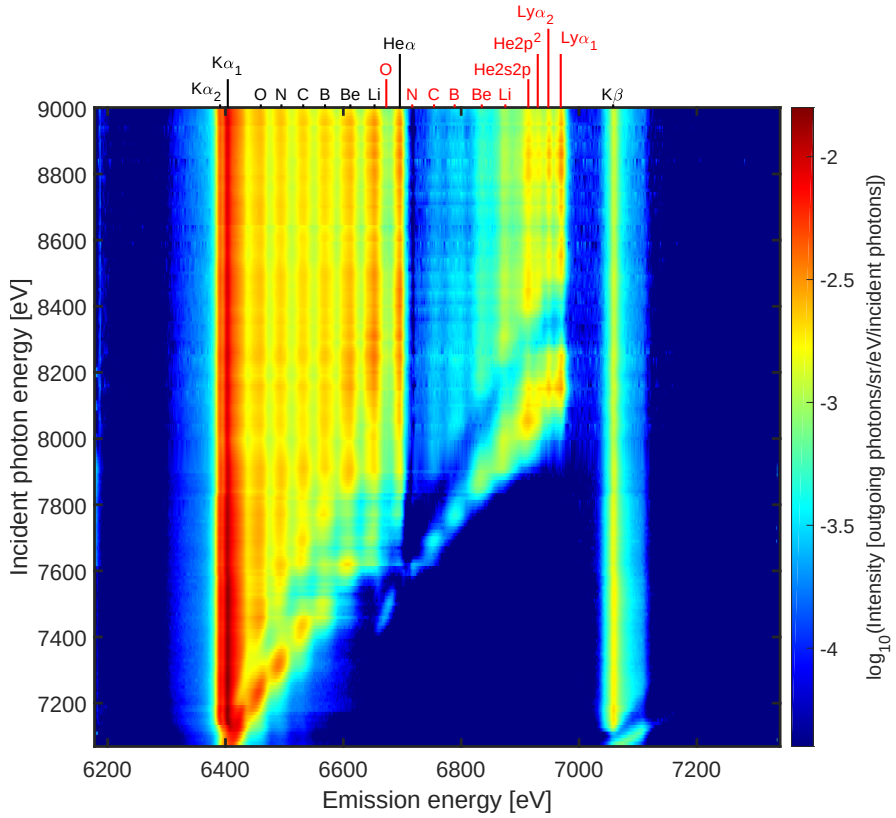

Figure 5.1: X-ray photoemission of keV XFEL-heated solid-density Fe. The energy of the K-edge of the 8 different L-shell ionization states are visible for all single (labelled in black) and double (in red) core hole electron configurations. The characteristic Kα satellite emission of each charge state is visible below the K-edge when the XFEL can resonantly heat the system via the K-M transition.

10 eV bins of central photon energy with a 1 eV energy contour spacing.

5.2 Spectral analysis

In order to construct a reliable unwarping of the spectrum as collected on the ePix100 camera, a generalised method for constructing the calibration was required. As the nano-focused XFEL spot effectively magnifies any angular jitter of the beam along its full length, the sample was scanned along the beam di-

rection, maximising the observed satellite emission to find best focus at regular intervals to account for any drift in the undulator. The normal approach of identifying a calibrant spectrum with known photon energies using an attenuated beam was not always possible due to the number of different target positions along the beam direction. The approach outlined in chapter 2 of maximising the contrast of the spectrum via integrating its square was taken, with a good initial parameter estimate from calibrations performed before small shifts in target position. For then mapping this calibration to shifts of Δz, the position of the origin on the camera and the target-crystal-camera distance was adjusted inline with the size of the shift – $\mathcal{O}(200\,\mu\text{m}\ )$ corresponding to ~ 4 pixels or $\sim 5\,\text{eV}$ – using the measured/calibrated geometry of the camera at 70° from normal.

Shots were only included in the spectral averaging if they were within 10 eV of the target photon energy, had measured pulse energy of 1.5 mJ to 2.5 mJ, were within 200 µm z-position of best focus (for a 0.7 m focal length, 78 µm × 78 µm FWHM source size). Additional checks were made on the recovered intensity, as any warping of the target Fe foil can result in a loss of ideal focus and therefore intensity of satellite emission. Spectra were normalized to the solid angle of emission, the spectral dispersion across the image, and incident beam energy (converted to an expected # of incident photons) to compute a scattering cross section. This normalization makes data from different pulse lengths directly comparable, as well as measurements of scattering length via different thickness targets.

Although documentation of the ePix series of cameras includes expected response, the micro-scale of detectors leads to small changes in pixel response, and fluctuations in temperature, or damage on previous experiments can affect mea-

surements. The gain, relative and absolute noise coefficients as described in chapter 2 of the particular camera in use were determined using attenuation scans on the experiment. By attenuating the incident beam to the point that characteristic x-ray emission lines were at a single photon level, and using the known energy dispersion across the image, single photon detection events as a function of energy were found. In this case the response had to be interpoated across the image rather than characterised on a pixel by pixel basis, as the x-ray emission lines only illuminated a small region on the camera - however background noise corrections were performed individually.

5.3 Measures of electronic structure of hot-dense Iron

The dataset presented here contains the K_α satellite emission from all K- and L-shell configurations, including visible population in highly non-thermal double core hole states. Details of some of the transitions responsible for the series of spectral lines are shown in figure 5.2 for the example of incident XFEL photon energy at 7.5 keV. Satellite emission from some K_α states is visible when the incident energy is below the K-edge; this is due to both collisional ionization of the L-shell of the previous charge state [34], e.g. $\mathrm{Fe}1s^1 2s^2 2p^3 + e^- \rightarrow \mathrm{Fe}1s^1 2s^2 2p^2 + 2e^-$, and electron recapture from higher charge states which can be generated through K-M heating. Resonant M-shell heating can be seen for both single and double core holes, including when the K_α satellite energy overlaps, as the binding energy of the M-shell is strongly affected by the shielding of inner shells. Double core hole states are generated via rapid sequential photoionization, only possible due to the extreme intensities of $\sim 10^5$ photons/atom.

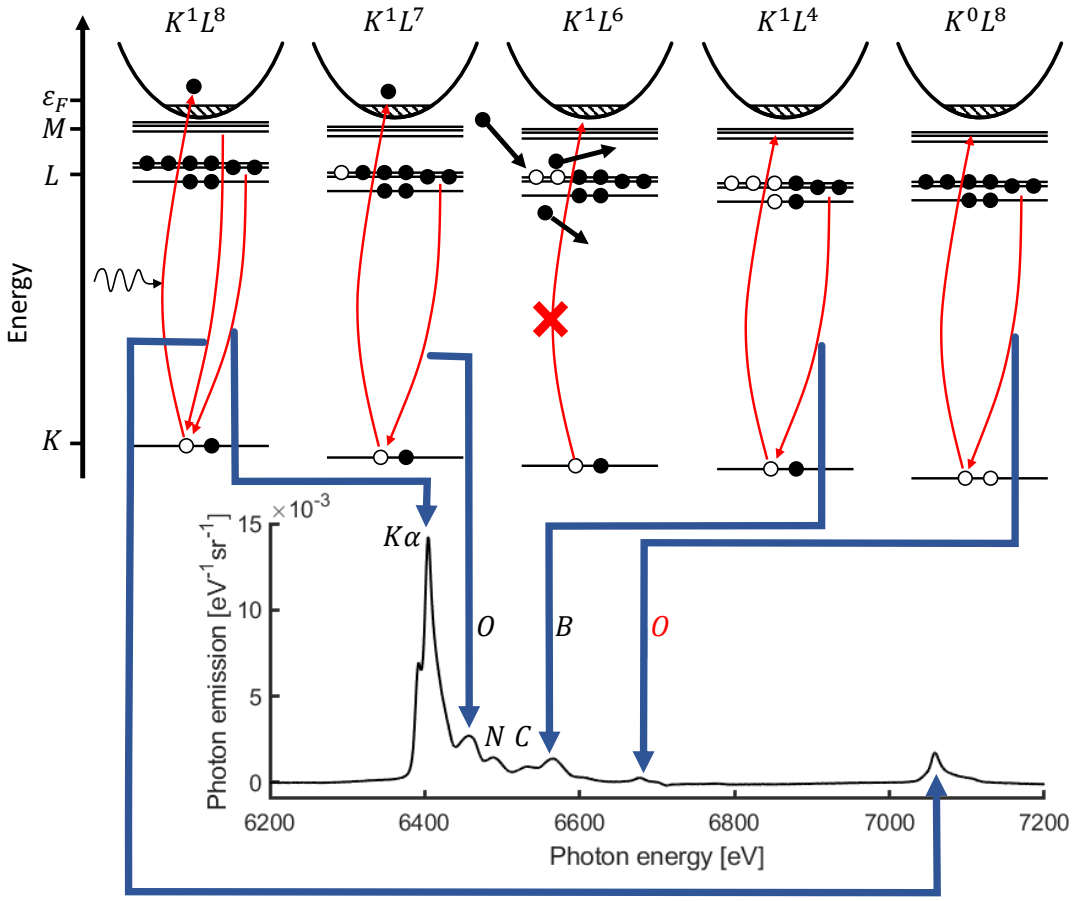

Figure 5.2: Schematic of atomic transition lines visible in Fe on irradiation with 7.5 keV XFEL, showing the K- and L-shell populations responsible for each satellite line, along with the corresponding element associated with the electron population. The population within the M-shell is not detailed as it only has a small effect on the binding energies, affecting the measured line width and symmetry. Resonant M-shell heating allows characteristic K_α emission from the Boron-like electron population of Fe below it's K-edge, while neighbouring charge states are visible due to collisional ionization or electron capture of the L-shell. The Oxygen-like double core hole M-shell is also resonant, however still very weak as by the time in the pulse that the intensity is sufficient to generate double core holes, the system is thermalized past the point where there is any significant population of full L-shell.

Upper level population	Single core hole 1s-2s-2p								M-shell being ionized	Double core hole 1s-2s-2p							
Charge state	1-2-6	1-2-5	1-2-4	1-2-3	1-1-3	1-1-2	1-1-1	1-0-1		0-2-6	0-2-5	0-2-4	0-2-3	0-1-3	0-1-2	0-1-1	0-0-1
3	6408																
4	6407	6436								6677							
5	6406	6435	6465							6676	6706						
6	6406	6435	6465	6496						6675	6705	6736					
7	6405	6434	6464	6495	6524				3d	6675	6705	6736	6768				
8	6404	6433	6464	6495	6523	6556				6674	6704	6735	6767	6796			
9	6404	6433	6463	6494	6523	6555	6589			6673	6704	6735	6767	6796	6829		
10	6407	6433	6463	6494	6523	6555	6589	6618		6673	6703	6735	6767	6796	6829	6864	
11	6411	6437	6463	6494	6523	6556	6589	6619		6677	6703	6734	6767	6796	6830	6864	6894
12	6416	6441	6467	6494	6523	6556	6590	6619	3d	6681	6707	6735	6767	6796	6830	6865	6895
13	6420	6446	6472	6499	6524	6557	6590	6620		6686	6712	6739	6767	6797	6831	6865	6895
14	6426	6451	6478	6505	6529	6558	6591	6621	3p	6691	6717	6745	6773	6797	6831	6866	6896
15	6431	6457	6483	6511	6535	6564	6593	6623		6697	6723	6751	6779	6803	6833	6868	6898
16	6436	6463	6490	6517	6541	6570	6599	6624		6703	6729	6757	6785	6810	6839	6869	6899
17	6441	6468	6496	6524	6548	6577	6606	6631	3s	6708	6736	6763	6792	6816	6846	6876	6901
18		6473	6502	6531	6556	6584	6614	6639		6713	6741	6770	6799	6824	6853	6883	6909
19			6507	6537	6563	6592	6622	6647	3p		6747	6776	6806	6831	6861	6891	6917
20				6543	6569	6600	6630	6655				6782	6812	6839	6869	6899	6925
21					6576	6607	6639	6664					6819	6846	6878	6908	6934
22						6614	6646	6673						6852	6884	6917	6943
23							6653	6681	3s						6892	6924	6952
24								6689								6932	6960
25																	6969

Table 1: List showing the range in K_α transition energies in eV of each single- and double-core-hole satellite charge state over the full range of M-shell ionization, calculated using the average atom code from International Atomic Energy Agency (IAEA). Note the weak dependence on M-shell spectator electrons, and the overlapping energy range of He_α and O-like double core hole.

The measured discrete transition energies are primarily due to the K- and L-shell populations, as these states are more strongly localised around the nucleus they contribute to the shielding of outer electron states to a greater degree, however the M-shell population also affects the transition energy. The shifts in energy due to M-shell ionization are small, leading to an observed asymmetry in the collected emission from the range of M-shell electron populations present in the system. The approximate effect of M-shell population on K_α satellite emission is shown in Table 1, where transition energies were calculated using the average atom approximation

code from IAEA, which itself uses the well known "Cowan's code" for Hartree-Fock calculations of the atomic structure. The full range of different satellite line energies was not calculated, in either 2s2p populations or 3s3p3d, as the number of configurations is large, at 2646 (when neglecting more detailed configurations incl. spin splitting), and a full sampling would not represent the states present in a thermalized system – however the full range of line energies is represented by the calculated ion stages.

The cold K_α is primarily generated from the low intensity "halo" around the XFEL focus, however the distribution of M-shell states probed by the XFEL gives an asymmetry on the blue side of the line profile, seen in figure 5.3. Similarly, this distribution affects the other satellite emission – however as higher charge state satellites are generated later in the XFEL pulse, after the M-shell has had more time to equilibrate over the fs timescale of collisional processes in the plasma – the asymmetry is seen to shift to being largely fully ionized M-shell with an asymmetry on the red side of the line profile. This effect is also seen in figure 5.3, where measured line position is compared against the range of calculated transition energies for different M-shell populations seen in Table 1. The observed peak in emission for each transition from higher L-shell ionization corresponds to higher M-shell ionization. Another way to see this shift in M-shell ionization would be to look at the emission on pumping with shorter XFEL pulse duration - where collisional processes will not have sufficient time to thermalize the M-shell, and therefore the observed satellite emission is moved to lower energy from the increased M-shell shielding.

The long delay in the onset of M-shell ionization is due to the primary heating

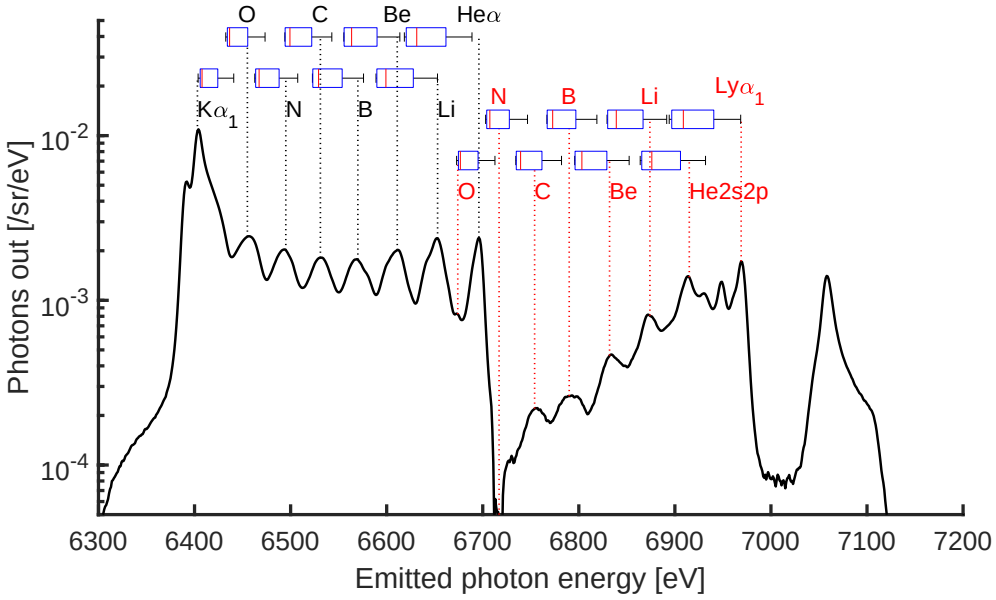

Figure 5.3: An emission spectrum for an incident photon energy above all satellite K-edges is plotted, mapping the peak position of each satellite onto the distribution of calculated transition energies from table 1. Positions of the observed peaks shift from the low energy (full M-shell) to high energy (ionized M-shell) side of the set of possible transition energies for increasing L-shell ionization, as higher charge states are generated later in the XFEL pulse and the M-shell has more time to thermalize.

mechanism being the generation of high-energy Auger electrons after photoionization, which initially are weakly coupled to the plasma system as their momentum transfer cross-section is low as illustrated in figure 1.2. These electrons with $\mathcal{O}(5\,\mathrm{keV})$ kinetic energy can quickly escape the focal spot, travelling $\sim 10\,\mathrm{nm}$, depositing their energy outside the region with the highest radiation intensity. Energy transport can impose limits on the minimum interaction volume, and correspondingly the increase in temperature associated with smaller focal spot sizes; with the $\sim 100\,\mathrm{nm}$ focal spot used here, energy transport is not thought to be

as significant in limiting the target response as the saturated K-shell absorption mechanism. High energy electrons are also those responsible for collisionally ionizing the system, which can result in emission from states above those the incident x-rays can directly photoionize the core electrons.

The peak in emission for the Nitrogen-like double core-hole is not seen in figure 5.3, as the ePix100 x-ray camera has a small gap between detector regions, where most of the N-like emission would have been collected. The position of the N-like peak was found from other data shots where the He_α fell on this region of the detector. The L-shell populations are largely thermal, as despite the $\sim 1\,\mathrm{keV}$ ionization energy of L-shell electrons, the large statistical weight of the continuum vs. bound states can produce fully L-shell ionized systems at a few hundred eV temperature. The peak emission for double core holes with larger L-shell populations are very low signal as the emission is only observed when ionization states are rapidly swept through by the rise in temperature of the target with the pulse. Double core-hole generation is strongly intensity dependent as they are produced via rapid sequential photoionization, competing with the emission rates of K-shell holes, which with their 7 keV ionization energy do not form a significant part of the system at temperatures in the 100's of eV.

In addition to determining collisional ionization rates by observing L-shell satellite emission below the relevant K-edge – where states are generated via electron impact ionization on the timescale of the core hole lifetime [34, 11] – the data is also compared to heating with a 10 fs XFEL pulse in Fig. 5.4. The 10 fs pulses were 0.8 mJ, giving comparable peak intensity on target; the final energy density achieved in the system will be lower, however as core-hole creation and emission

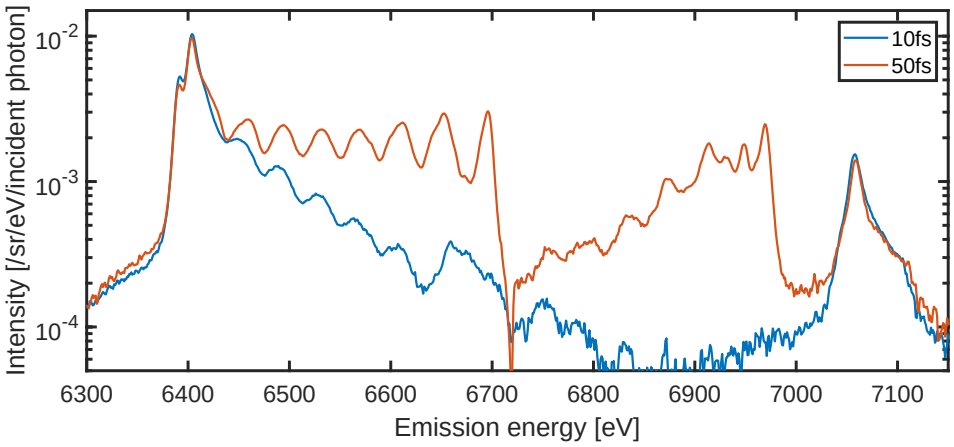

Figure 5.4: X-ray emission of 12.5 µm Fe foil for both 50 fs and 10 fs XFEL pulses averaged over 50 shots and 360 shots respectively, for incident pulses of 8970 eV photons with intensity $\sim 10^{20}\,\mathrm{W\,cm^{-2}}$. The spectra show shifted satellite peak position due to different populations of the M-shell at the time of emission. The exponential decay of charge states observed in 10 fs emission, seen in both single and double core holes, indicates that sequential photoionization is the dominant process at this time the system adapts the charge state distribution to high temperature.

predominantly occurs during the intense XFEL pulse, the collected emission can be viewed as an effective snapshot of the spectrum up to early times, when the 50 fs pulse would still be heating.

A schematic of the ion stages present throughout a 50 fs FWHM pulse, and the resulting time integrated emission cutoff at various stages through the pulse is shown in figure 5.5, to demonstrate the evolution of the collected spectrum. The modelling used here is only meant to be a schematic picture of the evolution of the plasma, using approximate rates for photoionization, emission, collisional ionization, auger decay and electron capture, and an additional imposed thermalization timescale of the L-shell toward a distribution given by the Saha equation. This results in a system of 28 coupled differential equations for populations of K^iL^j

($i \in [0..2]$, $j \in [0..8]$) and temperature for a single incident intensity profile. The scaling of transition rates with temperature, electron density and XFEL radiation field was approximated to have the correct dependence over the plasma parameter range, however absolute values are not compared.

The temperature of the plasma achieved with the shorter, 10 fs pulse will be lower, and therefore not directly comparable with the longer pulse, however additional information on the relative rates can be deduced from the spectrum. The natural linewidth of the Fe K_α can be use to infer the emission lifetime of core hole states at $\mathcal{O}$(fs), and can therefore occur multiple times throughout a 10 fs XFEL pulse. If L-shell collisional times were sufficiently short to thermalize on the timescale of the shorter pulse, small changes in incident energy would result in different satellite distributions corresponding to different achieved temperatures. The varying pulse energy shot to shot was not seen to result in different behaviour for short pulses, rather an exponential decay consistent with sequential photoionization via a saturated photoabsorption mechanism, and therefore it can be ascertained that the highly energetic auger- and photo-electrons are likely not thermalized with the L-shell on the timescale of emission during the short pulse envelope, although this could also be an effect of lower achieved temperature and lower free electron density. The double core-hole populations in particular demonstrate the dominance of radiative processes during the short pulse, as the exponential decay of double core-hole states is directly coupled to the single core-hole state generation. As the double core holes will only be generated in the central spot as they are strongly intensity dependent, if the centre of the focal spot had thermalized on this timescale to a higher temperature than the surrounding plasma – which

can generate single core holes with a less severe intensity dependence – we would expect to see a difference in the satellite distribution of single and double core holes.

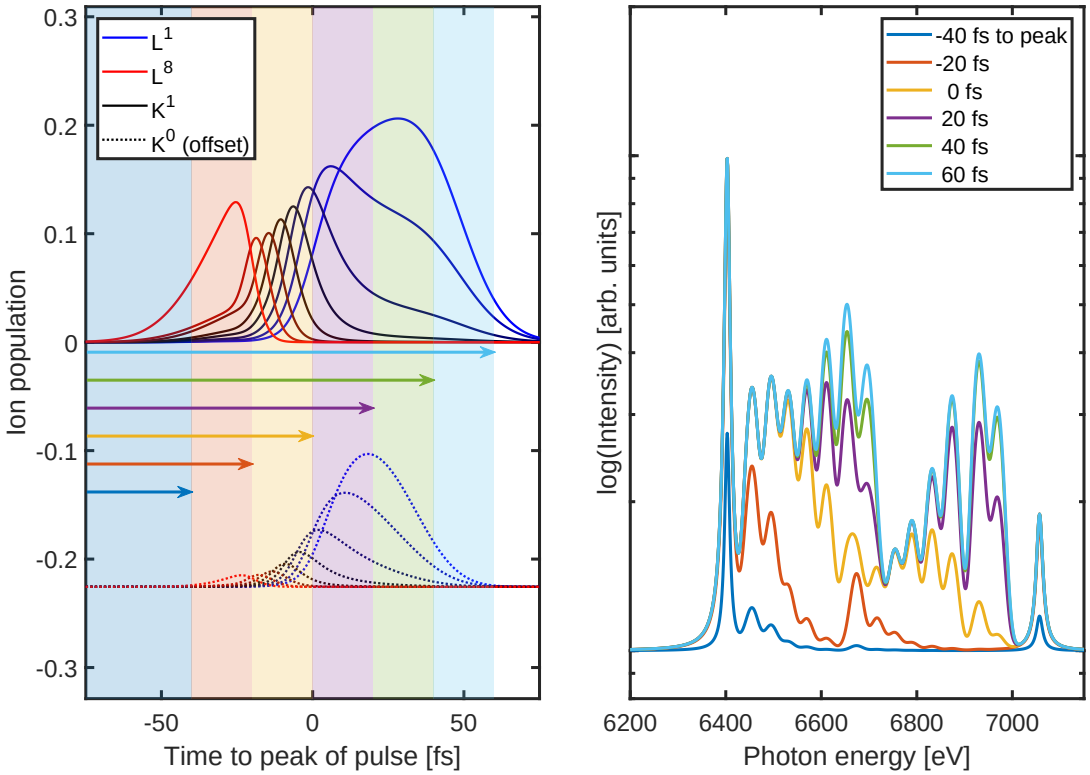

Figure 5.5: (a) A schematic model of the emitting ion stages present throughout the x-ray pulse, and (b) the resulting time integrated emission for time steps throughout the pulse collected on the spectrometer (mapped to single photon energies for each K^nL^m charge state) with a simple gaussian lineshape. Note that if the emission is only collected from earlier in the pulse, the ion stages exhibit an exponential decay as in Fig. 5.4, and at the peak of the pulse ion stages are rapidly transitioned through. The L-shell electrons thermalize at high temperatures, however, once the pump is removed the core-holes generated by x-ray absorption rapidly decay, and satellite K_α emission is no longer observed.

The peak position of satellite emission lines for the shorter pulse is also slightly

shifted within the range of transition energies due to M-shell spectator electrons. This is likely due to the short time of interaction not being sufficient for the bulk and M-shell electrons thermalize with the hot photoelectrons which have low scattering cross sections (figure 1.2). The shift in peak position is primarily seen in lower ion charges, e.g. O-like and the asymmetry of the K_α, as higher ion stages are generated later in the pulse when there has been more time to remove M-shell electrons.

5.4 Summary

Here a description of how the data on isochorically heated Iron was collected and processed has been detailed, the atomic transitions generating the array of spectral features explained, along with a preliminary comparison of spectra to calculated line positions. A full exploration of the models used to describe collisional rates, IPD and atomic processes was not undertaken as it fell outside the scope of this project, and is being furthered elsewhere. Future work to model the emitting plasma in 2D, extract measures of non-thermal electron population, and accurately bound the relative contribution of competing transition rates promise to further illuminate the complex dynamics at play on the short timescale of XFEL heating. The techniques used in spectral processing and data analysis were applied to hundreds of thousands of collected images for this experiment alone, synthesising only those that achieved the desired conditions in the target, and validating the routines' performance on real data for use on future experiments and diagnostics.

The brief discussion of the myriad of effects contained within the dataset provided a rich platform for describing these XFEL heated HED systems, and is

a useful example of the XFEL produced isochoric systems to compare with the complexity of diagnosing optical laser experiments, where in addition to opacity effects, experiments are often limited to single-shot statistics. The promised great potential of new, higher rep-rate facilities is the ability to pursue experiments to accurately bound physically meaningful quantities across large parameter spaces, improved by online diagnostics and active feedback in experiments. The experiment presented here demonstrates all the principles required to implement such a system: a rich dataset, modelling capability and fast data processing with well characterised errors. Extending such an experiment over multiple orders of magnitude in intensity, wide ranges of photon energy, and over different elements and mixtures could provide a more complete characterisation of hot-dense systems to benchmark physical models.

6 Conclusions

6.1 Summary and conclusions

This thesis has presented the developing understanding of spectroscopic studies of isochorically heated WDM and HED systems, with a range of techniques used to create and diagnose the extreme conditions within laser targets. The use of both high intensity optical laser systems as well as XFEL studies at the frontier of laser technology accesses a wide range of systems relevant to astrophysical and ICF plasma conditions.

Developments of more accurate statistical descriptions of photons incident on x-ray detectors was critical in improving signal/noise of measurements; allowing detailed plasma dynamics of nanowires over its full emission duration to be extracted, RIXS signals to be resolved over 5 orders of magnitude, and reconstruction of extremely low-level satellite emission in XFEL heated Fe. The techniques presented here have also been adapted in part to contribute toward other work including coherent x-ray diffraction, inelastic x-ray scattering of phonons, and complete forward-models of x-ray area detectors.

A proof-of-principle temperature measurement of solid density transient XFEL heated Ni was bounded using observations of RIXS of detuned K_α photons scattered via L-M transitions. This experiment was only possible using the extreme brightness of XFELs to provide the level of signal required on a single shot basis. Modelling the temperature alone proved to be insufficient, as the temperatures $\mathcal{O}(10\,\mathrm{eV})$ causes partial ionization and IPD. By modelling the spectra, the functional dependence of IPD can be recovered, and was shown to be in agreement

with DFT calculations, over the limited range of these initial measurements.

Recovering an accurate description of evolving plasma conditions at multi-keV temperatures using experimental data rather than relying on a spatially integrated average description, and modelling internal fluctuations has been an ongoing effort in laser-plasma systems, as the range of instabilities present that can be present is large. Using FLYCHK to model the spectral emission of high temperature Ni plasmas over a range of different conditions, a limited form of the temporally resolved plasma parameter distribution of Ni nanowires irradiated with a relativistic petawatt laser was shown to match extremely well with the understanding of their dynamics from PIC code work. The performance of nanostructured targets has proved challenging to scale up to kilojoule facilities due to the extreme contrast requirements, and correspondingly difficult to model due to the imposed spatial scales of the nanostructure, as well as hydrodynamic timescales. These first results of kilojoule-scale nanowire interaction, along with a complete description of their evolution in time, provide an excellent platform to diagnose limitations in order to improve their performance as bright x-ray backlighters, particle sources, or platforms for ultra-HED science.

The method of extracting the plasma parameter distribution detailed in chapter 4 is potentially useful across a variety of studies, where spatio-temporal scales are integrated in the diagnostic. Furthermore, additional details of plasma conditions such as the ionization balance in the system – including those with no spectroscopic signature – can elucidate otherwise indecipherable aspects of system dynamics.

Finally, extending the spectral analysis methods presented here to nanofocused XFEL studies links the two previous experiments, as using low signal spectra,

measurements of Fe K_α satellites are used to inform the conditions present in extremely short lived high-temperature states of Fe. Observations of K-M heating here place bounds on the atomic levels present in a highly ionized system, where spatio-temporal scales are integrated over in the collected emission. Shifted satellite emission line energies due to shielding of ions generated at different times during heating gives an indication of M-shell collisional ionization rates from non-thermal electrons created via Auger decays and L-shell absorption, which are initially largely decoupled from the plasma and transport energy out of the focal spot. Reasoned estimates of the temperature achieved to observe the wide range of satellite emission in Fe place the XFEL heated system at several hundred eV, higher temperature than previous studies on low-Z prototypical metals and mixtures which achieved $\sim$180 eV solid density plasma on XFEL.

6.2 Future work

Mapping collected spectral emission from a laser target to conditions present in the interaction volume is vital in comprehending the complex dynamics present within systems. Accurate measurements and determination of the EOS is essential in understanding the structure of many astrophysicsal objects. Mapping the phase diagram of such systems requires direct measurements of the achieved density, pressure and temperature conditions. To date temperature diagnosis has often relied on either hydrodynamic simulations or XRTS measurements - which have been shown to have potentially large discrepancies. The proof-of-principle single-shot, time-resolved temperature diagnosis using RIXS offers a potential route forward, where further experiments could exploit higher resolution spectra to resolve fea-

tures within the DOS and the shifting Fermi-Dirac population function as a direct measurement of bulk temperature. Another applicaton of particular interest is the potential to observe the rebinding of atomic states in highly charged ions, or the timescale of equilibration in XFEL vs. optically heated systems, in order to distinguish between prevalent models of IPD. The discussion of data on XFEL-heated Fe will hopefully inform ongoing efforts to model these complicated and short-lived systems more completely, in order to accurately diagnose the relative contributions of different stimuli of observed transitions.

In order to achieve single shot diagnosis of conditions, recovering the signal from every photon is valuable, along with a complete description of the error in the recovered spectrum. The methods described in chapter 2 have proved useful across a range of experiments, using a variety of different detectors and geometries. While they are presented here in the context of spectroscopy, single photon statistics can be applied to other techniques including coherent x-ray diffraction, where accurate accounting of single photon statistics in azimuthal variation of Debye-Scherrer rings or spots could remove additional sources of noise, of interest in shocked studies, where signal/noise is often limited for features of interest. The emphasis on maintaining SPC-informed techniques that are still capable of performing at high repetition-rate facilities can also potentially improve online diagnostics, and active feedback to more rapidly limit the error bounds on physically meaningful parameters. While in this work the detailed analysis was performed *post hoc*, the experimental plan was often refined using online monitoring. Improving this capability is seen as fundamental in exploiting high rep-rate experiments, where the quantities of data produced are well past the ability of any one person to

synthesise without algorithmic intervention.

To conclude, the work in this thesis describes the successful application of single-photon counting informed algorithms in determining accurate measures of spectral emission for a variety of isochorically heated systems. Measured emission and scattering spectra are used in conjunction with modelling efforts in DFT and PIC to provide a more complete picture of conditions present in XFEL and optical laser-plasma targets. Accurate characterisation of spatially and temporally resolved conditions provides a benchmark for plasma simulation capacity, and insights into the factors affecting the targets response to a laser drive, which can be used to inform future efforts investigating conditions relevant to astrophysical systems and ICF.

References

[1] DB Guenther, P Demarque, Y-C Kim, and MH Pinsonneault. Standard solar model. *The Astrophysical Journal*, 387:372–393, 1992.

[2] CA Iglesias and FJ Rogers. Opacities for the solar radiative interior. *The Astrophysical Journal*, 371:408–417, 1991.

[3] John Lindl. Development of the indirect-drive approach to inertial confinement fusion and the target physics basis for ignition and gain. *Physics of plasmas*, 2(11):3933–4024, 1995.

[4] John D Lindl, Peter Amendt, Richard L Berger, S Gail Glendinning, Siegfried H Glenzer, Steven W Haan, Robert L Kauffman, Otto L Landen, and Laurence J Suter. The physics basis for ignition using indirect-drive targets on the national ignition facility. *Physics of plasmas*, 11(2):339–491, 2004.

[5] Colin N Danson, Constantin Haefner, Jake Bromage, Thomas Butcher, Jean-Christophe F Chanteloup, Enam A Chowdhury, Almantas Galvanauskas, Leonida A Gizzi, Joachim Hein, David I Hillier, et al. Petawatt and exawatt class lasers worldwide. *High Power Laser Science and Engineering*, 7, 2019.

[6] EL Clark, K Krushelnick, JR Davies, Matthew Zepf, M Tatarakis, FN Beg, A Machacek, PA Norreys, MIK Santala, I Watts, et al. Measurements of energetic proton transport through magnetized plasma from intense laser interactions with solids. *Physical Review Letters*, 84(4):670, 2000.

[7] RA Snavely, MH Key, SP Hatchett, TE Cowan, Markus Roth, TW Phillips, MA Stoyer, EA Henry, TC Sangster, MS Singh, et al. Intense high-energy proton beams from petawatt-laser irradiation of solids. *Physical review letters*, 85(14):2945, 2000.

[8] Stephen P Hatchett, Curtis G Brown, Thomas E Cowan, Eugene A Henry, Joy S Johnson, Michael H Key, Jeffrey A Koch, A Bruce Langdon, Barbara F Lasinski, Richard W Lee, et al. Electron, photon, and ion beams from the relativistic interaction of petawatt laser pulses with solid targets. *Physics of Plasmas*, 7(5):2076–2082, 2000.

[9] Max Tabak, James Hammer, Michael E Glinsky, William L Kruer, Scott C Wilks, John Woodworth, E Michael Campbell, Michael D Perry, and Rodney J Mason. Ignition and high gain with ultrapowerful lasers. *Physics of Plasmas*, 1(5):1626–1634, 1994.

[10] M Roth, TE Cowan, MH Key, SP Hatchett, C Brown, W Fountain, J Johnson, DM Pennington, RA Snavely, SC Wilks, et al. Fast ignition by intense laser-accelerated proton beams. *Physical Review Letters*, 86(3):436, 2001.

[11] SM Vinko, O Ciricosta, BI Cho, K Engelhorn, H-K Chung, CRD Brown, T Burian, J Chalupskỳ, RW Falcone, C Graves, et al. Creation and diagnosis of a solid-density plasma with an x-ray free-electron laser. *nature*, 482(7383):59, 2012.

[12] A. Lévy, P. Audebert, R. Shepherd, J. Dunn, M. Cammarata, O. Ciricosta, F. Deneuville, F. Dorchies, M. Fajardo, C. Fourment, D. Fritz, J. Fuchs,

J. Gaudin, M. Gauthier, A. Graf, H. J. Lee, H. Lemke, B. Nagler, J. Park, O. Peyrusse, A. B. Steel, S. M. Vinko, J. S. Wark, G. O. Williams, D. Zhu, and R. W. Lee. The creation of large-volume, gradient-free warm dense matter with an x-ray free-electron laser. *Physics of Plasmas*, 22(3), 2015.

[13] O Ciricosta, SM Vinko, B Barbrel, DS Rackstraw, TR Preston, T Burian, J Chalupskỳ, Byeoung Ick Cho, H-K Chung, GL Dakovski, et al. Measurements of continuum lowering in solid-density plasmas created from elements and compounds. *Nature communications*, 7:11713, 2016.

[14] Paul Emma, R Akre, J Arthur, R Bionta, C Bostedt, J Bozek, A Brachmann, P Bucksbaum, Ryan Coffee, F-J Decker, et al. First lasing and operation of an ångstrom-wavelength free-electron laser. *nature photonics*, 4(9):641, 2010.

[15] Siegfried Glenzer, Luke Fletcher, Eric Galtier, B Nagler, Roberto Alonso-Mori, B Barbrel, S Brown, D Chapman, Zhijiang Chen, Chandra Curry, F Fiuza, E Gamboa, Maxence Gauthier, D Gericke, Arianna Gleason, Sebastian Göde, Eduardo Granados, P Heimann, J Kim, and Hyun Jeong Lee. Matter under extreme conditions experiments at the linac coherent light source. *Journal of Physics B: Atomic, Molecular and Optical Physics*, 49:092001, 05 2016.

[16] G Alberto, Pedro Velarde, Francois de Gaufridy, David Portillo, Manuel Cotelo, Alfonso Barbas, Agustín González, and Philippe Zeitoun. Non-maxwellian electron distributions in time-dependent simulations of low-z

materials illuminated by a high-intensity x-ray laser. *High Energy Density Physics*, 9(3):542–547, 2013.

[17] SA Khrapak, AV Ivlev, GE Morfill, and SK Zhdanov. Scattering in the attractive yukawa potential in the limit of strong interaction. *Physical review letters*, 90(22):225002, 2003.

[18] TS Ramazanov and SK Kodanova. Coulomb logarithm of a nonideal plasma. *Physics of Plasmas*, 8(11):5049–5050, 2001.

[19] TFR Equipe. Tokamak plasma diagnostics. *Nuclear Fusion*, 18(5):647, 1978.

[20] John Dawson and Carl Oberman. High-frequency conductivity and the emission and absorption coefficients of a fully ionized plasma. *The Physics of Fluids*, 5(5):517–524, 1962.

[21] CD Decker, WB Mori, JM Dawson, and T Katsouleas. Nonlinear collisional absorption in laser-driven plasmas. *Physics of Plasmas*, 1(12):4043–4049, 1994.

[22] DW Forslund, JM Kindel, and K Lee. Theory of hot-electron spectra at high laser intensity. *Physical Review Letters*, 39(5):284, 1977.

[23] Donna Strickland and Gerard Mourou. Compression of amplified chirped optical pulses. *Optics communications*, 56(3):219–221, 1985.

[24] PM Nilson, AA Solodov, JF Myatt, W Theobald, PA Jaanimagi, L Gao, C Stoeckl, RS Craxton, JA Delettrez, B Yaakobi, et al. Scaling hot-electron

generation to high-power, kilojoule-class laser-solid interactions. *Physical review letters*, 105(23):235001, 2010.

[25] AFA Bott, C Graziani, P Tzeferacos, TG White, DQ Lamb, G Gregori, and AA Schekochihin. Proton imaging of stochastic magnetic fields. *Journal of Plasma Physics*, 83(6), 2017.

[26] Jena Meinecke, HW Doyle, Francesco Miniati, AR Bell, R Bingham, R Crowston, RP Drake, Milad Fatenejad, Michel Koenig, Yasuhiro Kuramitsu, et al. Turbulent amplification of magnetic fields in laboratory laser-produced shock waves. *Nature Physics*, 10(7):520, 2014.

[27] Ingo Uschmann, Kazuhiza Fujita, Izam Niki, Randolf Butzbach, Hiroaki Nishimura, Jiro Funakura, Mitsuo Nakai, Eckhart Förster, and Kunioki Mima. Time-resolved ten-channel monochromatic imaging of inertial confinement fusion plasmas. *Applied optics*, 39(31):5865–5871, 2000.

[28] AL Kritcher, T Döppner, D Swift, J Hawreliak, G Collins, J Nilsen, B Bachmann, E Dewald, D Strozzi, S Felker, et al. Probing matter at gbar pressures at the nif. *High Energy Density Physics*, 10:27–34, 2014.

[29] Bob Nagler, Andrew Aquila, Sébastien Boutet, Eric C Galtier, Akel Hashim, Mark S Hunter, Mengning Liang, Anne E Sakdinawat, Christian G Schroer, Andreas Schropp, et al. Focal spot and wavefront sensing of an x-ray free electron laser using ronchi shearing interferometry. *Scientific reports*, 7(1):13698, 2017.

[30] Sébastien Boutet and Garth J Williams. The coherent x-ray imaging (cxi) instrument at the linac coherent light source (lcls). *New Journal of Physics*, 12(3):035024, 2010.

[31] Henry N Chapman, Anton Barty, Stefano Marchesini, Aleksandr Noy, Stefan P Hau-Riege, Congwu Cui, Malcolm R Howells, Rachel Rosen, Haifeng He, John CH Spence, et al. High-resolution ab initio three-dimensional x-ray diffraction microscopy. *JOSA A*, 23(5):1179–1200, 2006.

[32] Matthias Hoener, Li Fang, Oleg Kornilov, Oliver Gessner, Stephen T Pratt, Markus Gühr, Elliot P Kanter, Cosmin Blaga, Christoph Bostedt, John D Bozek, et al. Ultraintense x-ray induced ionization, dissociation, and frustrated absorption in molecular nitrogen. *Physical review letters*, 104(25):253002, 2010.

[33] CE Wehrenberg, David McGonegle, C Bolme, A Higginbotham, A Lazicki, HJ Lee, B Nagler, H-S Park, BA Remington, RE Rudd, et al. In situ x-ray diffraction measurement of shock-wave-driven twinning and lattice dynamics. *Nature*, 550(7677):496–499, 2017.

[34] QY van den Berg, EV Fernandez-Tello, T Burian, J Chalupskỳ, H-K Chung, O Ciricosta, GL Dakovski, V Hájková, P Hollebon, L Juha, et al. Clocking femtosecond collisional dynamics via resonant x-ray spectroscopy. *Physical review letters*, 120(5):055002, 2018.

[35] DS Rackstraw, O Ciricosta, SM Vinko, B Barbrel, T Burian, J Chalupskỳ, Byeoung Ick Cho, H-K Chung, GL Dakovski, K Engelhorn, et al. Sat-

urable absorption of an x-ray free-electron-laser heated solid-density aluminum plasma. *Physical review letters*, 114(1):015003, 2015.

[36] Bob Nagler, Ulf Zastrau, Roland R Fäustlin, Sam M Vinko, Thomas Whitcher, AJ Nelson, Ryszard Sobierajski, Jacek Krzywinski, Jaromir Chalupsky, Elsa Abreu, et al. Turning solid aluminium transparent by intense soft x-ray photoionization. *Nature Physics*, 5(9):693, 2009.

[37] E Garcia Saiz, Gianluca Gregori, Dirk O Gericke, Jan Vorberger, B Barbrel, RJ Clarke, Robert R Freeman, SH Glenzer, FY Khattak, M Koenig, et al. Probing warm dense lithium by inelastic x-ray scattering. *Nature Physics*, 4(12):940–944, 2008.

[38] M. P. Hill, O. Humphries, R. Royle, B. Williams, M. G. Ramsay, A. Miscampbell, P. Allan, C. R. D. Brown, L. M. R. Hobbs, S. F. James, D. J. Hoarty, R. S. Marjoribanks, J. Park, R. A. London, R. Tommasini, A. Pukhov, C. Bargsten, R. Hollinger, V. N. Shlyaptsev, M. G. Capeluto, J. J. Rocca, and S. M. Vinko. Volumetric heating of nanowire arrays to kev temperatures using kilojoule-scale petawatt laser interactions, 2020.

[39] Robin S Marjoribanks, L Lecherbourg, JE Sipe, G Kulcsàr, A Héron, J-C Adam, A Miscampbell, G Thomas, R Royle, O Humphries, et al. Ultrafast laser-matter interaction with nanostructured targets. In *X-Ray Lasers and Coherent X-Ray Sources: Development and Applications XIII*, volume 11111, page 111110L. International Society for Optics and Photonics, 2019.

[40] OS Humphries, RS Marjoribanks, Q Berg, EC Galtier, MF Kasim, HJ Lee, AJF Miscampbell, B Nagler, R Royle, JS Wark, et al. Mapping the electronic structure of warm dense nickel via resonant inelastic x-ray scattering. *arXiv preprint arXiv:2001.05813*, 2020.

[41] BA Hammel, CJ Keane, MD Cable, DR Kania, JD Kilkenny, RW Lee, and R Pasha. X-ray spectroscopic measurements of high densities and temperatures from indirectly driven inertial confinement fusion capsules. *Physical review letters*, 70(9):1263, 1993.

[42] Thomas R Preston, Sam M Vinko, Orlando Ciricosta, Hyun-Kyung Chung, Richard W Lee, and Justin S Wark. The effects of ionization potential depression on the spectra emitted by hot dense aluminium plasmas. *High Energy Density Physics*, 9(2):258–263, 2013.

[43] JD Kilkenny, RW Lee, MH Key, and JG Lunney. X-ray spectroscopic diagnosis of laser-produced plasmas, with emphasis on line broadening. *Physical Review A*, 22(6):2746, 1980.

[44] PW Lake, JE Bailey, GA Rochau, TC Moore, D Petmecky, and P Gard. Time-and space-resolved elliptical crystal spectrometers for high energy density physics research. *Review of scientific instruments*, 75(10):3690–3692, 2004.

[45] Hendrik A Kramers and Werner Heisenberg. Über die streuung von strahlung durch atome. *Zeitschrift für Physik A Hadrons and Nuclei*, 31(1):681–708, 1925.

[46] William Henry Bragg and William Lawrence Bragg. The reflection of x-rays by crystals. *Proceedings of the Royal Society of London. Series A, Containing Papers of a Mathematical and Physical Character*, 88(605):428–438, 1913.

[47] Junji Miyahara, Kenji Takahashi, Yoshiyuki Amemiya, Nobuo Kamiya, and Yoshinori Satow. A new type of x-ray area detector utilizing laser stimulated luminescence. *Nuclear Instruments and Methods in Physics Research Section A: Accelerators, Spectrometers, Detectors and Associated Equipment*, 246(1-3):572–578, 1986.

[48] Georg E Schulz and Gerd Rosenbaum. The multi-wire proportional chamber as an area detector for protein crystallography in comparison with photographic film; guidelines for future development of area detectors. *Nuclear Instruments and Methods*, 152(1):205–208, 1978.

[49] Philip Hart, Sébastien Boutet, Gabriella Carini, Mikhail Dubrovin, Brian Duda, David Fritz, Gunther Haller, Ryan Herbst, Sven Herrmann, Chris Kenney, et al. The cspad megapixel x-ray camera at lcls. In *X-Ray free-electron lasers: beam diagnostics, beamline instrumentation, and applications*, volume 8504, page 85040C. International Society for Optics and Photonics, 2012.

[50] PA Hart, G Blaj, P Caragiulo, G Carini, A Dragone, G Haller, J Hasi, R Herbst, S Herrmann, C Kenney, et al. Characterization of the epix10k camera at ssrl and lcls. In *2014 IEEE Nuclear Science Symposium and Medical Imaging Conference (NSS/MIC)*, pages 1–4. IEEE, 2014.

[51] B Markovic, A Dragone, P Caragiulo, R Herbst, K Nishimura, B Reese, S Herrmann, P Hart, G Blaj, J Segal, et al. Design and characterization of the epix100a: A low noise integrating pixel asic for lcls detectors. In *2014 IEEE Nuclear Science Symposium and Medical Imaging Conference (NSS/MIC)*, pages 1–3. IEEE, 2014.

[52] R. C. Alig, S. Bloom, and C. W. Struck. Scattering by ionization and phonon emission in semiconductors. *Phys. Rev. B*, 22:5565–5582, Dec 1980.

[53] F. GARWOOD. (i) Fiducial Limits for the Poisson Distribution. *Biometrika*, 28(3-4):437–442, 12 1936.

[54] U Zastrau, A Woldegeorgis, E Förster, R Loetzsch, H Marschner, and I Uschmann. Characterization of strongly-bent hapg crystals for von-hámos x-ray spectrographs. *Journal of Instrumentation*, 8(10):P10006, 2013.

[55] H Shiraga, M Nakasuji, M Heya, and N Miyanaga. Two-dimensional sampling-image x-ray streak camera for ultrafast imaging of inertial confinement fusion plasmas. *Review of scientific instruments*, 70(1):620–623, 1999.

[56] Edward V. Marley. *The Production and Spectroscopic Characterization of High Temperature, High Density Plasmas with Minimal Gradients*. PhD thesis, University of California, Davis, 2016. Copyright - Database copyright ProQuest LLC; ProQuest does not claim copyright in the individual underlying works; Last updated - 2019-10-19.

[57] S. M. Vinko, O. Ciricosta, T. R. Preston, D. S. Rackstraw, C.R.D. Brown, T. Burian, J. Chalupský, B. I. Cho, H.-K. Chung, K. Engelhorn, R. W. Falcone, R. Fiokovinini, V. Hájková, P. a. Heimann, L. Juha, H. J. Lee, R. W. Lee, M. Messerschmidt, B. Nagler, W. Schlotter, J. J. Turner, L. Vysin, U. Zastrau, and J. S. Wark. Investigation of femtosecond collisional ionization rates in a solid-density aluminium plasma. *Nature Communications*, 6:6397, 2015.

[58] AB Zylstra, JA Frenje, PE Grabowski, CK Li, GW Collins, P Fitzsimmons, S Glenzer, F Graziani, SB Hansen, SX Hu, et al. Measurement of charged-particle stopping in warm dense plasma. *Physical review letters*, 114(21):215002, 2015.

[59] Michael P Desjarlais, Christian R Scullard, Lorin X Benedict, Heather D Whitley, and Ronald Redmer. Density-functional calculations of transport properties in the nondegenerate limit and the role of electron-electron scattering. *Physical Review E*, 95(3):033203, 2017.

[60] Yuan Ping, Heather D Whitley, Andrew McKelvey, Gregory E Kemp, Phillp A Sterne, Ronnie Shepherd, Marty Marinak, Rui Hua, Farhat N Beg, and Jon H Eggert. Heat-release equation of state and thermal conductivity of warm dense carbon by proton differential heating. *Physical Review E*, 100(4):043204, 2019.

[61] James E Bailey, Taisuke Nagayama, Guillaume Pascal Loisel, Gregory Alan Rochau, C Blancard, James Colgan, Ph Cosse, G Faussurier, CJ Fontes,

F Gilleron, et al. A higher-than-predicted measurement of iron opacity at solar interior temperatures. *Nature*, 517(7532):56–59, 2015.

[62] TR Preston, SM Vinko, O Ciricosta, P Hollebon, H-K Chung, GL Dakovski, J Krzywinski, M Minitti, T Burian, J Chalupskỳ, et al. Measurements of the k-shell opacity of a solid-density magnesium plasma heated by an x-ray free-electron laser. *Physical review letters*, 119(8):085001, 2017.

[63] P Hollebon, O Ciricosta, MP Desjarlais, C Cacho, C Spindloe, E Springate, ICE Turcu, JS Wark, and SM Vinko. Ab initio simulations and measurements of the free-free opacity in aluminum. *Physical Review E*, 100(4):043207, 2019.

[64] P Loubeyre, R LeToullec, D Hausermann, M Hanfland, RJ Hemley, HK Mao, and LW Finger. X-ray diffraction and equation of state of hydrogen at megabar pressures. *Nature*, 383(6602):702–704, 1996.

[65] J Clérouin, P Noiret, P Blottiau, V Recoules, B Siberchicot, P Renaudin, C Blancard, G Faussurier, B Holst, and CE Starrett. A database for equations of state and resistivities measurements in the warm dense matter regime. *Physics of Plasmas*, 19(8):082702, 2012.

[66] Siegfried H Glenzer and Ronald Redmer. X-ray thomson scattering in high energy density plasmas. *Reviews of Modern Physics*, 81(4):1625, 2009.

[67] Andrea L Kritcher, Paul Neumayer, John Castor, Tilo Döppner, Roger W Falcone, Otto L Landen, Hae Ja Lee, Richard W Lee, Edward C Morse,

Andrew Ng, et al. Ultrafast x-ray thomson scattering of shock-compressed matter. *Science*, 322(5898):69–71, 2008.

[68] AJ Visco, RP Drake, SH Glenzer, T Döppner, G Gregori, DH Froula, and MJ Grosskopf. Measurement of radiative shock properties by x-ray thomson scattering. *Physical review letters*, 108(14):145001, 2012.

[69] LB Fletcher, AL Kritcher, A Pak, T Ma, T Döppner, C Fortmann, L Divol, OS Jones, OL Landen, HA Scott, et al. Observations of continuum depression in warm dense matter with x-ray thomson scattering. *Physical review letters*, 112(14):145004, 2014.

[70] Paul Mabey, S Richardson, TG White, LB Fletcher, SH Glenzer, NJ Hartley, J Vorberger, DO Gericke, and Gianluca Gregori. A strong diffusive ion mode in dense ionized matter predicted by langevin dynamics. *Nature communications*, 8(1):1–6, 2017.

[71] Brett Larder, DO Gericke, Scott Richardson, Paul Mabey, TG White, and Gianluca Gregori. Fast nonadiabatic dynamics of many-body quantum systems. *Science Advances*, 5(11):eaaw1634, 2019.

[72] DJ Hoarty, P Allan, SF James, CRD Brown, LMR Hobbs, MP Hill, JWO Harris, J Morton, MG Brookes, R Shepherd, et al. Observations of the effect of ionization-potential depression in hot dense plasma. *Physical review letters*, 110(26):265003, 2013.

[73] Sam M Vinko. X-ray free-electron laser studies of dense plasmas. *Journal of Plasma Physics*, 81(5), 2015.

[74] V Recoules and S Mazevet. Temperature and density dependence of xanes spectra in warm dense aluminum plasmas. *Physical Review B*, 80(6):064110, 2009.

[75] Yuan Ping and Federica Coppari. Laser shock xafs studies at omega facility. *High Pressure Research*, 36(3):303–314, 2016.

[76] Cullie J Sparks Jr. Inelastic resonance emission of x rays: anomalous scattering associated with anomalous dispersion. *Physical Review Letters*, 33(5):262, 1974.

[77] P Eisenberger, PM Platzman, and H Winick. X-ray resonant raman scattering: observation of characteristic radiation narrower than the lifetime width. *Physical Review Letters*, 36(11):623, 1976.

[78] P Eisenberger, PM Platzman, and H Winick. Resonant x-ray raman scattering studies using synchrotron radiation. *Physical Review B*, 13(6):2377, 1976.

[79] Eberhard Burkel. Phonon spectroscopy by inelastic x-ray scattering. *Reports on Progress in Physics*, 63(2):171, 2000.

[80] Luuk JP Ament, Michel Van Veenendaal, Thomas P Devereaux, John P Hill, and Jeroen Van Den Brink. Resonant inelastic x-ray scattering studies of elementary excitations. *Reviews of Modern Physics*, 83(2):705, 2011.

[81] PM Platzman and ED Isaacs. Resonant inelastic x-ray scattering. *Physical Review B*, 57(18):11107, 1998.

[82] S Reiche, P Musumeci, C Pellegrini, and JB Rosenzweig. Development of ultra-short pulse, single coherent spike for sase x-ray fels. *Nuclear Instruments and Methods in Physics Research Section A: Accelerators, Spectrometers, Detectors and Associated Equipment*, 593(1-2):45–48, 2008.

[83] Bob Nagler, Brice Arnold, Gary Bouchard, Richard F Boyce, Richard M Boyce, Alice Callen, Marc Campell, Ruben Curiel, Eric Galtier, Justin Garofoli, et al. The matter in extreme conditions instrument at the linac coherent light source. *Journal of synchrotron radiation*, 22(3):520–525, 2015.

[84] H Sorum and J Bremer. High-resolution studies of the k emission spectra of nickel. *Journal of Physics F: Metal Physics*, 12(11):2721, 1982.

[85] Xavier Gonze, J-M Beuken, R Caracas, F Detraux, M Fuchs, G-M Rignanese, Luc Sindic, Matthieu Verstraete, G Zerah, F Jollet, et al. First-principles computation of material properties: the abinit software project. *Computational Materials Science*, 25(3):478–492, 2002.

[86] Marc Torrent, François Jollet, François Bottin, Gilles Zérah, and Xavier Gonze. Implementation of the projector augmented-wave method in the abinit code: Application to the study of iron under pressure. *Computational Materials Science*, 42(2):337–351, 2008.

[87] Burton L Henke, Eric M Gullikson, and John C Davis. X-ray interactions: photoabsorption, scattering, transmission, and reflection at e= 50-30,000 ev, z= 1-92. *Atomic data and nuclear data tables*, 54(2):181–342, 1993.

[88] MF Kasim, TP Galligan, J Topp-Mugglestone, G Gregori, and SM Vinko. Inverse problem instabilities in large-scale modeling of matter in extreme conditions. *Physics of Plasmas*, 26(11):112706, 2019.

[89] Hisao Nagasawa, Spiridon Mourikis, and Winfried Schülke. X-ray raman spectrum of li, be and graphite in a high-resolution inelastic synchrotron x-ray scattering experiment. *Journal of the Physical Society of Japan*, 58(2):710–717, 1989.

[90] Winfried Schülke. *Electron dynamics by inelastic X-ray scattering*. Number 7 in Oxford series on synchrotron radiation. Oxford University Press, 2007.

[91] Abhay Shukla, Jean-Pascal Rueff, James Badro, Gyorgy Vanko, Aleksi Mattila, FM F de Groot, and Francesco Sette. Charge transfer at very high pressure in nio. *Physical Review B*, 67(8):081101, 2003.

[92] BJB Crowley. Continuum lowering–a new perspective. *High Energy Density Physics*, 13:84–102, 2014.

[93] G Kulcsar, D AlMawlawi, Fw Budnik, Pr Herman, M Moskovits, L Zhao, and Rs Marjoribanks. Intense picosecond X-Ray pulses from laser plasmas by use of nanostructured "Velvet" targets. *Physical review letters*, 84(22):5149–52, 2000.

[94] Michael A Purvis, Vyacheslav N Shlyaptsev, Reed Hollinger, Clayton Bargsten, Alexander Pukhov, Amy Prieto, Yong Wang, Bradley M Luther, Liang Yin, Shoujun Wang, et al. Relativistic plasma nanophotonics for ultrahigh energy density physics. *Nature Photonics*, 7(10):796, 2013.

[95] Clayton Bargsten, Reed Hollinger, Maria Gabriela Capeluto, Vural Kaymak, Alexander Pukhov, Shoujun Wang, Alex Rockwood, Yong Wang, David Keiss, Riccardo Tommasini, Richard London, Jaebum Park, Michel Busquet, Marcel Klapisch, Vyacheslav N. Shlyaptsev, and Jorge J. Rocca. Energy penetration into arrays of aligned nanowires irradiated with relativistic intensities: Scaling to terabar pressures. *Science Advances*, 3(1):3–11, 2017.

[96] O S Humphries, P Allan, C R D Brown, L M R Hobbs, S F James, M G Ramsay, B Williams, D J Hoarty, and S M Vinko. Time evolution of transient plasma states from nanowire arrays irradiated at relativistic intensities. *Manuscript submitted for publication*, 2020.

[97] Jukka Venermo and Ari Sihvola. Dielectric polarizability of circular cylinder. *Journal of electrostatics*, 63(2):101–117, 2005.

[98] Gábor Kulcsár. *Intense picosecond x rays from structured targets*. PhD thesis, National Library of Canada= Bibliothèque nationale du Canada, 2000.

[99] PB Johnson and RW Christy. Optical constants of transition metals: Ti, v, cr, mn, fe, co, ni, and pd. *Physical review B*, 9(12):5056, 1974.

[100] David Hillier, Colin Danson, David Egan, Stephen Elsmere, Mark Girling, Ewan Harvey, Nicholas Hopps, Michael Norman, Stefan Parker, Paul Treadwell, et al. Contrast enhancements to petawatt lasers using picosecond optical parametric amplification and frequency doubling. In *2014 Conference on Lasers and Electro-Optics (CLEO)-Laser Science to Photonic Applications*, pages 1–2. IEEE, 2014.

[101] H-K Chung, MH Chen, WL Morgan, Yu Ralchenko, and RW Lee. Flychk: Generalized population kinetics and spectral model for rapid spectroscopic analysis for all elements. *High energy density physics*, 1(1):3–12, 2005.

[102] Daniel Nilsson, Fredrik Uhlén, Anders Holmberg, Hans M Hertz, Andreas Schropp, Jens Patommel, Robert Hoppe, Frank Seiboth, Vivienne Meier, Christian G Schroer, et al. Ronchi test for characterization of nanofocusing optics at a hard x-ray free-electron laser. *Optics letters*, 37(24):5046–5048, 2012.